NANO-/MICRO-STRUCTURED MEMBRANE ENABLED WATER AND ENERGY SUSTAINABILITY

A Dissertation

by

YUCHEN LIU

Submitted to the Office of Graduate and Professional Studies of
Texas A&M University
in partial fulfillment of the requirements for the degree of

DOCTOR OF PHILOSOPHY

Chair of Committee,	Shiren Wang
Committee Members,	Xingmao Ma
	Hamid Parsaei
	Li Zeng
Head of Department,	Lewis Ntaimo

May 2021

Major Subject: Industrial and Systems Engineering

ABSTRACT

Environmental sustainability covers a wide range of issues starting from a specific location to a global one. Energy and water issues are two essential elements of a sustainable society. The research objectives in this dissertation are to reduce the energy consumption during water desalination to broader the application of such water treatment techniques and also reduce the energy consumption for the cooling and heating system. The energy-efficient water desalination can be achieved by tuning the interlayer spacing of graphene oxide (GO) laminates and shortening the water pathway through the filtration membrane. Compared to the previous research, as-designed reverse osmosis (RO) membranes can provide a stable high ion-rejection rate ascribed to the fixed interlayer spacing and a high ion-permeation rate because of a short water-flowing pathway. In addition, the energy-saving cooling and heating system was achieved by the environmentally-adaptive membrane (EAM), consisting of delicately microstructures made from the thermal-sensitive polymer. In this dissertation, my research focuses on three topics:

- Fullerene tailored graphene oxide interlayer spacing for water sustainability
- Scalable gradient graphene oxide nanostructure for water sustainability
- Environmentally-adaptive self-cooling and heating membrane for energy sustainability

All three topics developed in the dissertation are to realize the energy efficiency for social sustainability through nano-/micro-structured membrane enabled technologies.

DEDICATION

I dedicate my dissertation work to my family and many friends. I am very grateful to my loving parents, whose words of encouragement and push for tenacity ring in my ears. My cousins, aunts, and uncles have never left my side and are very special to me. My grandparents always live in my heart, and I miss you so much. My mother-in-law gives me a lot of help. I also dedicate this dissertation to my many friends who have supported me throughout the process. I will always appreciate all they have done. I dedicate this work and give special thanks to my wife Bing and my lovely daughter Cyanne for being there for me throughout the doctorate program. Both of you have been my best cheerleaders.

ACKNOWLEDGMENTS

I wish to thank my committee members, who were more than generous with their expertise and precious time. A special thanks to Dr. Shiren Wang, my committee chairman, for his countless hours of reflecting, reading, guidance, and most of all, patience throughout the entire doctorate program at Texas A&M University. His mentorship was paramount in providing a well-rounded experience consistent with my long-term career goal.

I would also like to thank Dr. Jingjing Qiu, Dr. Lei Fang, and Dr. Ming-Wei Lin for guiding my research in the past several years and developing my background in material science and chemistry. Thank you, Dr. Xingmao Ma, Dr. Hamid Parsaei, and Dr. Li Zeng, for agreeing to serve on my committee. Thanks also go to all present and graduated members from Dr. Wang's group (Dr. Kun Zhang, Dr. Liming Wang, Dr. Biran Wang, Zimeng Zhang, Wei Li, Ruochen Liu, Jun Ma, and Chongjie Gao). It has been an unforgettable experience to work and study with you all. Thanks go to my friend Minjie Lu, who gave me the courage to come to Texas A&M University.

I want to acknowledge and thank my school division for allowing me to conduct my research and providing any assistance requested. Special thanks go to the staff member, Shannon Caldwell from the Department of Industrial and Systems Engineering, for his continued support.

Finally, but most importantly, I would like to thank my wife and daughter for their unwavering love, support, and encouragement through my good and bad times.

CONTRIBUTORS AND FUNDING SOURCES

Contributors

This work was supervised by a dissertation committee consisting of Professor Shiren Wang (Chair of Committee), Professor Hamid Parsaei, Professor Li Zeng of the Department of Industrial and Systems Engineering, and Professor Xingmao Ma of the Department of Civil and Environmental Engineering.

The SEM characterization for Chapter 3 and 4 were performed with the help of Zimeng Zhang. The DMA tests in Chapter 4 were performed with the help of Ruochen Liu. The data analysis in Chapter V were performed with the help of Dr. Minjie Lu.

All other work conducted for the thesis (or) dissertation was completed by the student independently.

Funding Sources

The research work was supported by the Water Research Grant from The State of Texas, and also partially supported by the National Science Foundation (CMMI #1634858 and CMMI#1934120), and President's Excellence Fund.

TABLE OF CONTENTS

Page

ABSTRACT II

DEDICATION III

ACKNOWLEDGMENTS IV

CONTRIBUTORS AND FUNDING SOURCES V

TABLE OF CONTENTS VI

LIST OF FIGURES VIII

LIST OF TABLES XIII

CHAPTER I INTRODUCTION 1

1.1 Motivation 1
1.2 Technical challenges 6
1.3 Research objectives 7

CHAPTER II LITERATURE REVIEW 9

2.1 Graphene-based RO membranes 9
2.2 Environmentally-adaptive technologies for passive radiative cooling and heating 14

CHAPTER III FULLERENE TAILORED GRAPHENE OXIDE INTERLAYER SPACING FOR WATER SUSTAINABILITY 17

3.1 Introduction 17
3.2 Experiments 20
3.2.1 Preparation of C60-grafted GO 20
3.2.2 Preparation of GO/C60 membrane 21
3.2.3 Characterization 22
3.3 Results and Discussion 23
3.3.1 Water desalination mechanism for C60-grafted GO membrane 23
3.3.2 Grafting C60 to GO and membrane fabrication 25
3.3.3 Membrane characterization and desalination test 29

3.4 Summary 39

CHAPTER IV SCALABLE GRADIENT GRAPHENE OXIDE NANOSTRUCTURE FOR WATER SUSTAINABILITY 40

4.1 Introduction 40
4.2 Experiments 42
4.2.1 Numerical simulation 42
4.2.2 Preparation of gradient nanocomposite membrane 43
4.2.3 Characterization 44
4.2.4 Desalination Test 45
4.2.5 Scale-Up Demonstration 47
4.2.6 Energy Consumption Calculation 47
4.3 Results and Discussion 50
4.3.1 Gradient structure design 51
4.3.2 Gradient GO membrane fabrication 58
4.3.3 Desalination test and scalability 63
4.4 Summary 71

CHAPTER V ENVIRONMENTALLY-ADAPTIVE MEMBRANE FOR RADIATIVE COOLING AND HEATING 73

5.1 Introduction 73
5.2 Experiments 77
5.2.1 Materials 77
5.2.2 NIPAM resist synthesis 77
5.2.3 Pretreatment of substrates 78
5.2.4 Fabrication of 3D microstructures 78
5.2.5 Characterization 79
5.2.6 Radiative cooling power calculation 79
5.2.7 Numerical simulation 81
5.3 Results and Discussion 81
5.3.1 Structure design and numerical simulation 81
5.3.2 Two-photon laser lithography of PNIPAM microstructures 86
5.4 Conclusion 100

CHAPTER VI CONCLUSIONS AND FUTURE WORK 101

6.1 Conclusions 101
6.2 Future Work 103

REFERENCES 105

LIST OF FIGURES

Page

Figure 1.1. 1 (a) Membrane processes for water purification and the corresponding size of waste materials in seawater and brackish water. (b) Energy consumption for industrial RO desalination plants and other treatments of water. 4

Figure 3.1. 1 Schematic representation of graphene oxide (GO) and fullerene (C60) hybrid for desalination process of (a) cross-sectional membrane and (b) flat membrane desalination. C60 was grafted between the laminates of GO. When the pressure is applied from the top side of the membrane, water passes through the membrane driven by the applied force while the membrane blocks the anion and cation. 20

Figure 3.3. 1 Schematic diagram of the ions with large hydration diameter during passing through the membrane tunnel. 24

Figure 3.3. 2 Schematic illustration of the separation process of GO/C60 membrane at the entrance: (a) electrostatic exclusion for anions (Cl^-)[108, 109]; (b) steric effects for cations (Na^+)[110, 111]. 25

Figure 3.3. 3 Schematic of beam bending theory. 26

Figure 3.3. 4 AFM image of the single layer GO.....27

Figure 3.3. 5 (a) TEM image of pure GO layer (The skinny layer with a little bit folding edge represents GO layer. The scale bar is 100 nm.) (b) Schematic illustration of grafting C60 onto GO layer through lithiation reaction. (c) TEM image of C60-grafted GO layer. (The smooth layer with irregular shape represents the GO layer, and the dark dots represent C60 nanoparticles. The scale bar for this image is 20 nm. The size of this GO layer is around 150 nm while C60 nanoparticles are 1-2 nm.) 28

Figure 3.3. 6 SEM image of GO laminates. Scale bar 1 μm. 29

Figure 3.3. 7 XRD characterization: XRD pattern of as-prepared GO/C60 membrane and pure GO membrane, where the red, blue, and green lines indicate the feed ratio of GO: C60 = 1:2, 1:1, and 2:1 respectively, and the orange line represents the pure GO; The peak of C60-grafted GO is around 7° which means 12.5 Å in interlayer spacing. On the other hand, the pristine GO peaks at 11.5°, indicating 7.7 Å in interlayer spacing. 31

Figure 3.3. 8 GO/C60 membranes fabrication process and water desalination setup. (a) Photograph of pure GO membrane. (b) Photograph of C60-grafted GO

membrane (c) Optical micrograph of the cross-sectional area, which shows 148-μm-thick GO laminates (red arrow) embedded in 81-μm thick epoxy (black arrow). Epoxy and GO/C60 layers are labeled in the figure. The scale bar is 100 μm. (d) Photograph of GO/C60 membrane encapsulated with epoxy and glued into a rectangular slot within a plastic disk of 47 mm in diameter. (e) Photograph of GO/C60 membrane inside the water desalination setup. (f) Schematic of water desalination setup. 32

Figure 3.3. 9 (a) Ion permeation rate and (b) Ion rejection rate through GO/C60 membrane with different pressure applied. The red, blue, and green lines indicate the feed ratio of GO: C60 = 1:2, 1:1, and 2:1, respectively. The dashed line indicates the feed ratio of GO: C60=1:1, which uses the flat surface for desalination. 34

Figure 3.3. 10 Water permeation rate through GO/C60 membrane with different pressure applied. The red, blue, and green lines indicate the feed ratio of GO: C60 = 1:2, 1:1, and 2:1, respectively. The dashed line indicates the feed ratio of GO: C60=1:1, which uses the flat surface for desalination. 35

Figure 3.3. 11 Ion concentration on the permeation side through GO/C60 membrane over the period. The red, blue, and green lines indicate the feed ratio of GO: C60 = 1:2, 1:1, and 2:1, respectively. 36

Figure 4.2. 1 Setup for (a) water desalination test and (b) large scale membrane fabrication. 46

Figure 4.3. 1 Schematic of gradient structure consisting of GO laminates with 1nm channels and two symmetric mesoporous (2-50 nm pore size) layers. The ion is sieved via the middle layer, 1nm-channels GO laminates. 51

Figure 4.3. 2 Tensile strength and Young's Modulus. (a) Photograph of GO laminates after tensile test. (b) Stress-strain curve of GO laminates with different lateral sizes of GO nanosheets (1430 nm, 1009 nm, 473 nm, and 276 nm, respectively). (c) calculated tensile strength and Young's Modulus based on the stress-strain curve with different lateral sizes of GO nanosheets (1430 nm, 1009 nm, 473 nm, and 276 nm, respectively). 53

Figure 4.3. 3 Numerical illustrating the design of gradient structure. (a) The maximum tensile stress acting on the GO laminates and corresponding water flux with the different thickness of the protective layer (0, 10 nm, 100 nm, 1 μm, 10 μm, and 100 μm). (b) The maximum tensile stress acting on the GO laminates and corresponding water flux with different aperture sizes of the protective layer ranged from 10 nm to 200 nm. The dashed line indicates the tensile stress tolerance of the GO laminates, which determines the aperture size selection of the protective layer. 55

Figure 4.3. 4 Numerical simulation effects of the protective layer with different thickness and aperture sizes. (a) The cross-sectional tensile stress distribution on the GO laminates with the different thicknesses of the protective layer (h=0, 10 nm, 100 nm, and 1000 nm, respectively). (b) The tensile stress acting on the GO laminates with different aperture sizes of the protective layer (25 nm, 50 nm, 100 nm, and 200 nm, respectively). 58

Figure 4.3. 5 Schematic of gradient GO-PPD membrane fabrication procedure and corresponding experimental characterizations. (a) The fabrication procedure of the gradient membrane. (b) DLS patterns and AFM images of GO nanosheets with different tip sonication periods (0 min, 3 min, 10 min, and 20 min which exhibit GO lateral size with 1430 nm, 1009 nm, 473 nm, and 276 nm, respectively). The width of each AFM image is 2 μm. (c) SEM image of gradient structure on cross-sectional view. The GO laminates were clamped by two MCE membranes. The scale bar for the large image and the insert magnification image are 100 μm and 100 nm, respectively. 59

Figure 4.3. 6 XRD pattern of as-prepared pure GO (orange), uncrosslinked GO-PPD (red), and crosslinked GO-PPD (purple) membranes. 61

Figure 4.3. 7 ATR-FTIR spectra of pure GO (orange), uncrosslinked GO-PPD (red), and crosslinked GO-PPD (purple) membranes. 62

Figure 4.3. 8 GO laminates surface morphology test by AFM. The lateral size of each image is 2 μm. 63

Figure 4.3. 9 Desalination performance of gradient GO membrane. (a) The water permeance for different thicknesses of GO membrane and different lateral sizes of GO sheets. The inserted image shows the water-transport pathway through the GO laminates. (b) The ion rejection rate for different thickness of GO membrane and different lateral size of GO sheets. The inserted image shows the test setup. (c) The water flux for different applied pressure. The dashed line indicates the linear trend line without the concentration polarization issue. (d) The ion concentration on the permeation side through gradient membrane for different periods (the red and blue lines indicate the uncrosslinked GO laminates and crosslinked GO laminates, respectively). 66

Figure 4.3. 10 (a) Filtration energy consumption and overall energy consumption of RO desalination for brackish water and seawater. (b) Comparison of the energy consumption between this work and the state-of-the-art RO desalination membranes including commercial membranes[144] and PA/DA/TMC[162] for 35,000 ppm seawater and commercial membranes[163], CNT-TA membranes[117], NaY Zeolite membranes[164], MWNT/TNT membranes[142], KCl-controlled GO membranes[36], CNT/PMMA membranes[116], GO/PA membranes[165], and technical data

from El Paso Water Utilities for 2,000 ppm brackish water. (c) The forecast of future brackish water supply and corresponding cumulative cost saving by applying the gradient GO membranes. 69

Figure 4.3. 11 Scale-up demonstrations of gradient nanocomposite membrane. (a) As-prepared scale-up gradient nanocomposite membrane. (b) The ion concentration on the permeation side through gradient membrane and ion rejection rate at different periods for scale-up gradient GO membranes (the red and blue lines indicate the permeate ion concentration and the ion rejection rate, respectively). 71

Figure 5.3. 1 Schematic of responsive structure for environmentally-adaptive cooling and warming. (a) Environmental temperature-induced structure evolution for radiative cooling and heating. (b) The mechanism of environmentally-adaptive self-cooling and heating membrane through IR radiation transmission and reflection. 83

Figure 5.3. 2 Simulation of emissivity of different sizes of EAM structures. (a) Side-view of the designed system. (b) The developed model in Lumerical FDTD simulation. (c) Calculated emissivity spectra for different bottom lengths of the closed-flower structure.....86

Figure 5.3. 3 Environmentally-adaptive micro-structure fabrication. (a) Temperature-induced transformation between open-flower structure and closed-flower structure. (b-c) Top view and 3D image of printed open-flower structure. (d-e) Top view and 3D image of printed closed-flower structure. 89

Figure 5.3. 4 Printed sample for closed-flower structure and open-flower structure with the different bottom lengths of the pyramid structure (a = 30 μm, 60 μm, 90 μm, and 120 μm, respectively). 94

Figure 5.3. 5 Optical properties of the EAM. (a) Measured emissivity (absorptivity) of the EAM for different bottom lengths of the pyramid structure. The wavelength ranged from 0.4 μm to 3 μm was measured by UV-Vis-NIR and the wavelength ranged from 4 μm to 16 μm was measured by FTIR. (b) Calculated cooling power without the presence of nonradiative heat exchange for different bottom lengths of the pyramid structure. (c) Net cooling (heating) power of the designed EAM for different bottom lengths of the pyramid structure. 96

Figure 5.3. 6 Thermal measurement of the EAM. (a) The cooling and warming test system. (b, c) The temperature distribution of the experimental group and the control group respectively. (d) Cooling effect of the experiment group (EAM on the substrate) and the control group (substrate only), respectively. (e)

Heating effect of the experiment group (EAM on the substrate) and the control group (substrate only), respectively. 99

LIST OF TABLES

Page

Table 3. 1 Comparative Results of Different Nanofiltration Membranes 37

Table 5. 1 Geometric parameters of the printed structure 91

CHAPTER I

INTRODUCTION

1.1 Motivation

Water and energy are fundamental resources used for economic, social, and cultural development. With the increase of population and evolvements brought by the industrial revolution, it is undeniable that water and energy demands have increased, and the resources are too scarce to realize global sustainability. Increasing renewable energy sources and decreasing energy consumption are essential strategies for achieving sustainability. Technological innovations can help energy-saving performance and support sustainable development pathways.

Sustainability has various meanings in the context of water acquisition and reuse. Water resources are irreplaceable and fundamental elements whose usage is increasing worldwide by 1% per year since the 1980s[1][*]. But at present, human beings are suffering from the severe freshwater crisis, which is compromising food security and public health[2]. The rising demands of freshwater make the situation even worse due to the rapid population growth of the global population, urbanization, rapid industrialization, global climate change, and more stringent health-based water quality standards[3]. Global water

[*] Reprinted with permission from "Carbon Nanopore-Tailored Reverse Osmotic Water Desalination " by Yuchen Liu, et. al, 2020. ACS ES&T Water, 1, 1, 34-47, Copyright 2020 by American Chemical Society.

demand is expected to increase by 20% to 30% above the current water use level until 2050. Although 71% of the earth's surface is water-covered, more than 96% of this water is held by the oceans as saline water. The remaining freshwater also includes glaciers, ice caps, groundwater, and surface water, which means only less than 1% water resource on the earth is readily usable for domestic activities and agriculture[4]. Unfortunately, the distribution of freshwater resources on the planet is incredibly uneven. According to the satellite-based study, the earth's dry areas are getting drier while the wet areas are increasingly wetter, which intensifies the current severe situation[5].

Generally, water can be classified into the following levels based on the dissolved-solids concentration in milligrams per liter (ppm) as seawater (> 10,000 ppm), brackish water (1,000 - 10,000 ppm), and freshwater (< 1,000 ppm). Freshwater is the standard water resource for daily life and social development. As the freshwater demand crisis increased, unconventional water sources such as stormwater, brackish water, industrial wastewater, and seawater are considered to be used, especially in some water-stressed areas. Seawater is the most inexhaustible water source on the earth, while the high salinity constrains the application on domestic activities. Brackish water possesses an extensive amount all over the world. It comes from brackish fossil aquifers, human activity byproducts, and the salinity gradient power process's waste product. Texas, for example, has abundant underground water, including 880 trillion gallons of primarily brackish groundwater. In this case, the desalination process is one of the best strategies to acquire freshwater from salinity to achieve water sustainability. Desalination is defined as removing the salts and other dissolved-solids from either seawater or brackish water to

obtain fresh water suitable for human consumption and industrial and domestic requirements[6]. Desalination methods can be classified as distillation (including multi-stage flash distillation and multiple-effect distillation), ion exchange, membrane processes, freezing desalination, geothermal desalination, eletrodeionisation (EDI), and solar desalination[7]. The membrane processes which are driven by hydraulic pressure can be distinguished as reverse osmosis/forward osmosis (RO/FO), nanofiltration (NF), ultrafiltration (UF), and microfiltration (MF) based on the feature size (as shown in Fig. 1.1.1 (a)). The primary function of MF and UF membranes is to retain suspended particles and macromolecules. The mass transport in MF and UF membranes is governed by a size or sieving exclusion mechanism. On the other hand, NF and RO focus on removing nearly all kinds of ions to reduce water salinity. The molecular separation of RO is based on the solution-diffusion mechanism. The separation mechanism of NF is a combination of sieving exclusion and solution-diffusion.

Specifically, over 65% of the installed desalination capacity is based on the RO desalination process[8]. RO desalination is a water purification technology that uses applied pressure overcoming the osmotic pressure to separate the water molecule from the salinity with the help of a partially permeable membrane. Compared with thermal distillation and other desalination methods, RO technology has significant advantages in the continuous process, mild working conditions, energy efficiency, low environmental pollution, and ease of operation[9]. However, the conflict between desalination efficiency and the vast energy consumption is still the biggest obstacle in developing desalination technologies. Fig. 1.1.1 (b)) compares the productivity and electricity consumption in

various desalination companies worldwide and the energy consumption of different water treatment methods. As shown in the figure, seawater purification's energy consumption is ten times larger than surface water treatment. Specifically, the intensive energy consumption of the RO unit represents 50%-60% of the total cost of the whole desalination process[10]. Herein, reducing the energy consumption during the membrane filtration process of water desalination is a promising strategy to broader the applications of RO desalination technology.

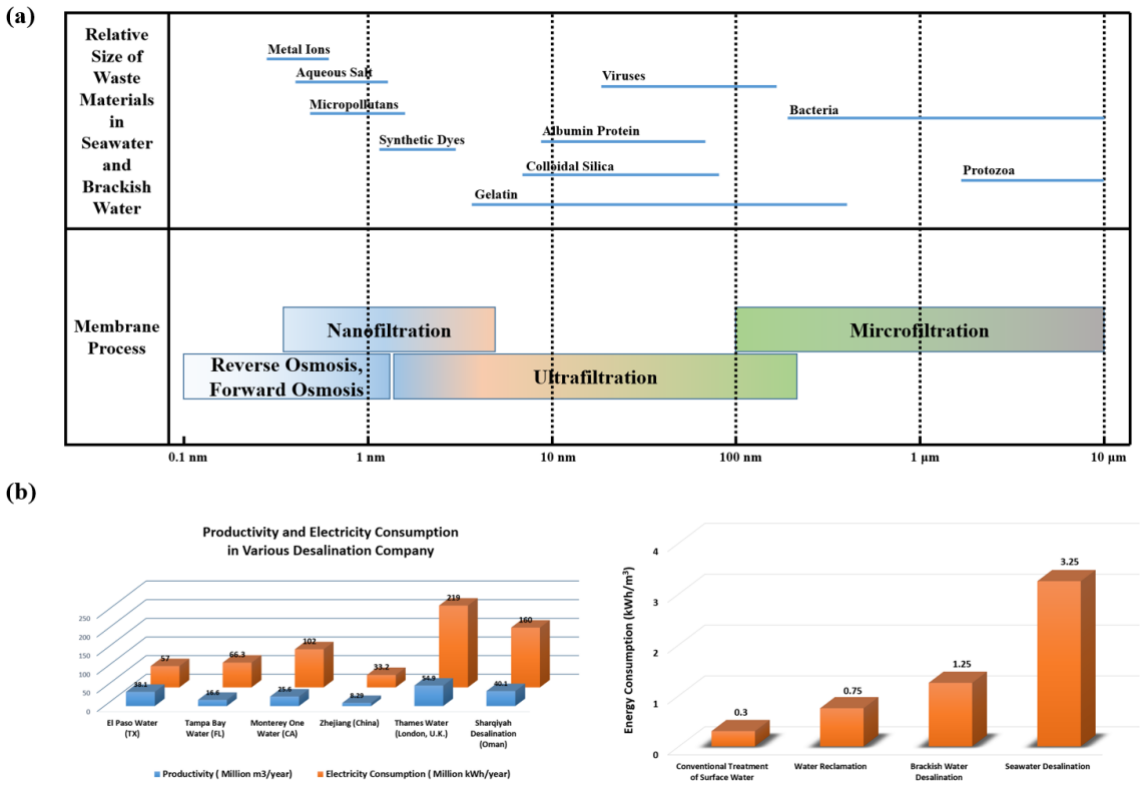

Figure 1.1. 1 (a) Membrane processes for water purification and the corresponding size of waste materials in seawater and brackish water. (b) Energy consumption for industrial RO desalination plants and other treatments of water.

On the other hand, the current global energy issue comes from limited fossil energy supplies and the environmental impacts for its entire energy life cycle, from mining and processing to emissions, waste disposal, and recycling. In 2019, the electricity used by the residential end sector was about 1,400 billion kW in the United States, which attributes 50% of the total usage. Space heating and cooling account for 26% of that and approximately cost 44 billion USD per year[11]. Considering the rapid population growth and the climate change due to the global greenhouse gas emission, the space heating and cooling energy consumption for buildings will grow by 79% and 83% throughout 2010-2050, respectively[12]. Conventional air-conditioning, heating, and ventilation (HVAC) systems heavily rely on vapor compression-based cooling technologies, which consume massive fossil energy and emit vast amounts of greenhouse gases. Therefore, other economic and environmental-friendly cooling and heating systems will arise great attention. Radiative cooling and heating technology provides an alternative passive cooling and heating solution using the atmospheric window[13]. Since radiative heating is originally a passive process, recent research mainly focuses on passive radiative cooling. Radiative cooling can be achieved by carefully selecting and designing the materials and structures with high emissivity in the spectral wavelength of 8 -13 μm. However, due to the climate and temperature changes day and night, summer and winter, the monofunctional emitters cannot dynamically control the optical channel for thermal management. An energy-saving membrane with a superior cooling and heating effect and satisfactory wearability properties provides a novel way of saving the energy used by indoor cooling and heating systems and human body-temperature management. As a

passive, effective, and renewable form of decreasing cooling energy requirements without power input, radiative cooling has attracted considerable attention in the field of energy-saving applications[14]. However, automatically switching the cooling and heating performance through one single membrane based on the environmental stimulus is still very challenging.

1.2 Technical challenges

Current RO membranes used in desalination are still limited by intensive energy consumption and low energy-efficiency. Emerging selectively permeable membranes with sub-nanometer channels attract considerable attention for energy-efficient desalination[15-17]. Particularly, graphene has emerged as an attractive material for water desalination because of its outstanding antifouling and barrier performance. Single-layer graphene oxide (GO) with ~1nm pores have been studied for RO desalination[18, 19]. However, it is incredibly challenging to perforate 1nm nanopores in a single-layer defect-free graphene nanosheet in a scalable way, although numerous methods readily percolate large pores. Vertically aligned GO-based membranes have also been attempted for RO desalination, but it was also challenging to scale up[20]. Laminated GO nanosheets are scalable but demonstrated intensive energy consumption due to the sizeable hydrodynamic resistance[21, 22]. Hence, energy consumption and scalability are the key challenges of membrane technologies applying to water desalination.

On the other hand, due to the high energy consumption of traditional HVAC systems, passive radiative cooling and heating systems are essential to solving this obstacle. Although plenty of efforts have been made on radiative cooling, most of these approaches are monofunctional, which can only address radiative cooling or heating and cannot adapt the function according to the ambient temperature. The emissivity of the emitter is not tunable according to the ambient temperature. Herein, significant effort is needed to investigate the process of chemistry and physics for producing the thermal responsive structure for environmentally-adaptive membrane.

1.3 Research objectives

Three research objectives will be proposed and studied in this dissertation to achieve nanostructured membrane-enabled water and energy sustainability.

In the first topic, tuning interlayer spacing of graphene oxide (GO) to achieve high water flux during the desalination process is proposed. The proposed method incorporates covalent bonds between C60 and GO to fix the interlayer spacing of GO laminates at a proper range to achieve low energy consumption and high ion rejection rate. Chemical synthesis, membrane characterization, desalination test, and membrane lifetime were investigated. An energy-consuming analysis is also proposed. Chapter 3 will elaborate on this topic.

Secondly, a scalable gradient structure of GO-based membrane will be studied and discussed in Chapter 4. Since the water permeance is negatively related to the water-

transport pathway length and the ion rejection rate depends on interlayer spacing stability, reducing the thickness of the filtration membrane with fixed interlayer spacing can effectively saving energy consumption. In this case, a scalable gradient structure consisting of porous cellulose nanostructure and cross-linked graphene oxide (GO) nanosheets were designed and fabricated to achieve an energy-saving ion separation process. Chapter 4 will investigate energy-consuming analysis, membrane characterization, desalination test, and membrane lifetime.

Third, environmentally-adaptive self-cooling and heating using membrane technology are proposed in Chapter 5. The theoretical simulation was studied by the FDTD method. The environmentally-adaptive membrane for both radiative cooling and heating based on PNIPAM will be demonstrated. The emissivity of the membrane will be tested, and the corresponding cooling and heating power will be calculated. Furthermore, the cooling and heating performance of the membrane will be investigated by the IR camera.

CHAPTER II

LITERATURE REVIEW

In this chapter, the current state-of-the-art research progresses of graphene-based RO membranes and radiative cooling and heating membranes will be reviewed, which lead to the generation of the three research topics in the dissertation.

2.1 Graphene-based RO membranes*

The general idea for water desalination is transporting a water molecular from one side of a membrane to the other while rejecting the salinity. Herein, the simplest method is fabricating lateral pores on the surface of 2D-materials. A single-atomic thick graphene layer with a precisely controlled pore size is an ideal separation membrane. Researchers grew single-layer graphene via chemical vapor deposition (CVD) on a copper foil with the boundary of size at 50 μm[23]. The single-layer non-defect graphene was then transferred to a silicon nitride substrate with a 2 μm-hole for desalination test. In order to generate sub-nanometer pores on graphene, oxygen plasma etching is applied on the single-layer graphene to remove carbon atoms from the 2D lattice. By precisely controlling exposure time and power, the pore size of the NPG is confined in the range of

---

* Reprinted with permission from "Carbon Nanopore-Tailored Reverse Osmotic Water Desalination " by Yuchen Liu, et. al, 2020. ACS ES&T Water, 1, 1, 34-47, Copyright 2020 by American Chemical Society.

0.5-1 nm, which is the anticipated optimal pore size for ion sieving and water permeation, and the pore-density is on the order of 1/100 nm^2. The ion rejection rate of the single-layer NPG is nearly 100%, exceeding most of the reported desalination membrane. The membrane also exhibited outstanding water flux up to 10^6 g/ (m^2·s) at 40 °C driven by pressure difference while the water flux caused by osmotic pressure is less than 70 g/ (m^2·s·atm). Although NPG shows several higher water flux orders than current RO membranes, it is still restricted in the laboratory. Because of the requirements of the high density of porosity and the precise control of pore size for water desalination, the formation of large-scale single-layer defect-free graphene is very challenging[24].

Compared with porous membranes in which water flows directly through the membrane, non-porous membranes require water molecules to walk along the channels perpendicular to the direction of water flow. Because of the atomically smooth surface and thin layer, graphene-based materials become natural candidates for water desalination. To achieve an optimal ion selectivity for different feed water concentrations, non-porous graphene should comprise a multi-layered stack of finite-sized graphene sheets. Generally, graphene-based non-porous membranes were fabricated via vacuum filtration or layer-by-layer (LBL) assembling of graphene oxide (GO), which is commonly oxidized from graphite and exfoliated to single-layer[25-28]. Recalling the advantages of CNT, which possesses an atomically smooth channel for water molecules moving without friction, GO layer with a number of hydrophilic groups also exhibits the same benefits. Compared to previous NPG and hollow nanochannel structures, the lateral one is extensively studied due to its simplicity.

In 2014, a group of researchers from Manchester University first studied the stacked graphene oxide layers for water desalination. In order to increase the selectivity, the interlayer spacing of GO laminates needed to be precisely controlled. They proved that after vacuum filtration, the formed GO laminates exhibited an interlayer spacing of 0.9 ± 0.1 nm in the humid air. In comparison, the interlayer spacing of another group was significantly increased to 1.3 ± 0.1 nm in water, which could not reject the monovalent, divalent cations, and corresponding counterions[29]. In order to improve the selectivity of the multi-layer stacked GO membrane, et al. tried to decrease the interlayer spacing via the reduction of GO into reduced graphene oxide (rGO) [30]. In this case, researchers carried out several strategies to tune the interlayer spacing to accomplish the optimal ion selectivity. Since the pristine GO laminates possess natural nanocapillary channels around 0.7~1.1 nm[31], the interlayer spacing should be dedicated controlled The first strategy was inserting solid particles as intercalation to adjust the interlayer spacing. In this situation, GO sheets were supported by the intercalation to form a tent-shaped which allows water molecules to pass through. In work conducted by Gao et al., GO laminates were embedded with carbon nanodots of controllable sizes to tune the interlayer spacing[32]. Since the actual size of carbon nanodots is in the range of 1-8 nm, the as-prepared membrane was not designed to desalinate but to separate dyes from water, which showed 99% dye removal efficiency. Similarly, MnO_2 nanodots have also been tested as intercalation[33]. SWNT is another choice for intercalation [34]. GO/SWNT dispersions with different weight ratios were prepared following by diluting and vacuum filtration. The interlayer spacing was also too large to achieve water desalination even if the water

flux is 10-fold higher than the traditional NF membranes. On the other hand, dissolving the intercalations while maintaining the interlayer spacing could significantly increase the water flux[35]. By inserting and dissolving as-prepared 3-5 nm-size carbon hydroxide nanostrands in GO frameworks, the membrane exhibits 100 times higher water permeance than commercial UF membranes. Although the membrane is not proper for NF and RO desalination, the intercalation removal strategy is still inspiring.

An outstanding breakthrough in this method to achieve water desalination was presented by Liang Chen et al. in 2017[36]. They enlarged the interlayer spacing of graphene oxide sheets by inserting cations such as K^+, Na^+, Ca^{2+}, Li^+, and Mg^{2+}. The interlayer spacing was able to be fixed at 1.15 nm using KCl, which could steadily reject 99% Na^+ during the water desalination for an extended period. Although this membrane's water permeability was only about 0.36 L/ (m^2 h bar), it still provides a new vision for GO-based membrane for water desalination, which brings the GO framework membranes from UF and NF range to RO membrane. Since the tent-shaped structure inserts intercalations into GO sheets, the interlayer spacing is not uniform. The membranes also have the risk of swelling in water surroundings. Unfixed and non-uniform interlayer spacing will reduce both the ion selectivity and water permeability.

Compared with tent-shaped lateral nanochannel, tuning and fixing current GO interlayer spacing without inserting any intercalation is another bracket of the strategies. Quasi-uniform channels, which means the interlayer spacing is nearly even, can effectively reject the salty ions. Abraham et al. enlarged the interlayer spacing of GO laminates to ~1 nm by varying the humidity of the environment[37]. The ingenious

innovation of this research was used in the cross-sectional area for water desalination, where the membrane was encapsulated by epoxy so that the water flux could be as high as 5 L m^{-2} h^{-1}. Another bracket, consisting of covalent cross-linking, was used as intercalating materials to enlarge the interlayer spacing of GO[38]. The covalent bond, which is much stronger than Van der Waals force and hydrogen bond, provides more rigid interlayer spacing than solid intercalation to form quasi-uniform channels for water desalination. In an approach conducted by Hung et al.[39], the interlayer spacing of GO laminates was tuned by cross-linking with diamine monomers. By grafting different monomers with various molecular length (such as ethylenediamine (EDA), butylenediamine (BDA), and p-phenylenediamine (PPD)), the interlayer spacing between 0.87 nm to 1.04 nm in the dry state could be achieved. Cross-linked membranes also exhibit good rigidity of the d-spacing in the wet form. By the same cross-linking strategy, the GO-EDA membrane showed a high water permeability of 5.01 L m^{-2} h^{-1} bar^{-1} and around a 40% rejection rate for NaCl[40]. PDI (1, 4-phenylene diisocyanate) is another choice as cross-linker[41]. By modifying the Al_2O_3 tube with PDI, the membrane can be fabricated on the surface of the Al_2O_3 tube by vacuum filtration. In this case, the membrane can be worked on a load of the crossflow unit for desalination test while other membranes are only tested on the death-end unit. This design indicates that the GO-framework with quasi-uniform lateral channels has excellent potential for scaling up. Compared with different strategies, cross-linked GO membranes with quasi-uniform lateral channels exhibit a higher potential for better water desalination performance due to their fixed

interlayer spacing. However, the significant challenges of energy consumption and scalability still obstacle broadening the application of these techniques.

2.2 Environmentally-adaptive technologies for passive radiative cooling and heating

The human body, buildings, and vehicles etc. lose and absorb heat mainly in the form of IR radiation. The radiative thermal management can be achieved by tuning the transmission rate in the range of solar radiation band (i.e., 0.3-4 μm), atmospheric transparent window (i.e., 8-13 μm) as well as human body infrared (IR) radiation (7-14 μm in wavelength). Unlike all other available energy strategies, in which the waste heat is polluted into the surrounding environment, passive radiative cooling sends excessive heat to outer space at no additional energy cost[42-44]. In the previous research, scientists mainly focused on the radiative cooling effect in different materials[45-49].

In order to achieve radiative cooling, researchers are inspired by the natural phenomenon[50], such as frost and dew water formation on leaves[51], native silk[52], and silvery appearances of Saharan ants[53]. Based on the nature radiators, the membrane-based structure is a kind of strategy to achieve radiative cooling[54-62]. Czapla et al. [63] fabricated PDMS film on an aluminum substrate. They selectively radiated IR heat in the wavelength range of 8-13 μm, achieving as high as 12°C cooling in the ambient surroundings. Similarly, Hu et al.[64] inserted a conventional selective solar absorber between the polymer (PET) layer and the metal substrate to increase the emissivity in the solar spectrum and atmospheric window. In addition to organic materials, inorganic

coating, especially silicon-based materials, are also famous for IR absorber[65, 66]. Raman et al.[67] designed multilayer film consisting of seven alternating layers of hafnium dioxide (HfO_2) and SiO_2 with different thicknesses on the top of silver/silicon substrate. This structure could obtain radiative cooling to 5°C in the ambient surroundings and 40.1 W/m^2 net cooling power. Such multilayer films have been widely investigated for radiative cooling [47, 68-72].

Besides film-based structure, nanoparticle-filled material is another group of strategies for radiative cooling[73]. Bao et al.[74] generated scalable double-layer network filled with TiO_2 and SiO_2 nanoparticles. The reflectivity of such structure reaches 90.7% in the solar spectrum and 90.11% in the atmospheric window, which indicates 17°C cooling temperature theoretically. In 2017, Zhai et al.[48] embedded glass sphere (~10 μm) into polymer matrix for radiative cooling. The material of this layer was fully transparent for visible light but a strong emission within the atmospheric window, which provides ~110 W/m^2 cooling power in a continuous 3-day field test.

Another large group of strategies is patterned surface. Zhu et al. [75-78] designed different kinds of patterned structures for radiative cooling, such as α-quartz bars, pyramid structures, and square lattice air holes. All the systems showed high emissivity of the atmospheric window while remaining transparent for visible light. The reflection of visible light was achieved by the substrate coated by silver. Lu et al.[79] generated a universal routine for radiative cooling by adding ultra-broadband versatile membrane. Besides the experimental results, the simulation also directed the route of research. Wu et al.[80] demonstrated that the emissivity of pyramid structure and uniform structure is

significantly different, but the emissivity of the pyramid structures with different sizes are similar. However, these researchers focused on radiative cooling only, which cannot realize cooling or heating, responding to the environmental stimulus.

Self-adaptive radiative cooling based on phase change materials also attracts much attention[81, 82]. In 2017, Yi's group [83] designed a dual-mode membrane for both radiative heating and cooling by flipping between the inside and the outside layer. The membrane consisted of a high emissivity layer and a low emissivity layer. When the body felt hot, the high emissivity layer was placed inside to increase IR heat emissions. When the body felt cold, then the membrane was flipped over to reduce IR heat emissions. This technique can achieve both radiative cooling and heating, but it cannot manage the radiative heat automatically. Recently, Zhang et al. [84] reported dynamic gating for IR radiation, which tuned the emissivity radiative heat by controlling the contraction and relaxation of the smart membrane. This technique can achieve radiative heating and cooling by adjusting the transmissivity of body heat. But it is still very challenge to manage the IR heat from environment for cooling and heating, which is more significant for a radiative cooling and heating system.

Herein, the literature survey indicates no effort to fabricate a thermal-responsive pyramid structure for radiative cooling or heating. It is very challenging to achieve tuning the radiative cooling or heating automatically. Significant action is needed to investigate chemistry and physics for producing the thermal responsive pyramid structure for environmentally-adaptive membrane.

CHAPTER III

FULLERENE TAILORED GRAPHENE OXIDE INTERLAYER SPACING FOR WATER SUSTAINABILITY*

3.1 Introduction

Water resources are a vital element for a sustainable society[85]. Rapid population growth (1% growth rate per year) and industrialization have made freshwater shortage one of the most severe crises that threaten human beings[9, 86, 87]. Drinkable freshwater resources, mostly in groundwater and surface water, only occupy 1% of the total water resources on earth. This freshwater is necessary to maintain human life and be essential for social development, such as in agriculture, aquaculture, and power generation. The three elements of sustainable development are economic, environmental, and social. Global ecological concerns suggest that water resource development should pay more attention. Hence, desalination that can transform unconventional water sources (for example, seawater, brackish groundwater, and wastewater) into potable freshwater has become the most effective method to meet the global water crisis[9]. At present, the leading desalination technologies in use are based on membrane separation in terms of reverse osmosis (RO) and on thermal distillation, such as multi-stage flash (MSF) and

* Reprinted with permission from "Fullerene-Tailored Graphene Oxide Interlayer Spacing for Energy-Efficient Water Desalination" by Yuchen Liu, et. al, 2018. ACS Applied Nano Materials, 1, 11, 6168-6175, Copyright 2018 by American Chemical Society.

multi-effect distillation (MED). [7] Compared with thermal distillation, RO membranes desalination is more advantageous in energy efficiency, low environmental impact, and easy operation[9, 87]. However, the polymeric membranes currently used in conventional RO technologies suffer from low desalination capacity, fouling and flux decline under high pressure, and low tolerance to high temperature, acids/alkaline, chlorine, and organic solvents[88, 89].

Recently, nanostructures such as zeolites, metal-organic frameworks, ceramics, and carbon-based materials have attracted considerable attention as alternative membrane materials due to good chemical resistance, high flux, and high rejection rate[89-93]. Among them, graphene oxide (GO) membranes exhibit outstanding properties in molecular permeation and potential applications in water desalination, [19, 87, 91-96] and gas and ion separation, [97-101] due to their unique electronic properties, high tensile strength and impermeability to small molecules. For nanostructured membrane filtration, it requires nanopores or interlayer spacing with a fixed size of around 1 nm to let water pass through effectively while rejecting salt ions via size exclusion and electrostatic repulsion[37, 102]. Given the difficulty of assembling nanoporous graphene structures, controlling the interlayer spacing of GO sheets to be fixed around 1nm has become more practical and attractive[88, 92, 102].

A number of methods and intercalating materials have been developed to tune the interlayer spacing of GO sheets. Huang et al. fabricated nanostrand channels among graphene oxide layers by positively charged copper hydroxide nanostrands[35]. Another bracket, consisting of randomly distributed carbon nanotubes, was used as intercalating

materials to enlarge the interlayer spacing by Goh et al. [103]. Crosslinking with large organic materials can also tune the interlayer spacing via the different sizes of molecules[39]. Recently, Liang Chen et al. reported a novel strategy to crosslink the graphene oxide sheets by cations such as K+, Na+, Ca2+, Li+, and Mg2+[36]. The interlayer spacing can be fixed at 1.15 nm using KCl, which can steadily reject 99% Na+ during the water desalination for an extended period. Abraham et al. also tuned the interlayer spacing of the GO membrane to reach the 1 nm level by varying the humidity of the environment[37]. Moreover, they ingeniously used the cross-sectional area for water desalination where the membrane was encapsulated by epoxy so that the water flux can reach 5 L m^{-2} h^{-1}. However, these two most recent novel strategies have their limitations. The former can fix the interlayer spacing, but the water flux is too small, not cost-efficient for practical applications. The latter creatively enhanced the water flux by using cross-section, while the interlayer spacing is not sufficiently fixed since there is no physical bracket between GO layers. What's more, for brackish water desalination, the requirement on salt rejection rate is not as strict as that for seawater, while the water flux is more significant. The rejection rate of around 90% is sufficient to purify saline water with 10,000 ppm into freshwater.

In this work, the objective is to design and fabricate GO-based RO membrane to achieve higher energy-efficient water desalination, as shown in Fig. 3.1.1. The combination of the cross-sectional area filtration and continuous interlayer spacing adjustment to achieve water desalination was also introduced to the design. Fullerene (C60) is a carbon nanosphere with a diameter of about 0.7-1 nm[104], which is ideal for

tuning the interlayer spacing of GO for ion sieving purposes. It is an excellent strategy to fix the interlayer spacing of GO around 1.25 nm by grafting C60 on the surface of GO sheets to form the piers between GO sheets. Compared with other intercalations of GO layers for ion separation, such as cations and diamine monomers, the C60 molecule exhibits desired rigidity, which is essential to the feature of stability.

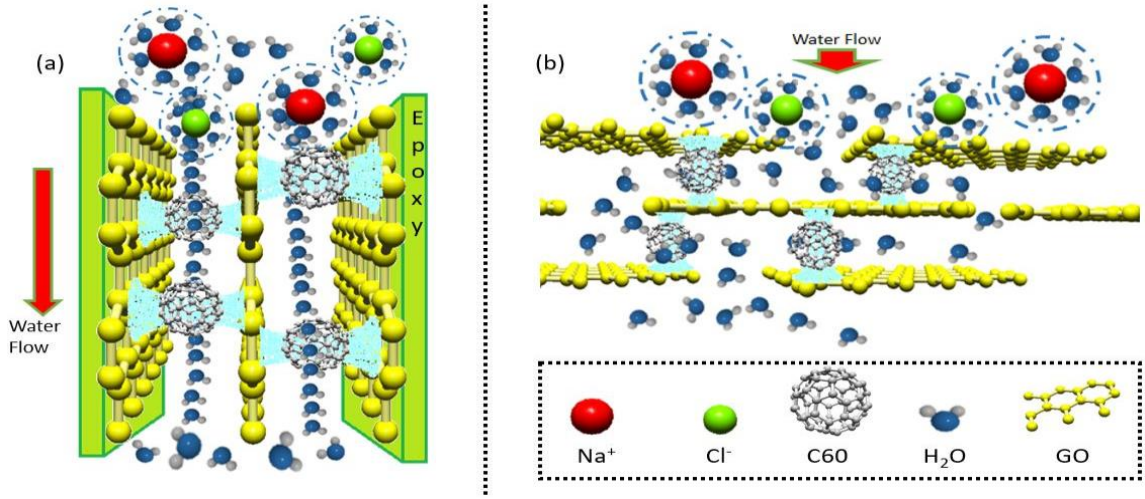

Figure 3.1. 1 Schematic representation of graphene oxide (GO) and fullerene (C60) hybrid for desalination process of (a) cross-sectional membrane and (b) flat membrane desalination. C60 was grafted between the laminates of GO. When the pressure is applied from the top side of the membrane, water passes through the membrane driven by the applied force while the membrane blocks the anion and cation.

3.2 Experiments

3.2.1 Preparation of C60-grafted GO

GO powders were prepared from graphite powder following modified Brodie's method according to our previous work[28, 105]. 500 mg of graphite was oxidized with a

mixture of 80 ml of nitric acid and 42.5 g of sodium chlorate and stirred at room temperature 24 hours. The sample was diluted with water and then neutralized with sodium hydroxide. Next, the sample was washed and collected by centrifugation to obtain graphite oxide. Graphite oxide was mixed with ammonia hydroxide to tune the pH value around 10-11 and was exfoliated into GO by ultrasonication for 2 hours. The exfoliated GO was collected by centrifugation at 5000 rpm for 30 minutes to remove the large sediment. Grafting C60 onto GO sheets follows the procedure as reported. [106] Briefly, 10 mg of dry GO was dispersed into 100 mL anhydrous toluene, which was also degassed in a Schlenk tube with the protection of nitrogen atmosphere. After two hours of ultra-sonication, 8 mL n-butyllithium in hexane (50 mL) was added dropwise and ultra-sonicated for another 2 h. After that, 10 mg (5 mg or 20 mg for different feed ratios) of C60 in 100 mL anhydrous toluene was added and sonication for 3 h. Then the mixture was kept under stirring overnight. To terminate the reaction, a droplet of methanol should be added to the mixture. In order to remove residual C60, the mixture was washed twice with toluene by 4000 rpm centrifuging for 30 min. Then the final powder was washed with methanol thoroughly by centrifuging repeatedly. Finally, the as-prepared C60-grafted GO was dried in a vacuum oven at 60 °C for 24 h.

3.2.2 Preparation of GO/C60 membrane

The membrane preparing process follows the procedure as reported. [37] Briefly, GO/C60 suspension was prepared via dispersing as-prepared C60-grafted GO in toluene

with the help of bath sonication for 2 h. Then the freestanding GO/C60 membranes were prepared by vacuum filtration of GO/C60 suspension via an Anodisc alumina filter membrane (200 nm pore size with 47 mm in diameter) followed by overnight drying in a vacuum oven at 60 °C. The membrane was then cut into 3 mm × 10 mm rectangular strips and encapsulated by epoxy (Epon 826 and CA 3300). If the GO/C60 layer was covered by epoxy, it should be cleaved carefully. Finally, the GO/C60 laminates were glued into a trough inside a plastic plate with 47 mm diameter and 2.5 mm thickness.

3.2.3 Characterization

XRD patterns were measured by X-ray diffraction (Bruker D8 ECO diffractometer) with a copper target (Kα1 radiation wavelength 1.54056 Å); zeta potential was measured by DelsaNano C with accessories; AFM images were collected by atomic force microscope (Bruker MultiMode 8); Microstructures were observed by transmission electron microscopy (TEM, JOEL JEM-2010); and electrical conductivity was measured by a conductivity meter (Horiba B-771 Twin Conductivity/Salinity Tester). The water desalination measurement experiment was operated by a homemade setup.[107] 50 mL saline water with 0.1 mol/L NaCl was added into the glass jar as the feed side. The permeant water was collected by a measuring cylinder covered by tin foil to avoid potential evaporation of water.

The salt rejection rate was calculated by the following equation:

$$R = \left(1 - \frac{C_p}{C_f}\right) \times 100\% \tag{3.1}$$

where C_p and C_f are the ion concentrations in permeate and feed side of solutions, respectively.

The water permeation flux J was calculated by the volume of the permeate side, passing through the membrane of cross-section area A in the period t. The equation was shown below: [107]

$$J = \frac{V}{At}[L/(m^2 h)] \tag{3.2}$$

In order to take the pressure issue into account, water permeance can also be defined as:

$$j = \frac{J}{P} = \frac{V}{PAt}[L/(m^2\ h\ bar)] \tag{3.3}$$

3.3 Results and Discussion

3.3.1 Water desalination mechanism for C60-grafted GO membrane

Before discussing the experiment results, the desalination mechanism for GO-based membrane should be clarified. The schematic diagram of the ions with large hydration diameter during passing through the membrane tunnel is shown in Fig. 3.3.1. Generally, the diameter of cations with larger hydration layers is more extensive than the interlayer spacing of GO layers. When the hydrated cations touch the edge of the GO layer, several water molecules in the outer hydration shell of the cations can be cut off by steric force that comes from GO layers. This process would be continued to the second hydration

shell of the ions until the width of the first hydration shell is narrower than the interlayer spacing of GO layers. Then the narrowed hydrated ions can pass through the GO layers. After the hydrated ion entirely passes through the GO layers, some other water molecules would take the defect position on the second hydration shell. Therefore, the critical issue is tuning the interlayer spacing of GO to exclude the salt ions in the water.

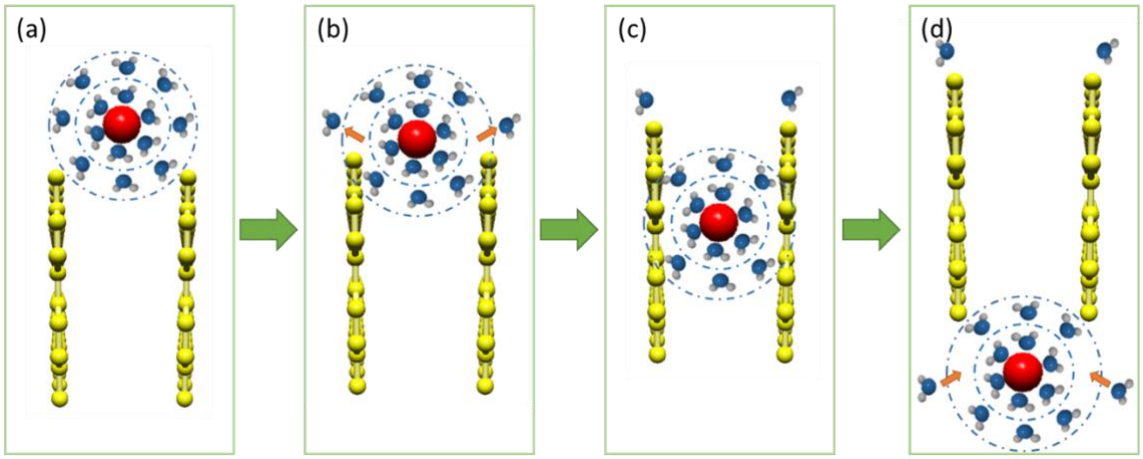

Figure 3.3. 1 Schematic diagram of the ions with large hydration diameter during passing through the membrane tunnel.

In the C60-grafted GO membrane, GO membrane is functionalized with negatively charged functional groups such as -COOH and -OH. Thus, anions (Cl^-) can be excluded at the entrance by electrostatic exclusion and steric effects, as shown in Fig. 3.3.2 (a) [108]. On the other hand, cations (Na^+) can only be excluded by the steric effects by the layer of GO. Precisely controlling the interlayer spacing of GO can balance the high ion rejection rate and the large water permeability.

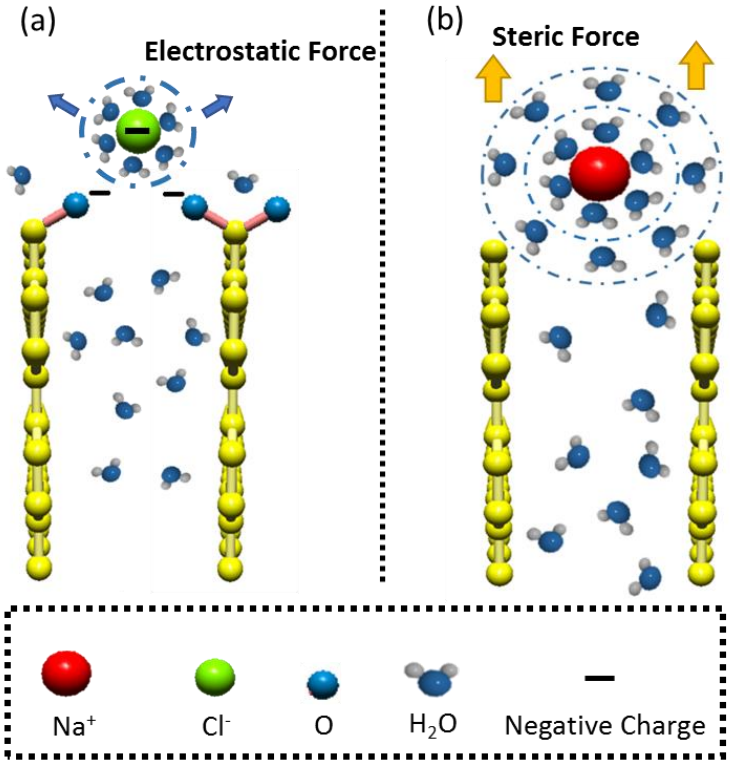

Figure 3.3. 2 Schematic illustration of the separation process of GO/C60 membrane at the entrance: (a) electrostatic exclusion for anions (Cl^-)[108, 109]; (b) steric effects for cations (Na^+)[110, 111].

3.3.2 Grafting C60 to GO and membrane fabrication

Before grafting C60 on the GO layer, the feed ratio of GO/C60 should be thoroughly calculated. Considering a monolayer GO as a beam, the relationship for bending rigidity and beam bending as shown in the following equations and Fig. 3.3.3 [112, 113]:

$$\delta = \frac{FL^3}{3D} \tag{3.4}$$

$$D = \frac{Eh^3}{12(1-\nu^2)} \tag{3.5}$$

where δ is the bending depth, F is the applied force which comes from the gravity of GO layers, L is the distance between two pillars, D is the bending rigidity of graphene, E is Young's modulus, h is the thickness of single-layer graphene, and v is the Poisson's ratio. According to the literature, the bending rigidity of graphene, D, is 2.31×10^{-19} Nm[114]. In order to fix the interlayer spacing of GO, the bending depth should be less than 0.1 nm. Then the theoretical distance between two C60 pillars can be calculated as ~5.21 nm.

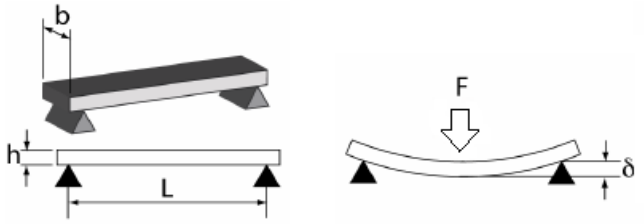

Figure 3.3. 3 Schematic of beam bending theory.

On the other hand, the weight of one C60 molecular is 1.197e-21 g. The weight of a single layer GO with a diameter of 5.21 nm is 8.1e-21 g. Hence, the minimum mass ratio of C60/GO is ~15%. In order to effectively tune the interlayer spacing of GO layers to avoid the mass ratio of grafted C60 less than 15%, the feed ratio of C60/GO is intentionally designed as 50% in minimum, i.e., the mass ratio of GO/C60 is 2:1.

GO was prepared by the modified Brodie's method[28, 105]. The detailed preparation processes are introduced in the Experiment Section. As-prepared single-layer GO was observed by AFM, as shown in Fig. 3.3.4. From the AFM image, the thickness of the GO layer is about 1 nm, which refers to a single layer GO.

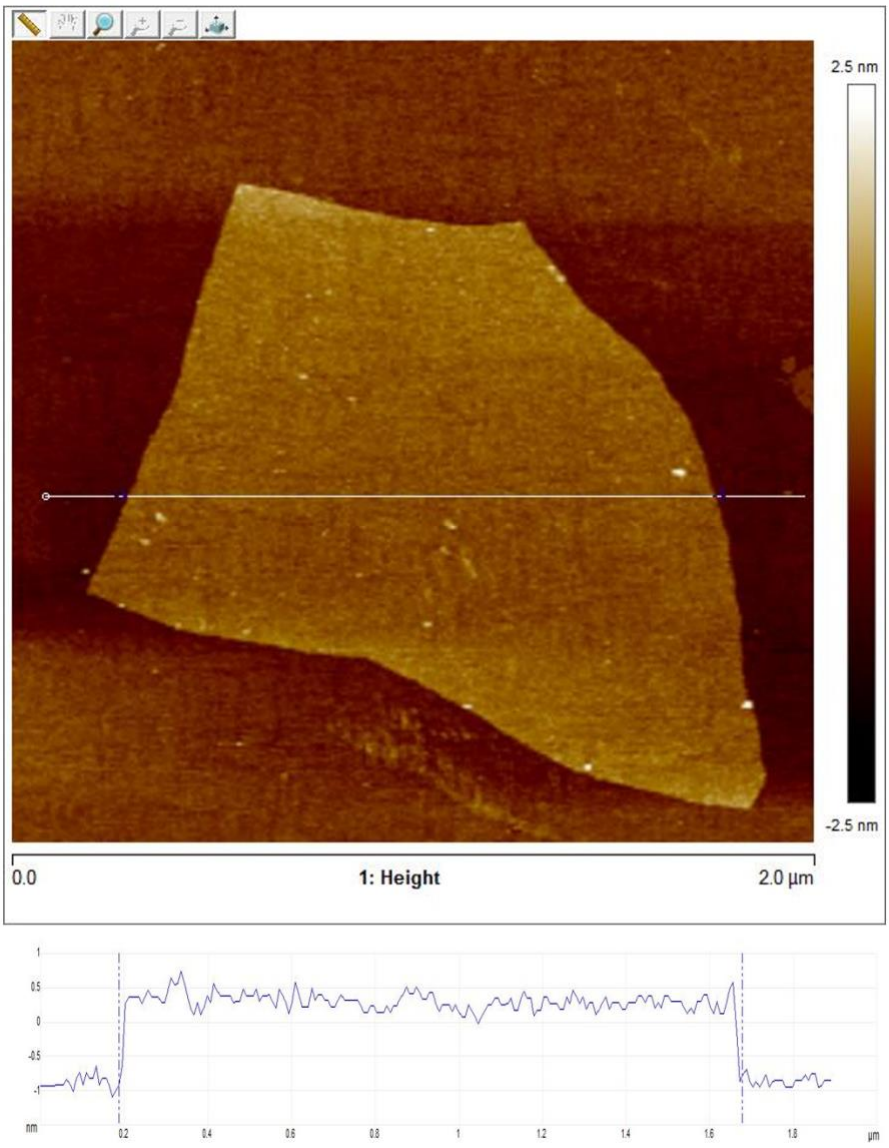

Figure 3.3. 4 AFM image of the single layer GO

Grafting C60 onto GO sheets follows the procedure as reported[106]. The detailed synthesis processes are stated in the Experiment Section. TEM images were taken to observe the C60 particles on the surface of GO layers. Fig. 3.3.5 shows the TEM images of pure single-layer GO (a) and C60-grafted GO layer (c), respectively.

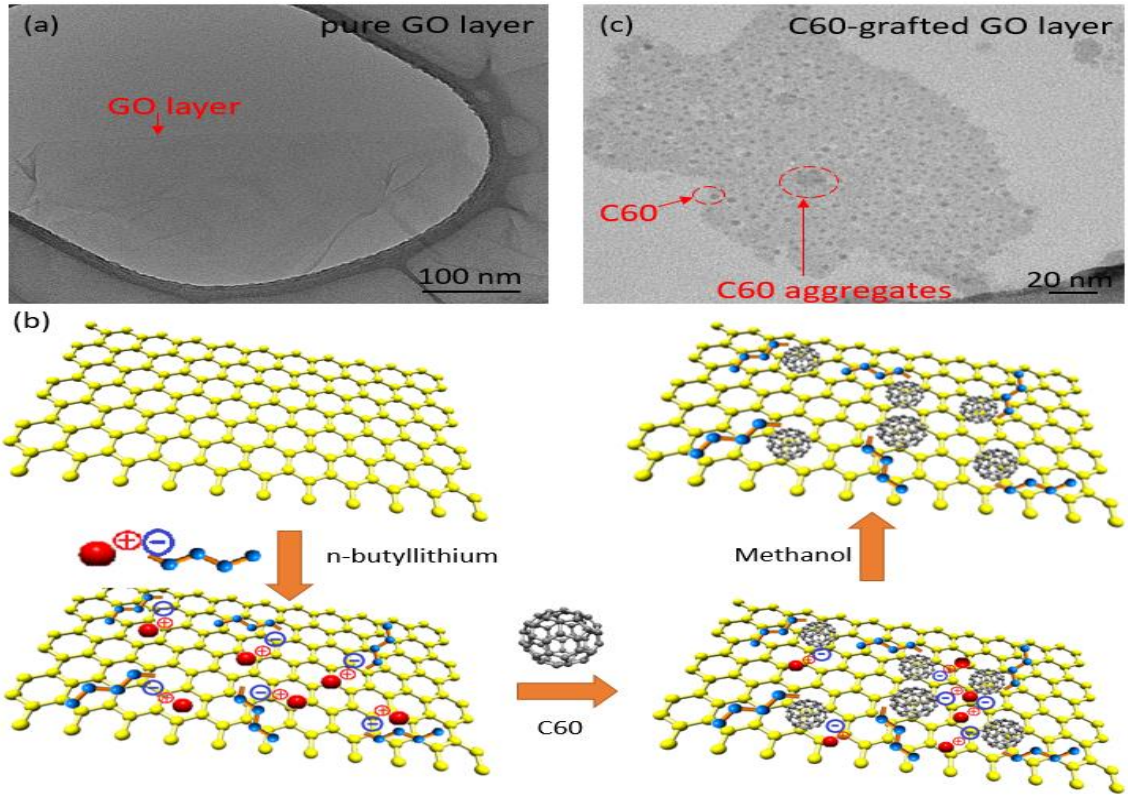

Figure 3.3. 5 (a) TEM image of pure GO layer (The skinny layer with a little bit folding edge represents GO layer. The scale bar is 100 nm.) (b) Schematic illustration of grafting C60 onto GO layer through lithiation reaction. (c) TEM image of C60-grafted GO layer. (The smooth layer with irregular shape represents the GO layer, and the dark dots represent C60 nanoparticles. The scale bar for this image is 20 nm. The size of this GO layer is around 150 nm while C60 nanoparticles are 1-2 nm.)

The membrane preparing process follows the procedure as reported[37]. GO/C60 suspension was prepared via dispersing as-prepared C60-grafted GO in toluene with the help of bath sonication for 2 h. The zeta potential of resultant solutions was also measured to understand the stability and nanomaterial distributions. At pH≈7.3, the zeta potential for the solution of pure GO and GO: C60=1:1 are -43.2 mV and -52.4 mV, respectively. The detailed fabrication processes have been noted in the Experiment Section. The GO

laminates produced by vacuum filtration were observed by SEM on the cross-section, as shown in Fig. 3.3.6.

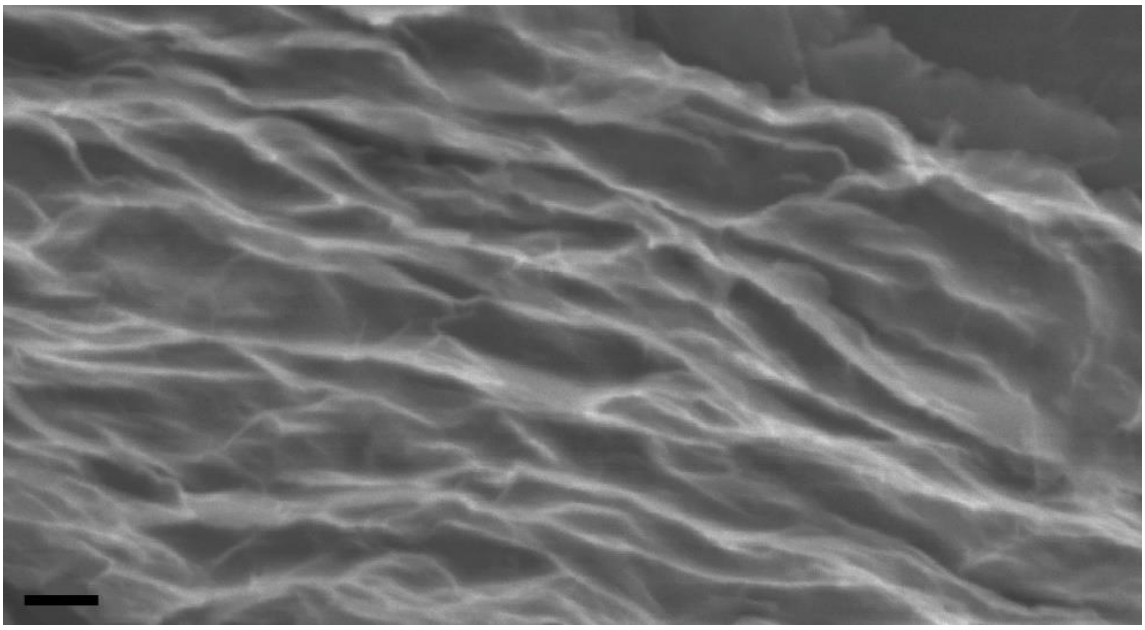

Figure 3.3. 6 SEM image of GO laminates. Scale bar 1 μm.

3.3.3 Membrane characterization and desalination test

To characterize the interlayer spacing of C60-grafted GO, X-ray diffraction was applied to the as-prepared samples. The interlayer spacing can be derived from the scattering angle (θ) by the following equation:

$$d = \frac{\lambda}{2\sin(\theta)} \tag{3.6}$$

where *d* indicates the interlayer spacing, λ is 1.54056 Å (wavelength of copper target) and θ is the scattering angle. As shown in Fig. 3.3.7, the peaks of samples with GO: C60 ratio of 2:1, 1:1, and 1:2 are located at 2θ of 7.038°, 6.977°, and 6.935° respectively, which

means that the interlayer spacing for corresponding feed ratio is around 12.5 Å, 12.6 Å and 12.7 Å respectively. The interlayer spacing was caused by C60 molecules (average diameter of 7 Å) and the C-C bonds of N-butyl on both sides of the graphene layer (each N-butyl is around 3 Å). From Fig. 3.3.7, the effect of C60 fraction on the interlayer spacing is tiny because the C60 fraction was above the threshold (15 wt.%) as calculated in the previous section. When the feed ratio of GO/C60 is between 2:1 and 1:2, the GO layer could not bend over 0.1 nm, and the C60 molecules could not aggregate, either. On the other hand, the tiny deceasing of interlayer spacing as the feed ratio of C60 decreases come from the spacing shrinking. The GO layer is bending to increase the distance among C60 piers. For comparison, the interlayer spacing of pure GO (without C60 grafting) was also tested by XRD which is 7.67 Å, as shown in Fig. 3.3.7. The interlayer spacing of pure GO, compared with C60-grafted GO, is too small to achieve a high water-permeation rate. Furthermore, the interlayer spacing of pure GO can be significantly influenced by water flow and be damaged due to swelling and folding, which results in low stability for applications.

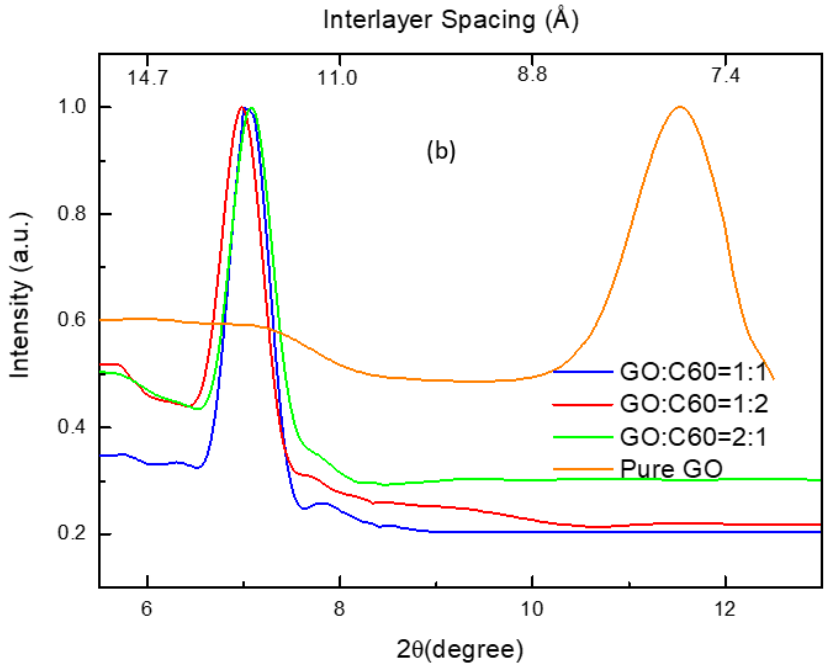

Figure 3.3. 7 XRD characterization: XRD pattern of as-prepared GO/C60 membrane and pure GO membrane, where the red, blue, and green lines indicate the feed ratio of GO: C60 = 1:2, 1:1, and 2:1 respectively, and the orange line represents the pure GO; The peak of C60-grafted GO is around 7° which means 12.5 Å in interlayer spacing. On the other hand, the pristine GO peaks at 11.5°, indicating 7.7 Å in interlayer spacing.

After tuning the interlayer spacing of GO membranes to the desired value of around 12.5 Å by grafting C60 on the surface of GO layers, the membrane can be used for water desalination. Fig. 3.3.8 shows the GO/C60 membranes fabrication process and water desalination setup. The ion permeation measurement experiment was operated by the setup device shown in Fig. 3.3.8 (f). The whole apparatus was using under magnetic stirring to avoid the influence of concentration polarization effect on the feed side. 50 mL saline water with 2000 ppm NaCl was added into the glass jar as feed side. The permeant water was collected by a 5-mL measuring cylinder (accuracy 0.05 mL, from Sigma

Aldrich), which is covered by tin foil to avoid potential evaporation of water. All the measurement results except the stability test were determined by 2-hour tests.

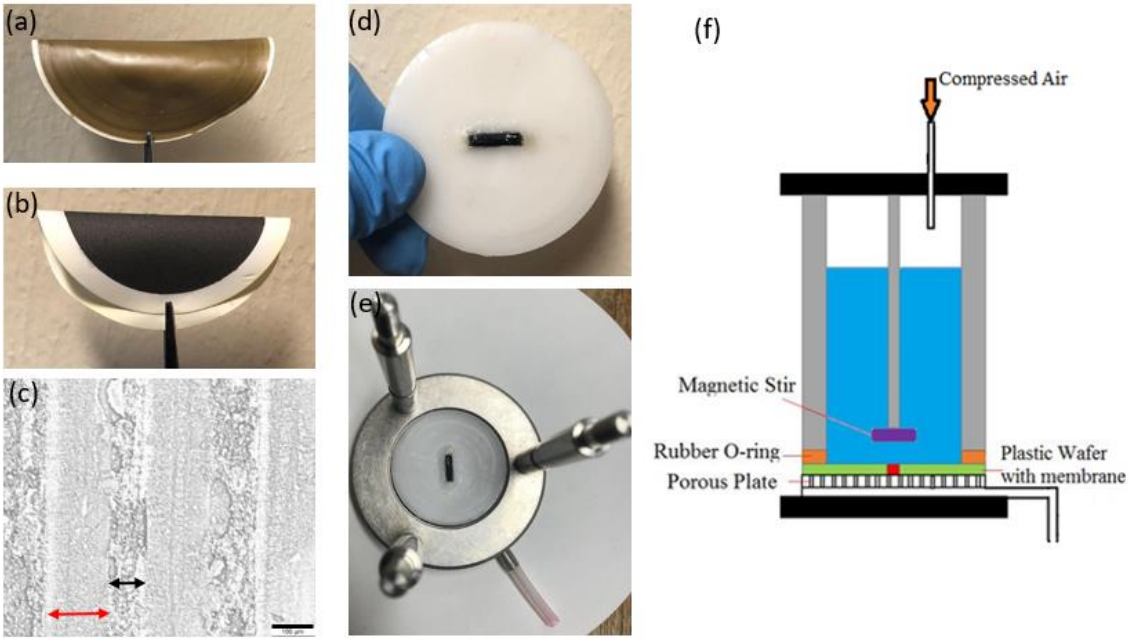

Figure 3.3. 8 GO/C60 membranes fabrication process and water desalination setup. (a) Photograph of pure GO membrane. (b) Photograph of C60-grafted GO membrane (c) Optical micrograph of the cross-sectional area, which shows 148-µm-thick GO laminates (red arrow) embedded in 81-µm thick epoxy (black arrow). Epoxy and GO/C60 layers are labeled in the figure. The scale bar is 100 µm. (d) Photograph of GO/C60 membrane encapsulated with epoxy and glued into a rectangular slot within a plastic disk of 47 mm in diameter. (e) Photograph of GO/C60 membrane inside the water desalination setup. (f) Schematic of water desalination setup.

Ion permeation results of aqueous 0.1 mol/L NaCl filtrated using different GO: C60 membranes are illustrated in Figures 3.3.9 and 3.3.10. As shown in Fig. 3.3.9, the ion permeation rate shows a linear relationship as a function of the applied pressure difference between the feed and the permeation sides. Compared with Abraham's work[37], which exhibited the Na^+ permeation rate of 0.033 mol h^{-1} m^{-2} bar^{-1}, this C60-grafted GO membrane shows about five times higher ion permeation rate because of the larger

interlayer spacing (12.6 Å) than that of the reported humidity-tuned GO membrane (9.6 Å). For GO: C60 = 1:1 membrane, the ion permeation rate jumped from 0.106 mol h^{-1} m^{-2} bar^{-1} to 0.188 mol h^{-1} m^{-2} bar^{-1} as the pressure increased from 1 bar to 5 bar. At the same pressure changing range, the salt rejection rate decreased from 89.66% to 82.65% because high pressure drives higher forces on the ions to overcome the energy barrier at the entrance of membranes.[115] On the other hand, the vertical difference for different lines in Fig. 3.3.9 indicates the ion permeation difference among various membranes, which comes from the difference in the density of C60 molecules. As the concentration of C60 increases, the steric effect for salty ions inside GO layers gets larger. At 5 bar pressure, as the GO: C60 ratio decreased from 2:1 to 1:2, the rejection rate increased from 79.40% to 83.16%. For the saline water with 0.1 mol/L NaCl (5,850 ppm), the 83.16% rejection rate means that the C60-grafted GO membrane filtrated water can be as low as 985 ppm, which can be regarded as freshwater. The difference in ion rejection rate shown in Fig. 3.3.9 (b) comes from the amount of C60 piers between GO layers instead of the 0.1 Å difference of interlayer spacing. The water permeation flux (J), as expected, increases linearly with the applied pressure. If the pressure issue is taken into account, the relationship between the water permeance (j) and the applied pressure is shown in Fig. 3.3.9. The water permeance of GO: C60 = 1:1 membrane increases from 10.21 L h^{-1} m^{-2} bar^{-1} to 10.85 L h^{-1} m^{-2} bar^{-1} as pressure changes from 1 bar to 5 bar. The other two membranes also show this trend. This pressure-induced enhancement subjects to the increase of water molecule kinetic energy to overcome the energy barrier of entry. The slightly vertical difference among different membranes in Fig. 3.3.9 comes from the difference of interlayer spacing and

C60 piers concentration. For the membrane with a larger concentration of C60, the effective cross-sectional area for water molecule passing through gets smaller, which results in lower water flux. Besides, compared with the water permeation rates, the ion permeation ratio changes among different pressures are much smaller, indicating that salty ions are more sensitive to the applied pressure than water molecules.

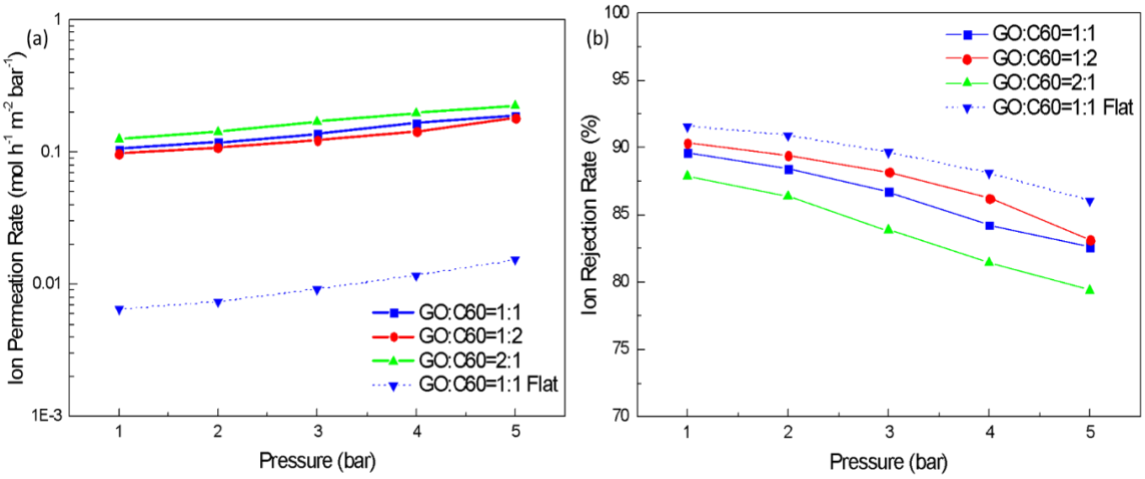

Figure 3.3. 9 (a) Ion permeation rate and (b) Ion rejection rate through GO/C60 membrane with different pressure applied. The red, blue, and green lines indicate the feed ratio of GO: C60 = 1:2, 1:1, and 2:1, respectively. The dashed line indicates the feed ratio of GO: C60=1:1, which uses the flat surface for desalination.

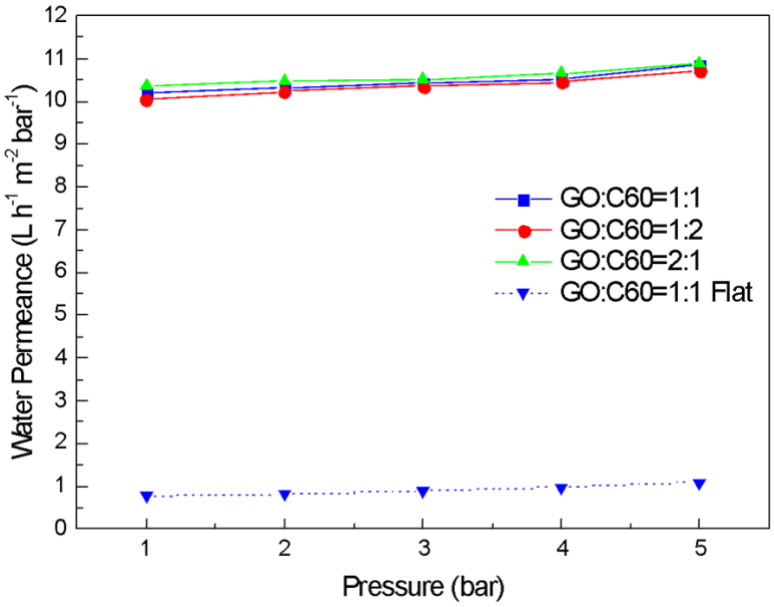

Figure 3.3. 10 Water permeation rate through GO/C60 membrane with different pressure applied. The red, blue, and green lines indicate the feed ratio of GO: C60 = 1:2, 1:1, and 2:1, respectively. The dashed line indicates the feed ratio of GO: C60=1:1, which uses the flat surface for desalination.

Accordingly, most reported GO membranes could be effectively used for ion separation for 5 h to 10 h[36]. The stability of the C60-grafted GO membrane was also indicated. As shown in Fig. 3.3.11, the ion concentration of water after passing through pure GO membrane increased rapidly from 2 h to 10 h and then became stable. Even at the 2-hour-test experiment, the ion rejection rate of pure GO is still more extensive than those of C60/GO groups, which indicate the interlayer spacing of pure GO has already changed at the 2-hour test. In contrast, after passing through the C60-grafted GO membrane, the water remained at a low ion concentration value, which indicated the high stability of the C60-grafted GO membrane. Among the C60/GO groups with a different feed ratio of C60, the higher C60 feed ratio groups exhibited higher membrane stability. Compared with the pure GO membrane, C60-grafted GO membranes demonstrate strong

covalent bonds, which is more vital than hydrogen bond and can fix the interlayer spacing at around 12 Å without swelling in water. The higher feed ratio of C60 exhibits a larger interlayer covalent bond resulting in higher stability and durability.

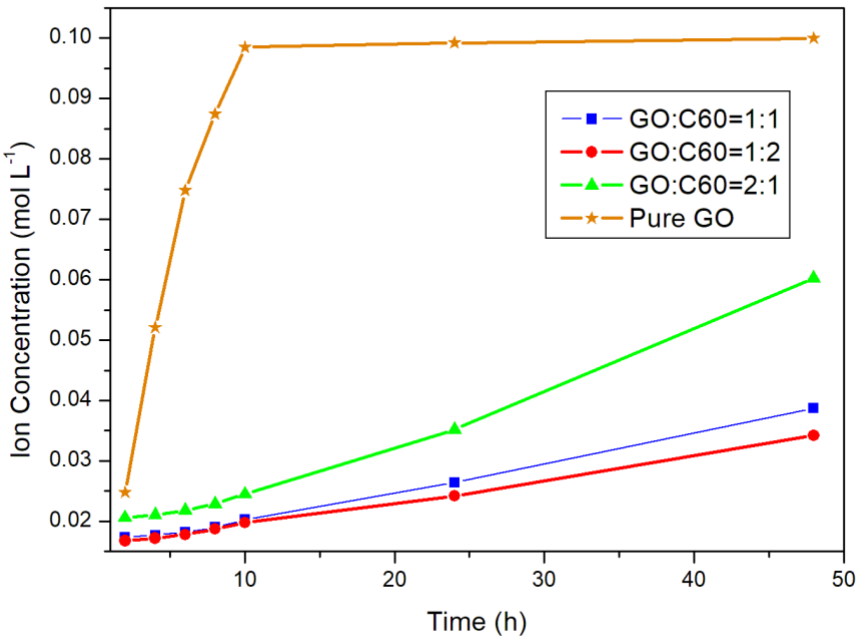

Figure 3.3. 11 Ion concentration on the permeation side through GO/C60 membrane over the period. The red, blue, and green lines indicate the feed ratio of GO: C60 = 1:2, 1:1, and 2:1, respectively.

Energy efficiency is another critical factor besides water separation performance, including water permeance, ion rejection rate, and stability. The operating pressure of most separation membranes is comparatively higher, which will significantly increase operational costs[91]. The separation performances and energy consumption of some membranes recently reported in the literature and the C60 grafted GO membranes prepared in this study are summarized in Table 3.1. It can be seen that under low operating

pressure (<5 bar) C60 grafted GO membranes exhibit excellent water flux and comparable rejection rate compared with most reported works. This phenomenon is because the grafted C60 can act as piers to fix the interlayer spacing of GO laminates at 12.5 Å, allowing water molecules pass through fluently while hindering cations (Na^+) and anions (Cl^-) at the entrance via electrostatic exclusion and steric effects[108]. Besides, by adopting a novel cross-sectional filtration strategy, these GO/C60 membranes can obtain a higher effective filtration area to achieve a high water-flux. C60-grafted GO membranes show not only outstanding water desalination performance, excellent long-term stability as well as low energy consumptions.

Table 3. 1 Comparative Results of Different Nanofiltration Membranes

Membrane	NaCl Concentration (mol/L)	Pressure (bar)	Equivalent Water Permeance (L/ m2 h bar)	Energy Consumption at 0.1M NaCl(kWh /m3)	Rejection Rate (%)	Ref.
GO/C60 (1:1)	0.01	2.00	13.76	0.94	88.46	This study
CNT/ PMMA	0.034	10.00	0.04	110.59	40.00	[116]
CNT-PA	0.034	15.50	3.40	1.20	97.00	[117]
KCl-controlled GO (280nm)	0.25	20.00	0.05	104.73	94.67	[118]
GO-PA (0.015wt%)	0.034	20.50	3.16	1.20	93.80	[119]
PEI/GO (1 bar)	0.00862	1.00	10.65	2.72	42.00	[120]
GO-NHS /EDC/PA	0.05	27.60	1.59	2.25	97.80	[121]
GO-PA	0.034	15.00	2.22	1.85	97.00	[122]
rGO/TiO2	0.034	15.00	3.85	1.07	99.45	[123]

Table 3. 1 Continued

Membrane	NaCl Concentration (mol/L)	Pressure (bar)	Equivalent Water Permeance (L/ m2 h bar)	Energy Consumption at 0.1M NaCl(kWh /m3)	Rejection Rate (%)	Ref.
PA/MPDA/ BTAC	0.034	15.50	3.02	1.35	99.10	[124]
PA/DAT/TMC	0.5983	35.00	1.71	3.37	98.30	[125]
PI/MPDA	0.034	15.00	2.41	1.71	98.80	[126]
PA/MPDA/ PTC/TMC	0.0256	13.80	4.32	0.97	93.00	[127]
PA/Silica	0.188	44.00	1.38	2.48	90.00	[128]
PEI/Silica	0.034	15.00	1.35	3.05	92.00	[129]
PA/ SMWNT	0.034	16.00	1.65	2.45	90.00	[130]
CDC/PA	0.034	14.15	1.36	3.07	97.80	[131]
PA-NGOOD	0.034	15.00	1.92	2.15	95.00	[132]
PA/TiO2	0.034	20.70	3.42	1.11	96.00	[133]
AqpZ-DOPC	0.01	5.00	4.44	1.42	97.00	[134]
Aqpz-ABA	0.0034	5.00	4.74	1.28	61.00	[135]
Zwitterion-CNT	0.034	24.10	1.12	3.28	98.00	[136]
NH2-MWCNT	0.034	15.00	4.36	0.95	96.00	[137]
Oxidized MWCNT	0.034	15.00	2.17	1.90	97.40	[138]
GO in RH 84%	0.1	15.00	0.45	10.00	97.78	[139]
TFC/EDAD MBSA	0.017	15.50	1.79	2.24	96.00	[140]
PA/MPDA/ TMC	0.034	15.50	1.78	2.29	99.90	[141]
MWNT/ TNT	0.034	15.00	0.83	4.94	97.97	[142]
aPES/ aTMA-PA	0.547	55.00	1.36	2.61	98.80	[143]

3.4 Summary

In conclusion, C60-grafted GO membranes can effectively sieve ions from salty water due to the electrostatic exclusion and steric effect, holding a high ion rejection rate of 89.66% with 10.21 L h^{-1} m^{-2} bar^{-1} water flux at 1 bar applied pressure. By adopting a novel cross-sectional filtration strategy, these GO/C60 membranes can obtain a high water flux up to 10.85 L h^{-1} m^{-2} bar^{-1} with 0.1883 mol h^{-1} m^{-2} bar^{-1} ion permeation rate at 5 bar applied pressure, which is around 10 times better than the flat GO/C60 membranes. Furthermore, the as-prepared GO/C60 membranes can work at low pressure (<5 bar) and show high stability over a long-time period, indicating a high potential for saline water desalination applications.

CHAPTER IV

SCALABLE GRADIENT GRAPHENE OXIDE NANOSTRUCTURE FOR WATER SUSTAINABILITY*

4.1 Introduction

As mentioned above, freshwater resource plays a key role for sustainable development. Reverse Osmosis (RO) desalination is a water purification process that uses a semi-permeable thin membrane to pass pure water while rejecting the salts and other impurities[3]. Compared with thermal distillation and other desalination methods (including ion-exchange membrane processes, freezing desalination, geothermal desalination, eletrodeionisation (EDI), and solar desalination), RO desalination shows excellent advantages on the continuous process, mild working condition, low environmental pollution, and easy operation[7, 9]. Over 65% of the current installed desalination capacity is based on the RO membrane process[8]. However, one of the most significant barriers for extending RO desalination technology to broader applications is the intensive energy consumption of the RO unit, which represents 50%-60% of the total cost of the whole desalination process[10]. In a typical seawater desalination plant that purifies Pacific Ocean water with total dissolved solids (TDS) of 33.5 g/L (33,500 ppm),

* Reprinted with permission from "Water purification performance and energy consumption of gradient nanocomposite membranes" by Yuchen Liu, et. al, 2020. Composite Part B: Engineering, 202, 1, 108426, Copyright 2020 by Elsevier Ltd..

the overall energy consumption is 3.57 kWh/m^3, and the RO unit accounts for 71% of this total energy consumption[144]. Besides the seawater, brackish water is another source for portable water recovery. U.S. Geological Survey indicated that brackish groundwater could help stretch limited freshwater supplies[145]. For brackish water RO desalination, the salt rejection rate requirement is not as strict as that for seawater due to a lower ion concentration. The rejection rate of ~90% is pretty decent in converting brackish water into fresh water. Generally, the specific energy consumption (SEC) during the RO desalination process can be broke down into filtration resistance energy-consumption (SEC_f), which is related to the performance of the RO membrane, and other energy consumptions that are influenced by the system process and the feed water osmotic pressure[146]. Under the same RO desalination operating systems and feed salinity, the energy consumed by SEC_f is the central part that can be reduced. This part of energy is one of the most important criteria to evaluate the performance of a RO membrane. The energy consumption in the membrane filtration process can be ascribed to the steric effect and friction losses. Herein, reducing the steric effect and friction losses of water molecules from hydrodynamic theory is a very promising strategy. Although the water molecule transportation mechanism through nanochannels is not precise[147], the water permeance was negatively related to the length of the water-transport pathway, and the salt rejection rate depends on the stability of nanochannels[148].

Commercial RO membranes are mainly made of polyamide (PA) thin composite film (TCF) and its derivatives, which suffer low water permeability, high energy consumption, high fouling tendency, and limited lifetime[149]. Even though some efforts

have been made, current RO membranes used in desalination are still suffering intensive energy consumption and low energy-efficiency. Emerging selectively permeable membranes with sub-nanometer channels attract considerable attention for energy-efficient desalination[15-17]. A lot of nanomaterials, such as zeolites, metal-organic frameworks (MOF), ceramics, graphene, carbon nanotubes, and aquaporin (AQP), have been attempted to fabricate RO membranes[89-93, 150, 151]. Among all kinds of nanomaterials, graphene oxide (GO) has emerged as the most attractive one for water desalination because of outstanding antifouling and barrier performance in molecular separation due to its unique molecular structure, high tensile strength, and impermeability to small molecules.

In this work, a nanocomposite membrane consisting of ultrathin GO laminates with 1-nm channels and two porous cellulose layers is presented to achieve both energy efficiency and scalability for RO desalination. The GO laminates thickness and GO nanosheet lateral size were studied to reduce energy consumption while maintaining the water desalination performance. The stability and lifetime of the gradient GO membrane were also discussed at such low energy consumption. Finally, the scalability of the gradient structure is also presented to examine the potential of commercialization.

4.2 Experiments

4.2.1 Numerical simulation

The ‘Transport of Diluted Species in Porous Media’, ‘Thin-Film Flow, Domain’, and ‘Fluid-Solid Interaction’ physics models in COMSOL were applied to simulate the ion/water separation process and stress distribution in the membrane. The simulation cell for the aperture selection of the protective layer was rectangular with a fixed thickness of 10 nm and a varied width ranging from 25 nm to 200 nm. The fluid domain was also rectangular with a height of 30 nm and the same width as the membrane. The input pressure, density, and dynamic viscosity of seawater were set to 1 MPa, 1.03×10^{3} kg/m^{3}, and 8.9×10^{-4} Pa·s, respectively. The Young’s moduli of thin membranes were measured by DMA 850(TA Instruments) in the tensile mode. The simulation cell for the protective layer was rectangular with a height of 20 nm and a width of 200 nm. The porosity domain as the protective layer on the GO membrane was also rectangular with a 200 nm width and different thicknesses. The porosity of the protective layer was set to 70%, according to the commercial data.

4.2.2 Preparation of gradient nanocomposite membrane

According to our previous work, GO powders were prepared from graphite powder following modified Brodie’s method[152]. 500 mg of graphite was oxidized with a mixture of 80 ml of nitric acid and 42.5 g of sodium chlorate and stirred at room temperature 24 hours. The sample was diluted with water and then neutralized with sodium hydroxide. Next, the sample was washed and collected by centrifugation to obtain graphite oxide. Graphite oxide was mixed with ammonia hydroxide to tune the pH value

around 10-11 and was exfoliated into GO by ultrasonication for 2 hours. The exfoliated GO was collected by centrifugation at 5000 rpm for 30 minutes to remove the large sediment. 5 mg of as-prepared dry GO powder was dispersed into 100 mL DI water, and a droplet of ammonia solution was added to the GO dispersion to tune the pH value to 10-11. After 30min bath sonication, GO dispersion was centrifuged at 4400 rpm for 20 min to remove large particles. The amplitude and power density of the tip sonicator were set to 25 % and 12.5 W/mL, respectively. Subsequently, the GO dispersion was treated by tip sonication for 0 min, 3 min, 10 min, and 20 min, resulting in GO nanosheets with a lateral size of1430 nm, 1009 nm, 473 nm, and 276 nm, respectively. 0.01 M PPD was then added to the resultant GO dispersion under stirring. The resultant GO-PPD dispersion (e.g., 2 mL, 4 mL, 6 mL, or 8 mL) was pumped through an MCE filter membrane (25 nm aperture size with 47 mm in diameter) to produce GO/MCE membranes, where the GO film thickness was dependent on the GO-PPD dispersion volume. The resultant 2-layered GO-MCE membrane was then covered by another MCE filter membrane and pressed by a Heat Presses (Digital Knight, K20 SP) at 80 °C with 20 psi pressure for 1 h.

4.2.3 Characterization

Zeta potential of GO dispersion was characterized by Dynamic Light Scattering (Zetasizer Nano ZS). GO nanosheet lateral size was measured by Dynamic Light Scattering (Zetasizer Nano ZS) and atomic force microscope (AFM, Bruker MultiMode 8) in tapping mode. The tensile strengths of GO films were tested by Dynamic Mechanical

Analyzer (TA Instruments, Q850 with accessories). The GO sample for the AFM characterization was prepared by the following steps. Firstly, the GO dispersion was diluted with 10-times DI water. Then a droplet of diluted GO dispersion was dropped on a clean silicon wafer followed by blowing dry with nitrogen. X-ray diffraction (XRD) characterization of the MCE/GO membrane was carried out by Bruker D8 ECO diffractometer with a copper target (Kα1 radiation wavelength 1.54056 Å). ATR-FTIR characterization was carried out by the ATR-FTIR spectrometer (Bruker Alpha-Platinum). The MCE/GO/MCE gradient membrane was dipped into a plastic tube of epoxy resins for 24 hours, and then the samples were encapsulated by the cured epoxy resin. The plastic cube was then cut by a waterjet cutter, and the cross-section was characterized by scanning electron microscopy (SEM, JEOL JSM-7500F).

4.2.4 Desalination Test

The water desalination tests were carried out by an in-house built system, as shown in Figure 4.2.1 (a). Specifically, 40 mL saline water with 2000 ppm NaCl was added to the feed side. The applied pressure on the feed side was 2.68 bar. The permeant water was collected by a measuring cylinder, which is sealed by tin foil to avoid potential evaporation of water. Electrical conductivity was measured by a conductivity meter (Horiba B-771 Twin Conductivity/Salinity Tester).

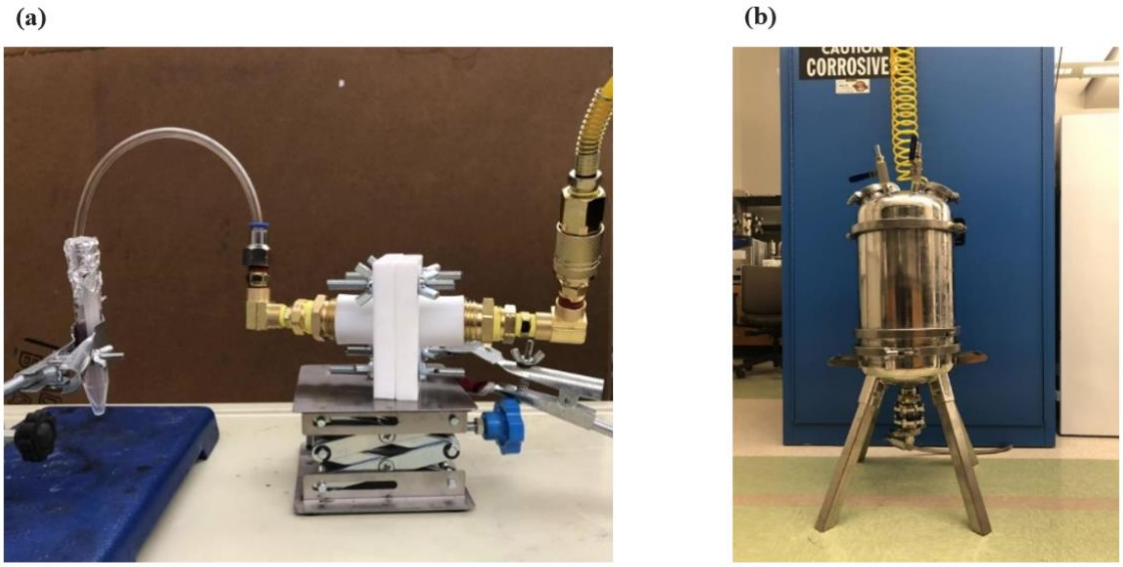

Figure 4.2. 1 Setup for (a) water desalination test and (b) large scale membrane fabrication.

Total Dissolved Solids (TDS) and electrical conductivity (EC) of the saline water can be calculated using the following equation:

$$TDS(mg/L) = k \cdot EC(\mu S/cm) \tag{4.1}$$

where k is the TDS factor for the solutions.

For NaCl solution, k = 0.48 ± 0.01 when the EC is in the range of 100-2000 μS /cm at the temperature of 25℃. Since the solute in the solution is NaCl only, the TDS can be converted to the ion concentration of NaCl solution by the following equation:

$$TDS(mg/L) = C(mol/L) \cdot M(mg/mol) \tag{4.2}$$

$$C(mol/L) = \frac{k \cdot EC(\mu S/cm)}{M(mg/mol)} \tag{4.3}$$

where C is the ion concentration of the solution, M is the mole mass of the solute, which is 58,440 mg/mol for NaCl.

The salt rejection rate was calculated by the following equation:

$$R = \left(1 - \frac{C_p}{C_f}\right) \times 100\% \quad (4.4)$$

where C_p and C_f are the ion concentrations in permeate and feed side of solutions, respectively.

4.2.5 Scale-Up Demonstration

The large-size membrane was fabricated by a homemade setup, as shown in Figure 4.2.1 (b). As-prepared scale-up GO/MCE membrane was also bonded by another MCE membrane to form the gradient structure with the same steps mentioned above. The resultant large-size membrane was cut to 47 mm disks for desalination tests.

4.2.6 Energy Consumption Calculation

The overall energy consumption for RO desalination is contributed by the RO filtration process and other processes (e.g., pretreatment of water, etc.), not related to the RO membrane. In this study, the energy consumption related to other processes was regarded as the fixed to reveal the energy consumption of gradient nanocomposite membranes. The energy consumption contributed by the sole RO filtration process

disclosed the performance of the water desalination process and was defined as the filtration resistance energy-consumption of the specific energy consumption (SEC_f). The SEC for seawater desalination is 3.57 kWh/m^3, and the SEC_f accounts for 71% of it. On the other hand, although a lot of research has been done to investigate the water permeability of various membranes, it was challenging to compare their performance due to different test conditions, such as feed salinity, salt composition, or applied pressure. Therefore, it is essential to generate a unified criterion to quantify the energy consumption for different RO membranes. Here, a unified model was established to quantify the energy consumption for a given RO membrane with given water permeability, feed salinity, feed flow, and feed pressure. The output for the model focuses on the SEC_f. This model can be used for both seawater (SW) and brackish water (BW). The only difference is the feed salinity concentration.

From the very beginning, according to empirical studies and molecular dynamics simulation, the water flux can be expressed as[153]:

$$J = [P - (\pi_f e^{J/k} - \pi_p)] \cdot A_m \tag{4.5}$$

where π_f and π_p are osmotic pressure of the feed side and the permeate side, respectively, A_m is the water permeability of the membrane, and k is the mass transfer coefficient. The factor $exp(J/k)$ indicates the effect of concentration polarization. Here, we assume the feed side can be regarded as pure NaCl salinity without any other salts and particles. The osmotic pressure of the permeate side can be ignored due to its low ion concentration compared with the feed side. Since the water flux J is related to the position of RO

desalination vessels Z, the Eq. 4.5 can be extended to a function related to the position variable *z*:

$$\mathrm{J(z) = (P(z) - \pi_f(z)e^{J(z)/k(z)}) \cdot A_m} \tag{4.6}$$

According to van't Hoff's Law,

$$\mathrm{\pi(z) = C_b(z)RT} \tag{4.7}$$

$$\mathrm{J(z) = Am \cdot P(z) - k(z)w(\frac{2C_b(z)e^{\frac{A_m P(z)}{k(z)}} A_m T}{k(z)})} \tag{4.8}$$

where *w(x)* is the Lambert W function, and its values are readily computed by Mathematica 9.

The water flow rate that has permeated ahead of position z can be expressed as:

$$\mathrm{\Phi(z) = \frac{W_c}{Q_{in}} \int_0^z J(z)dz} \tag{4.9}$$

where W_c is the effective width of the membrane and Q_{in} is the feed flow.

According to the literature, the mass transfer coefficient *k* can be regarded as a constant with a given height of the channel, feed flow, salt diffusivity, fluid viscosity, and fluid density[153]. Therefore,

$$\mathrm{\Phi'(z) = \frac{W_c}{Q_{in}} J(P(z), Q(z), C_b(z))} \tag{4.10}$$

$$\mathrm{Q(z) = Q_{in}(1 - \Phi(z))} \tag{4.11}$$

$$\mathrm{C_b(z) = \frac{C_{b0}}{1-\Phi(z)} \cdot \frac{dP}{dz} = -P'_{lost}(z)} \tag{4.12}$$

where P_{lost} is the pressure losses from the entry position to the exit position. Combining the Eq. (4.10) -(4.12), the state function of RO desalination can be described. The output value, recovery rate *R*, outside flow Q_{out}, and the specific energy consumption SEC can be defined as:

$$\mathrm{Q_{out}} = \mathrm{W_c} \int_0^{\mathrm{L}} \mathrm{J(z)dz} \tag{4.13}$$

$$\mathrm{R} \equiv \frac{\mathrm{Q_{out}}}{\mathrm{Q_{in}}} = \Phi(\mathrm{L}) \tag{4.14}$$

$$\mathrm{SEC}_f = \frac{1}{\eta} \cdot \frac{\mathrm{P_{in}} - \xi(1-\mathrm{R})(\mathrm{P_{in}} - \mathrm{P_{lost}})}{\mathrm{R}} \tag{4.15}$$

where ξ is the efficiency of the pressure recovery process and is taken to equal 97%, P_{lost} is a numerical function of P_{in}[153].

Here, the $\mathrm{SEC_f}$ is defined as the function of the feed side pressure P_{in} for a given feed salinity π_f. The feed side pressure P_{in} can also be derived from the water permeability A_m based on Eq. (4.8). Therefore, the SEC is a function of the water permeability *Am* for a given feed salinity π_f. For example, the water permeability A_m of the gradient nanocomposite membrane is 21.34 L h^{-1} m^{-2} bar^{-1}, and the feed side salinity is 2,000 ppm NaCl solution. According to Eq. (4.8), as *k(z)* and Am is known, the water flux *J(z)* is the function of P(z) and $C_b(z)$. Combining the results of Eq. (4.8) and Eq. (4.10) -(4.12), P_{in} and P_{lost} can be calculated based on the position of the vessel *z* as well as the corresponding water flux *J(z)*.

4.3 Results and Discussion

4.3.1 Gradient structure design

A nanocomposite membrane consisting of an ultrathin GO film and two MCE films is illustrated in Figure 4.3.1. The 1-nm channels in the GO membrane were tuned by the GO interlayer bonding and two porous layers with a pore size of 2-50 nm serving as the support and protective layer for RO desalination.

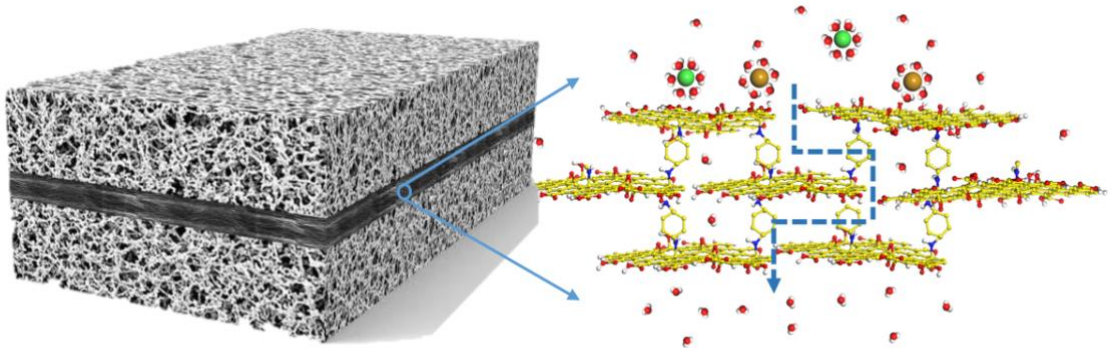

Figure 4.3. 1 Schematic of gradient structure consisting of GO laminates with 1nm channels and two symmetric mesoporous (2-50 nm pore size) layers. The ion is sieved via the middle layer, 1nm-channels GO laminates.

The gradient nanocomposite shows both gradient aperture size and gradient thickness. The mesoporous layer was made of MCE and was used to protect the ultrathin GO laminates from damage caused by sizeable hydrodynamic pressure due to water flow. The middle GO laminates serve as the essential ion sieving layer through a 1nm-channel of inter-GO spacing, and the primary energy consumption occurs at this layer. 1nm channels in the middle layer ensure high salt-rejection while the ultrathin thickness of the

1nm-channel layer ensures high water-flux and low energy consumption. High water permeability requires large pores, while high selectivity requires ultra-small pores, typically ~1nm pore size. The gradient structure can entirely solve this conflict by implementing ion sieving in the middle layer, which primarily contributes to energy consumption. Minimizing the ion sieving paths can minimize ion sieving energy consumption and also increase water permeability. A straightforward strategy is to reduce the thickness of the GO laminates since vertically aligned GO nanosheets are challenging to be scaled-up. Meanwhile, minimizing the GO laminate thickness could significantly weaken its mechanical strength, resulting in low robustness and a very short lifetime. Therefore, the conflicts between low energy consumption and a long lifetime should be solved. During the RO desalination, the tensile stress applied to the RO membrane comes from the friction between the fluid and solid membrane and the hydraulic pressure difference between the feed-side flow and permeate-side flow. The membrane should be robust enough to avoid any rupture to maintain the long-term stability of desalination performance. To ensure outstanding performance of ultrathin GO laminate, one of the most feasible strategies is to add a protective layer. Since it is difficult to directly measure the stress experienced by the membrane during the desalination process, a numerical simulation was performed by COMSOL Multiphysics to investigate the role of the protective layer on stress reduction and guide the design.

In order to determine the tensile strength of GO laminates to indicate the simulation process, the mechanical properties of GO films were measured by the dynamic mechanical analyzer (Q850, TA instruments). The samples were gripped by a film tension

clamp under ambient conditions. The tensile test was performed in controlled strain mode with a ramp rate of 0.005 mm/min and a preload of 0.01 N. Samples were cut into a rectangular shape with a dimension approximately 6 mm (width) ×25 mm (length) measured using standard calipers. The span between clamps was obtained directly from the DMA instrument, and the sample thickness was measured by AFM scanning of the fractured edge. Tensile test results (shown in Figure 4.3.2) revealed that the GO laminates have high tensile strength and modulus. The strain-stress curves of the GO laminates exhibit similar patterns as reported graphene oxide paper, which has a "straightening region" followed by a "linear region"[154]. The Young's modulus of the GO film was determined by fitting the strain-stress curve of the "linear region" (values within 0.1% strain before fracture) with a straight line. The highest tensile strength 184.1 MPa was obtained from the GO laminates with the GO nanosheet lateral size of 1430 nm. In contrast, the highest Young's modulus of the GO film 57.1 GPa was obtained from the GO laminates with GO nanosheet lateral size of 276 nm.

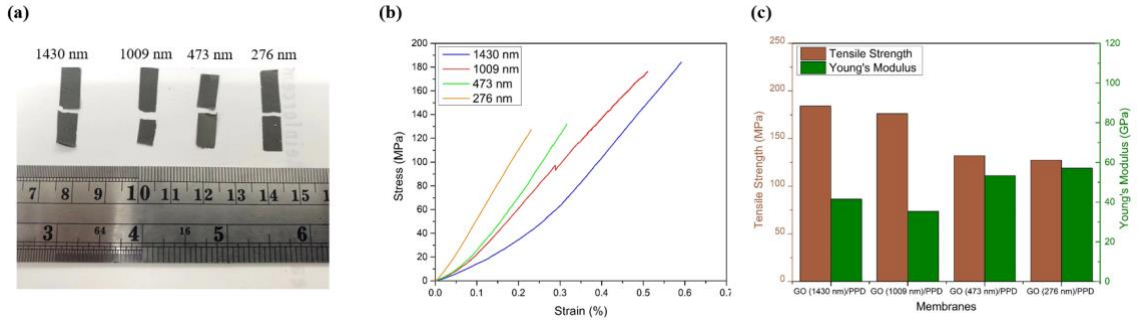

Figure 4.3. 2 Tensile strength and Young's Modulus. (a) Photograph of GO laminates after tensile test. (b) Stress-strain curve of GO laminates with different lateral sizes of GO nanosheets (1430 nm, 1009 nm, 473 nm, and 276 nm, respectively). (c) calculated tensile strength and Young's Modulus based on the stress-strain curve with different lateral sizes of GO nanosheets (1430 nm, 1009 nm, 473 nm, and 276 nm, respectively).

For the thickness of the protective layer, the geometric model of the GO laminates layer was defined as a rectangle with a height of 30 nm and a width of 2000 nm. With the same width as the GO laminates, the protective layer was designed with different thickness from 0 nm to 100 μm. The porosity of the protective layer was set to 72% according to the experimental characterization of such MCE membrane*[155]*. The input pressure, density, and dynamic viscosity of seawater were set to 1 MPa, 1.03×10^{3} kg/m^{3}, and 8.9×10^{-4} Pa·s, respectively. The Young's modulus was measured by TA Instruments DMA 850 with accessories. Fig. 4.3.3 (a) presents the maximum tensile stress acting on GO laminates and the corresponding water flux for different MCE membrane thicknesses with the same GO laminates. The maximum tensile stress working on GO laminates, which occurs on the corner, is exponentially decreasing from 2250 MPa to 0.037 MPa as the protective layer thickness increases from 0 nm to 100 μm.

The simulation cell for the aperture selection of the protective membrane was based on a 3D model. The thickness of the GO laminates was also 30 nm. The aperture was assumed as a regular circle with different diameters ranged from 10 nm to 200 nm. The distance between the apertures was determined by the porosity of the protective layer, which was set to 72%. Other parameters were appointed as the same as the previous simulation. Fig. 4.3.2 (b) shows the maximum stress acting on the ultrathin GO laminates and corresponding water flux with different aperture sizes. The largest stress occurs at the edge of the 200 nm aperture which is 268 MPa. The tensile stress in the middle of GO

laminates can also achieve 100 MPa. The water flux is also calculated by the Hagen Poiseuille (HP) Equation*[156]*.

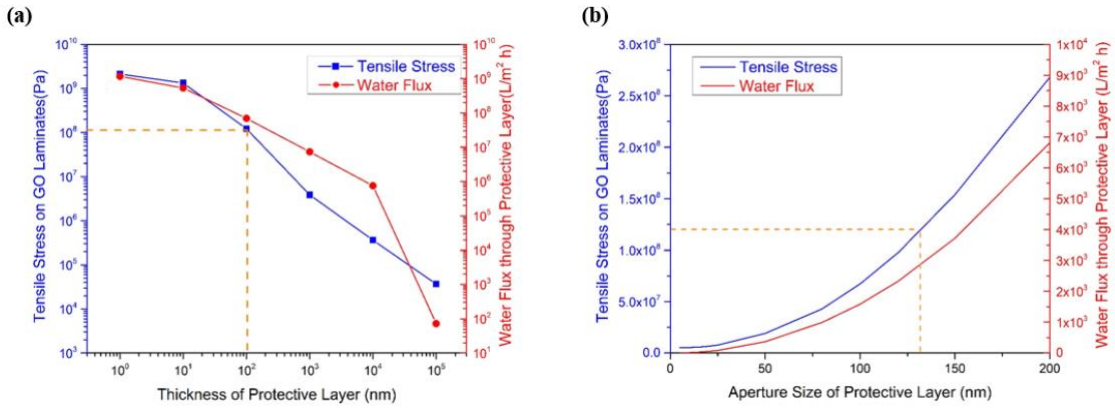

Figure 4.3. 3 Numerical illustrating the design of gradient structure. (a) The maximum tensile stress acting on the GO laminates and corresponding water flux with the different thickness of the protective layer (0, 10 nm, 100 nm, 1 µm, 10 µm, and 100 µm). (b) The maximum tensile stress acting on the GO laminates and corresponding water flux with different aperture sizes of the protective layer ranged from 10 nm to 200 nm. The dashed line indicates the tensile stress tolerance of the GO laminates, which determines the aperture size selection of the protective layer.

Generally, increasing the protective layer thickness can reduce the tensile stress applied to the GO laminates. To understand the effect of MCE layer thickness on the GO laminate robustness, a physical model was built for fixed pore size. Considering a typical operating pressure was above 10 bar (=1 MPa), the feed flow of 1 MPa was assumed for the simulation. For the MCE membranes with 25 nm pores and 72% porosity (based on experimental characterization of such an MCE membrane), the resultant hydrodynamic stress loaded on 30nm-thick GO laminates was simulated as shown in Fig. 4.3.4 (a). In this figure, the pressure distribution of the cross-sectional view of the membrane was shown by different color labels for different MCE thicknesses. The maximum tensile stress loaded on the 30-nm-thick GO laminates without the protective layer was 2,250

MPa, which could significantly damage the GO laminates. As the thickness of the MCE layer increased from h = 0 nm to h = 1000 nm, the maximum tensile stress decreased exponentially to 3.92 MPa, a much smaller value than the threshold where the GO laminates can be damaged. Therefore, the MCE layer thickness would significantly influence the hydrodynamic stress loaded on the GO laminates. This phenomenon could be ascribed to the protective layer that can bind the boundary of the GO laminates to reduce deformation area. The smaller deformation of GO laminates indicates smaller tensile stress. According to the tensile test of ultrathin GO laminates, shown in Fig. 4.3.2, the resultant GO laminates showed a tensile strength of ~120 MPa. In this case, the MCE thickness should be > 100 nm for long-time stability. On the other hand, the water flux of a commercialized MCE membrane with 100-μm thickness was still as high as 72 L/m^2 h, according to the simulation results in Fig. 4.3.3. The bottleneck for a high-water permeability was still the GO laminates instead of the MCE membrane.

Besides the thickness of the protective layer, the aperture size is another variable that affects the hydrodynamic stress, which may lead to the failure of GO laminates. Like the thickness issue, a small aperture could reduce the hydrodynamic force and downsize the water flow. Fig. 4.3.4 (b) shows the hydrodynamic stress distribution on the 30-nm thick GO laminates, which have fixed boundaries on the side with different aperture sizes. In order to visually compare the differences in the tensile stress with varying sizes of aperture, the color label for Fig. 4.3.4 (b) was set to be the same. The largest stress that occurs at the edge for the 200 nm-pore MCE layer was 268 MPa. In this situation, the GO laminates will be cracked since the 30-nm GO laminate strength is <180 MPa, resulting

in a failure of the RO desalination. When a 25 nm-pore MCE layer was used, the largest stress loaded on the GO laminates was calculated to 16 MPa, almost one order of magnitude smaller than that in the case of the 200 nm-pore MCE layer. Obviously, the hydrodynamic stress loaded on the GO laminates was susceptible to the aperture size of the MCE layer. Based on the tensile test of ultrathin GO laminate, the strength depended on the GO lateral size. For < 500 nm GO nanosheets, the resultant laminates showed a tensile strength of ~120 MPa (Fig. 4.3.2). Thus the aperture size of the protective layer should be < 130 nm for robust desalination performance (rupture of the membrane could lead to very poor ion rejection). In addition, the effect of the MCE aperture size on water flux was also examined. The MCE aperture size was on the order of 10 nm, which was large enough to fit the Hagen Poiseuille (HP) Equation*[156]*. Hence, the water flux for different apertures can be calculated through HP Equation. The size of the aperture was positively related to the water flow. The water flux for a 25-nm aperture was 86 L/m^2 h, much larger than that for the GO laminates. Therefore, selecting the aperture size for the protective layer should be based on the loaded stress on GO and ensure it is less than the maximum strength of GO laminates while the water flow stays as large as possible. Since the tensile strength of GO laminates was on the order of 100 MPa according to the tensile tests (shown in Fig. 4.3.2) and the data from the reference*[157]*, a 25nm-pore MCE was used for this study.

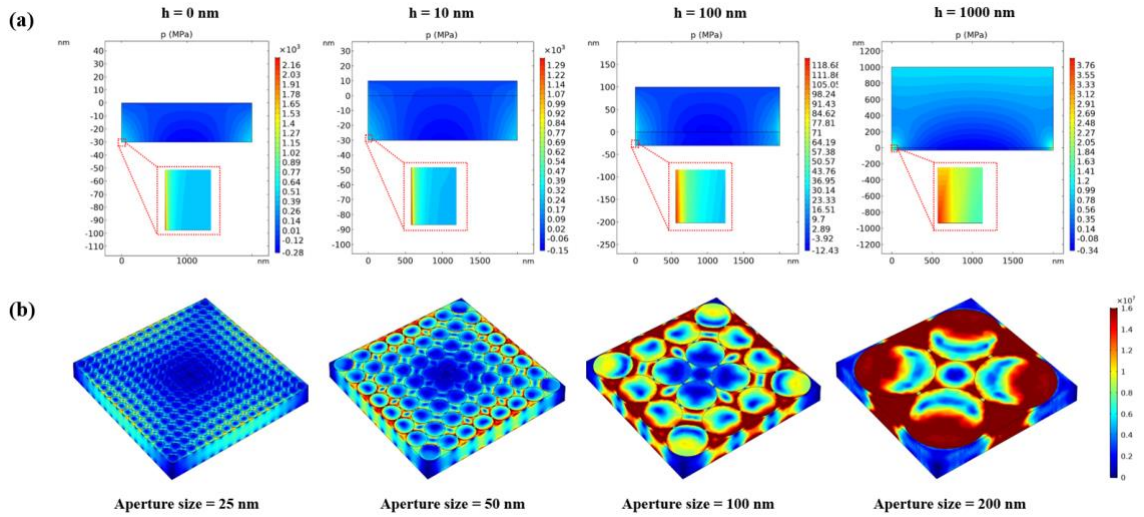

Figure 4.3. 4 Numerical simulation effects of the protective layer with different thickness and aperture sizes. (a) The cross-sectional tensile stress distribution on the GO laminates with the different thicknesses of the protective layer (h=0, 10 nm, 100 nm, and 1000 nm, respectively). (b) The tensile stress acting on the GO laminates with different aperture sizes of the protective layer (25 nm, 50 nm, 100 nm, and 200 nm, respectively).

4.3.2 Gradient GO membrane fabrication

In this research, the GO-based gradient membrane was designed to reduce the energy consumption in the RO desalination process. At the same time, the high water-permeability and high ion-rejection were maintained. A single film of GO laminates demonstrated channels around 0.7~1.1 nm caused by moistures, but it could swell and expand the interlayer spacing to 1.35 nm*[36],[31],[158]*. Cross-linking GO with desired constant interlayer spacing is essential in the RO desalination for stable performance. Compared with other cross-linkers, such as cations[36], fullerene (C_{60})[152], 1,4-phenylene diisocyanate (PDI)[41], and ethylenediamine (EDA), p-phenylenediamine (PPD) shows proper interlayer spacing as well as high robustness in water

surroundings[39]. Unlike linear diamine monomer, PPD exhibits higher stiffness because of the presence of a benzene ring, which has a fixed molecular length. The detailed route of synthesizing GO-PPD composite is shown in Fig. 4.3.5 (a) and Experiment Section.

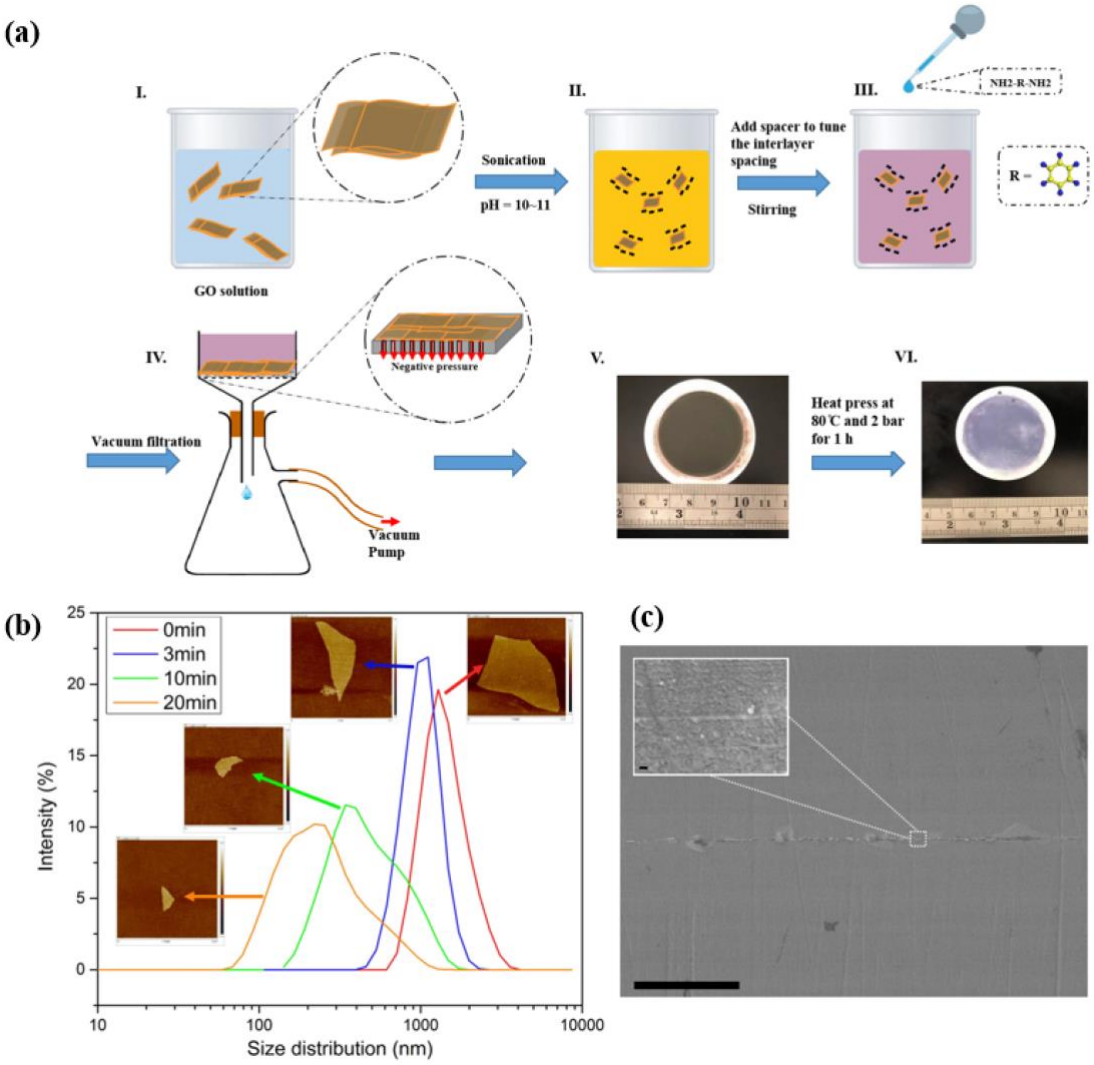

Figure 4.3. 5 Schematic of gradient GO-PPD membrane fabrication procedure and corresponding experimental characterizations. (a) The fabrication procedure of the gradient membrane. (b) DLS patterns and AFM images of GO nanosheets with different tip sonication periods (0 min, 3 min, 10 min, and 20 min which exhibit GO lateral size with 1430 nm, 1009 nm, 473 nm, and 276 nm, respectively). The width of each AFM image is 2 μm. (c) SEM image of gradient structure on cross-sectional view. The GO laminates were clamped by two MCE membranes. The scale bar for

the large image and the insert magnification image are 100 μm and 100 nm, respectively.

One feasible strategy for energy-efficient desalination is to reduce the water-transport pathway in the RO membrane since the energy losses from friction can be reduced. The water-transport pathway is determined by the thickness of the membrane and the lateral size of each GO nanosheet. To investigate the influence of GO nanosheet lateral size on the water desalination performance, GO dispersion was treated by tip sonication before further crosslinking. The average lateral dimensions of GO nanosheets with different treatment periods (0 min, 3 min, 10 m min, 20 min) were 1430 nm, 1009 nm, 473 nm, and 276 nm, respectively. DLS and the AFM characterizations are shown in Fig. 4.3.5 (b). The zeta potential of resultant solutions was also measured to understand the stability and nanomaterial distributions. At pH≈10, the zeta potential for the pure GO and GO-PDD solution was -45.2 mV and -15.7 mV, respectively. The XRD patterns and ATR-FTIR spectrums were provided in Fig. 4.3.6 and Fig. 4.3.7, respectively, to address the interlayer spacing of GO laminates and the chemical reaction between GO and PPD monomer, respectively. The average interlayer spacing of pure GO, un-crosslinked GO-PPD, and crosslinked GO-PPD was found to 0.77 nm, 1.0 nm, and 1.1 nm, respectively. The expansion of interlayer spacing was caused by the collective effect of the molecular length of the PPD monomer and the C-N bond on both sides between PPD monomers and GO nanosheets. The gradient structure was achieved by covering a filtrated untreated GO-PPD membrane (Fig. 4.3.5 (a) Step V) with another MCE membrane as the protective layer followed by hot-pressing at constant pressure and temperature to crosslink the

gradient membrane. The hydroxyl group in the cellulose acetate can react with the epoxy group on GO to create a strong chemical bond between GO laminates and the MCE membrane*[159]*. Fig. 4.3.5 (c) shows the cross-sectional SEM image of the gradient structure after crosslinking. The inset image indicates the sub-100 nm GO laminates encapsulated in the middle of the MCE membrane. The surface morphology and corresponding surface roughness are shown in Fig. 4.3.8.

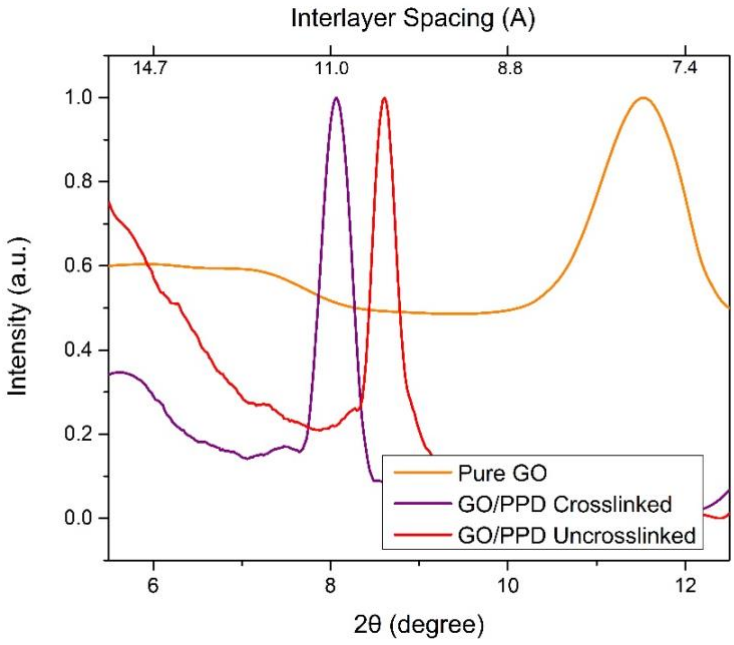

Figure 4.3. 6 XRD pattern of as-prepared pure GO (orange), uncrosslinked GO-PPD (red), and crosslinked GO-PPD (purple) membranes.

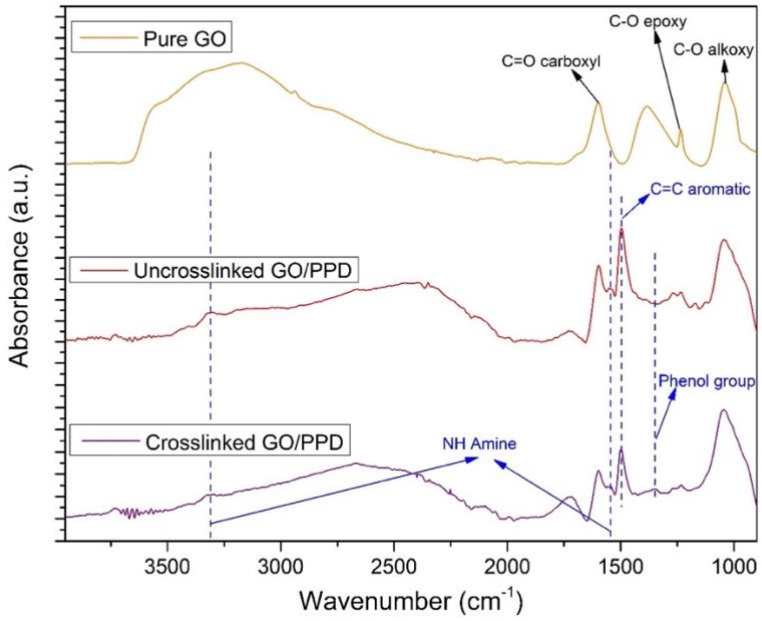

Figure 4.3. 7 ATR-FTIR spectra of pure GO (orange), uncrosslinked GO-PPD (red), and crosslinked GO-PPD (purple) membranes.

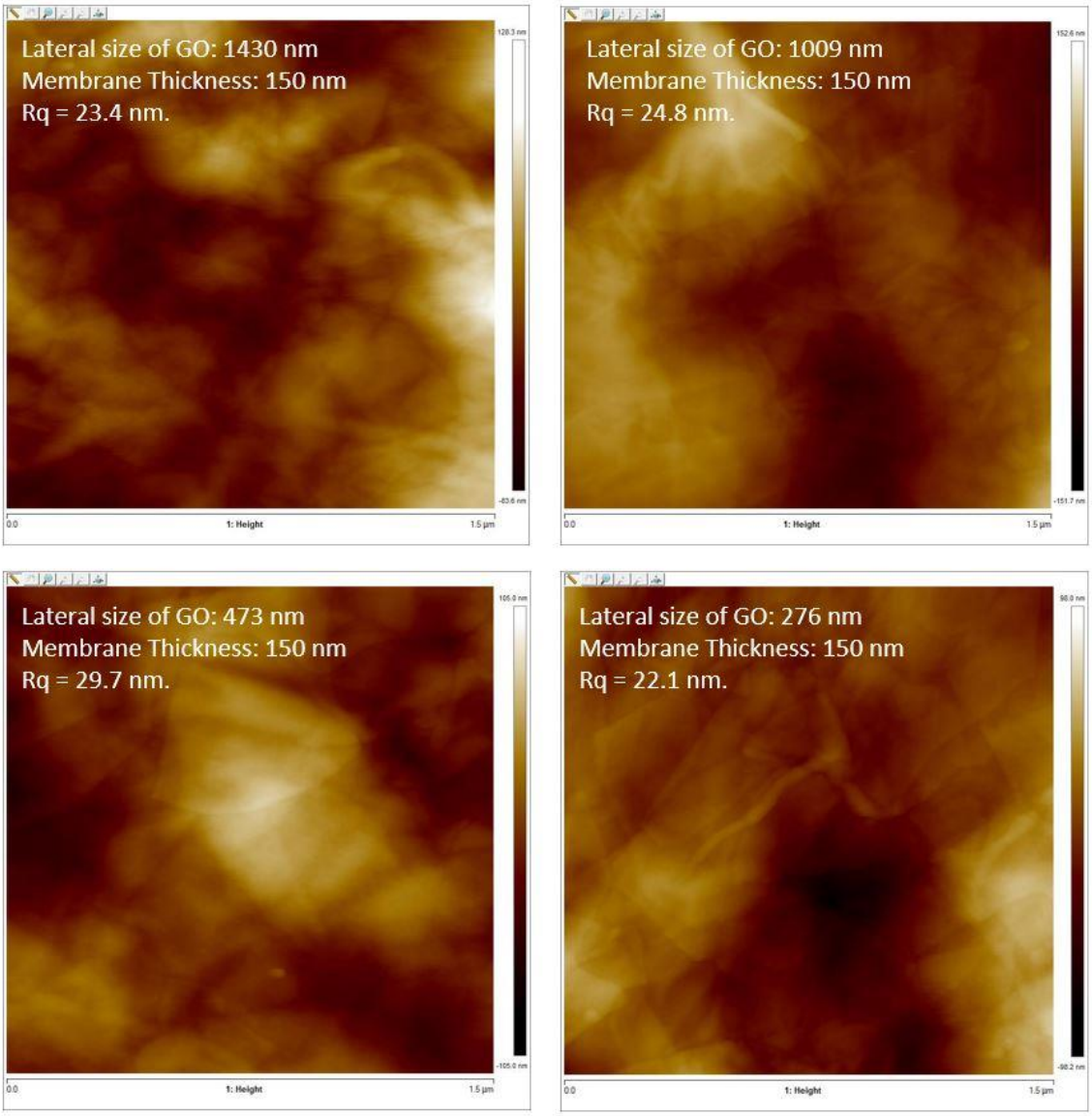

Figure 4.3. 8 GO laminates surface morphology test by AFM. The lateral size of each image is 2 µm.

4.3.3 Desalination test and scalability

To examine the effect of GO-PPD laminates thickness and the lateral size of GO nanosheets on water permeability and ion rejection rate, the desalination tests were carried

out using the nanocomposite membrane made from GO laminates with different thicknesses (30 nm, 60 nm, 90 nm, and 150 nm on average), and different GO nanosheet sizes (1430 nm, 1009 nm, 473 nm, and 276 nm). The 2000 ppm (0.034 M) NaCl water was used as the feed water, and the applied pressure was 2.68 bar, which means 1 bar left after overcoming osmotic pressure. The desalination results are shown in Fig. 4.3.9 (a) and (b), while the inserted image shows the test setup. The whole device was operating under magnetic stirring to avoid the concentration polarization effect on the feed side. The thinner GO-PPD laminates exhibited higher water permeability because of the shorter water-transport pathway, which reduced the friction during the water molecule. The ion rejection rate slightly went up for the increased thickness of the GO laminate because thicker GO-PPD laminates induced a larger steric effect to reject the salt ion. On the other hand, the enhancement of water permeability using smaller GO nanosheets can also be ascribed to reducing the water-transport pathway. As shown in the insert image of Fig. 4.3.9 (a), the smaller lateral size of GO nanosheets provides a shorter and less tortuous water-transport pathway, indicating smaller friction losses during the molecule transportation. The effect of GO lateral size on the ion rejection was negligible. Consequently, the gradient nanocomposite membrane made from the 30 nm-thick GO-PPD laminates with 476nm GO nanosheets demonstrated a water permeability of 21.34 L h^{-1} m^{-2} bar^{-1} and an ion rejection rate of 96.08%.

The effect of applied pressure on the water flux is critical for the water desalination process. When pure water passes through the RO membrane, the water flux increases linearly with the applied pressure. For the salinity filtration, the salt ions, which are

retained by the GO laminates, can form a thin layer of concentration polarization or even a cake layer*[160]*. Both these effects could boost the resistance of the membrane to water flux and thus cause the pressure to drop across the membrane. As such a layer was getting thicker, the driven pressure for the filtration process was becoming smaller due to the increasing flow resistance. When the driven pressure became smaller than the local osmotic pressure, the water molecules cannot pass through the membrane. The experimental results are shown in Fig. 4.3.9 (c) for two different lateral sizes of GO nanosheets. The dashed lines show the trends without the polarization issue. The smaller lateral size of GO nanosheets (473 nm) was usually related to a smaller polarization effect because a smaller water flux only took fewer salt ions to the surface of GO laminates. As a result, a more immense applied pressure was needed for a stable water flux. According to previous studies, the saved energy was very marginal after the permeability is over 25 L h^{-1} m^{-2} bar^{-1}, where energy consumption was already intensive*[161]*. Since energy consumption is positively related to the applied pressure, it is vital to operate the desalination process at the low applied pressure range where the polarization issue does not significantly reduce the water permeability.

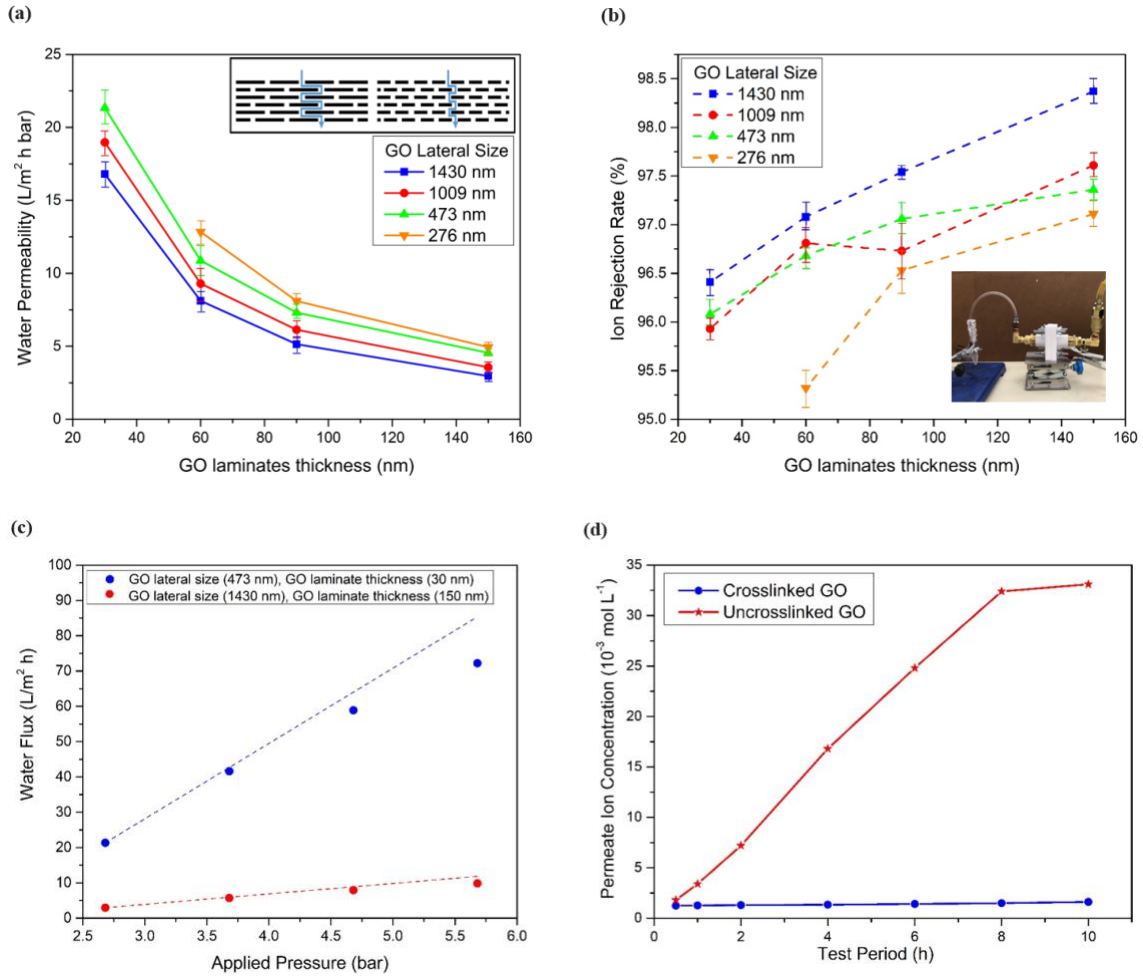

Figure 4.3. 9 Desalination performance of gradient GO membrane. (a) The water permeance for different thicknesses of GO membrane and different lateral sizes of GO sheets. The inserted image shows the water-transport pathway through the GO laminates. (b) The ion rejection rate for different thickness of GO membrane and different lateral size of GO sheets. The inserted image shows the test setup. (c) The water flux for different applied pressure. The dashed line indicates the linear trend line without the concentration polarization issue. (d) The ion concentration on the permeation side through gradient membrane for different periods (the red and blue lines indicate the uncrosslinked GO laminates and crosslinked GO laminates, respectively).

The ion rejection rate stability and membrane lifetime are also essential factors to evaluate the potential of commercialization. Resilience relies on two aspects of the

membrane, the stability of interlayer spacing and the robustness of the membrane. A stable interlayer spacing and a robust membrane can provide a long-term ion sieving effect. Most reported GO-based membranes could be effectively used for ion sieving for 5 to 10 hours*[36]*. Here, the stability of the gradient nanocomposite membrane was also tested. For comparison, the crosslinked GO laminates and uncrosslinked GO laminates were integrated into a gradient structure with a protective and supporting layer. As shown in Fig. 4.3.9 (d), for the uncrosslinked GO, the ion concentration of the permeate side increased rapidly from the beginning to 8 h until the concentration was almost equal to the feed side. This issue was caused by the swelling effect of GO laminates in the water surroundings, which enlarged the interlayer spacing of GO laminates to allow salt ions to pass through. In contrast, the ion concentration of the permeate side for the crosslinked gradient GO membrane demonstrates a negligible increase, indicating excellent stability and lifetime. In the crosslinked GO laminates, covalent bonds between GO and PPD molecule were much stronger than the hydrogen bonds between pure uncrosslinked GO, thus providing stable interlayer spacing for long-term stability.

According to the hydrodynamic theory, the filtration energy consumption SEC can be derived, and the details were provided in the Experiment Section:

$$\mathrm{SEC}_f = \frac{1}{\eta} \cdot \frac{\mathrm{P_{in}} - \xi(1-\mathrm{R})(\mathrm{P_{in}} - \mathrm{P_{lost}})}{\mathrm{R}} \tag{4.15}$$

where ξ was the efficiency of the pressure recovery process, R was the recovery rate, and P_{lost} was a numerical function of P_{in}[153].

For a given feed salinity, the feed pressure P_{in} can also be derived from the water permeability. Therefore, assuming the energy consumed by water intake, pretreatment,

product water delivery, pump & ERD inefficiency, the energy consumed by membrane filtration for RO membranes can be estimated based on the water permeability, the applied force, and the salinity concentration*[153]*. The energy consumption was a function of the applied pressure, the pressure loss in the flow resistance, and water flux. For example, the water permeability of the gradient nanocomposite membrane was 21.34 L h^{-1} m^{-2} bar^{-1}, and the feed salinity was 2,000 ppm NaCl solution. According to Eq. (4.8) - (4.15), the SEC for the gradient nanocomposite membrane was calculated to 0.169 kWh/m^3. Following the same procedure, the numerical relationship between the water permeability and the corresponding SEC for the given feed salinity was plotted as shown in Fig. 4.3.10 (a). The blue line and the green line indicated the SEC for 35,000 ppm seawater and 2,000 ppm brackish water. Considering the constant energy consumption of the RO desalination process induced by water intake, pretreatment, product water delivery, and other facilities, the overall energy consumption is shown in Fig. 4.3.10 (a).

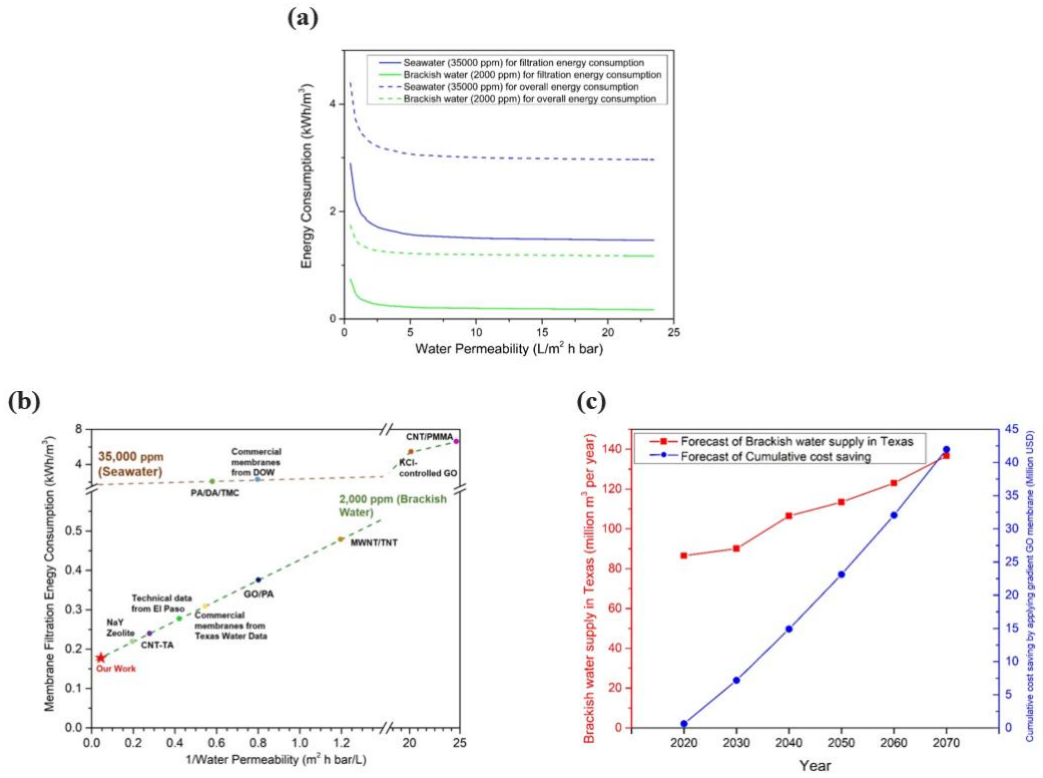

Figure 4.3. 10 (a) Filtration energy consumption and overall energy consumption of RO desalination for brackish water and seawater. (b) Comparison of the energy consumption between this work and the state-of-the-art RO desalination membranes including commercial membranes[144] and PA/DA/TMC[162] for 35,000 ppm seawater and commercial membranes[163], CNT-TA membranes[117], NaY Zeolite membranes[164], MWNT/TNT membranes[142], KCl-controlled GO membranes[36], CNT/PMMA membranes[116], GO/PA membranes[165], and technical data from El Paso Water Utilities for 2,000 ppm brackish water. (c) The forecast of future brackish water supply and corresponding cumulative cost saving by applying the gradient GO membranes.

Besides, Fig. 4.3.10 (b) also shows the comparison of the membrane filtration energy consumption between this work and the state-of-the-art RO desalination membranes, including commercial membranes[144] and PA/DA/TMC[162] for 35,000 ppm seawater and commercial membranes[163], CNT-TA membranes[117], NaY Zeolite membranes[164], MWNT/TNT membranes[142], KCl-controlled GO membranes[36],

CNT/PMMA membranes[116], GO/PA membranes[165], and technical data from El Paso Water Utilities for 2,000 ppm brackish water). Only the state-of-the-art RO membranes whose ion rejection rate larger than 90% for NaCl salinity was taken into account. The membrane filtration energy of the gradient nanocomposite membrane was 0.169 kWh/m^3, which was 35.8% less than that of commercial membranes for 2,000 ppm brackish water. As the forecast by Texas Water Development Board[166], the usage of brackish water desalination would be 90 million m^3 in 2030 and 140 million m^3 in 2070. Assuming the energy consumption accounts for 60% of the total cost[10], the cumulated cost saving from the gradient nanocomposite membranes until 2030 can reach 7.2 million for Texas. The forecast of brackish water supply and corresponding cumulative cost saving by applying gradient GO membranes is shown in Fig. 4.3.10 (c).

The scalability of the nanocomposite membranes was also examined because scalability is a crucial factor in evaluating the commercial potential of a scientific and engineering design. In contrast, many membranes like aquaporin*[150, 167, 168]* and nanoporous graphene*[23, 157, 169]* achieved high water permeability desalination membranes, but their scalability was very poor*[170]*. Fig. 4.3.11 (a) shows the as-prepared scale-up gradient nanocomposite membrane with a 30-cm diameter. Instead of vacuum filtration, the pressure-driven filtration method was applied to the scale-up fabrication of gradient nanocomposite membrane. A scale-up membrane was readily demonstrated where GO laminates were 432 nm thick on average. The only issue with scale-up lies in the lower-bound of GO laminate thickness in the large-scale nanocomposite membranes in order to fabricate the uniform and non-defect GO membrane on a large scale. It was a

little higher than that in the small-scale nanocomposite membranes. The water desalination performance was tested under the same condition as the small-size nanocomposite membranes. The water permeability was found to 0.81 L h^{-1} m^{-2} bar^{-1} while the ion rejection rate was still as high as 97.36%. Compared with the small-size gradient nanocomposite membrane, the scale-up membrane demonstrated a lower water permeability because of an increased lower bound of GO laminates thickness. On the other hand, as shown in Fig. 4.3.11 (b), the ion concentration of the permeate side for the scale-up gradient nanocomposite membrane confirmed excellent stability and lifetime. Further research is needed to tailor the thinner and uniform GO laminates at a large scale for larger water permeability and commercialization.

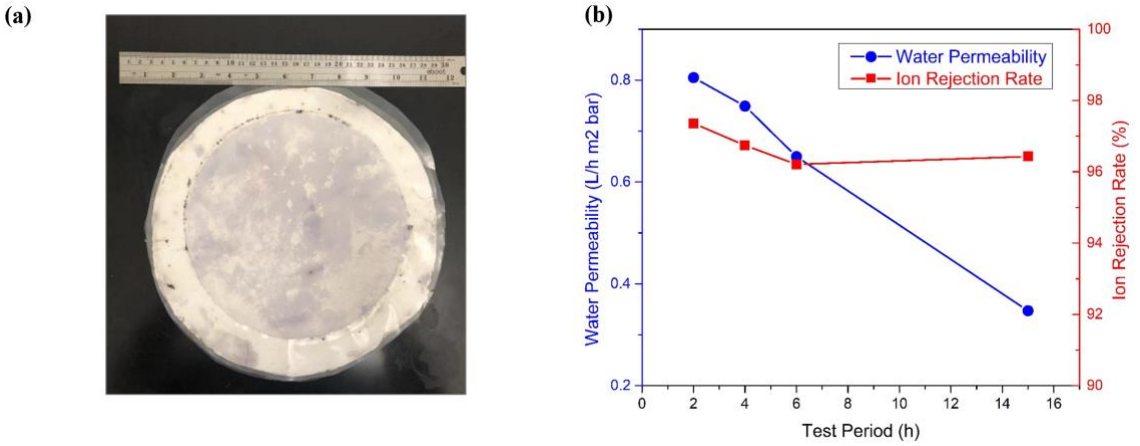

Figure 4.3. 11 Scale-up demonstrations of gradient nanocomposite membrane. (a) As-prepared scale-up gradient nanocomposite membrane. (b) The ion concentration on the permeation side through gradient membrane and ion rejection rate at different periods for scale-up gradient GO membranes (the red and blue lines indicate the permeate ion concentration and the ion rejection rate, respectively).

4.4 Summary

In summary, a gradient nanocomposite membrane has been demonstrated through simulation-guided design. The simulation results suggested that the protective layer should be >100nm thick with <130nm pores at a porosity of 72%. As-fabricated nanocomposites membranes exhibit water permeance as high as 21.34 L h^{-1} m^{-2} bar^{-1} and ion rejection rate > 96.08%, indicating a 35.8% energy saving on membrane filtration for brackish water, and the cumulative cost savings for Texas was estimated to 7.2 million in 2030 by applying the gradient nanocomposite membranes for brackish water RO desalination. The unique gradient structure supplies optimal protection for the ultrathin GO laminates, contributing to the high water-permeability and, consequently, low energy consumption and the effective reduction for tensile stress to extend the membrane lifetime. These results afford a new direction to design and fabricate scalable RO membrane for energy-efficient water desalination.

CHAPTER V

ENVIRONMENTALLY-ADAPTIVE MEMBRANE FOR RADIATIVE COOLING AND HEATING

5.1 Introduction

With the increasing concerns of global sustainability, it is vital to harvest clean energy and reduce traditional energy consumption. The heating, ventilation, and air conditioning (HVAC) systems have been extensively installed and utilized in the buildings, vehicles, aircraft, ships, and many other working and living spaces, and thus play a significant role in our daily life and work. With the climate changes and increasing demands of HVAC systems, tremendous energy is consumed to keep conformable conditions. For example, the electricity used by the residential end sector was about 1,400 billion kW in the United States in 2019. The space heating and cooling account for 26% of that and approximately 44 billion USD per year.[11] Considering the rapid population growth and the climate change due to the global greenhouse gas emission, the space heating and cooling energy consumption for buildings is expected to grow by 79% and 83% throughout 2010-2050, respectively.[12] Such massive energy consumption could lead to a significant greenhouse gas emission since most of the energy was generated by traditional fossil fuels. The emerging electric vehicles (EV) also consume electricity significantly by the HVAC system, resulting in a substantial reduction in the mileage per charge. As Idaho National Lab (INL) reported, the air conditioning and heating system

can impact the range of the EV up to 30% and 35%, respectively, depending on the ambient temperature and desired cabin temperature[171]. Therefore, HVAC systems consume a large amount of electricity and limit the performance of EVs. As a result, environmentally-adaptive cooling and heating are promising to substantially reduce the energy consumption by the HVAC while still maintaining a comfortable condition for human life and work toward energy and environmental sustainability. Passive radiative cooling through scattering incoming heat back to outer space becomes a promising strategy to reduce the energy consumption of HVAC systems. The emissivity of the surfaces of the materials has been delicately designed to suppress parasitic absorption from the surrounding thermal radiation in the atmospheric transparency window (8-13 μm) to achieve radiative cooling[54]. On the other hand, the minimum emissivity of the material surface in the atmospheric transparency window (8-13 μm) has also been designed to enhance the absorption from the surrounding thermal radiation to realize radiative heating[172]. Such a single function of radiative cooling or heating has demonstrated the great potential to reduce the energy consumption in the HVAC while maintaining the same level of comfortable conditions. Unfortunately, a single function of radiative cooling or heating is challenging to meet the demand due to the rapid change of climate. It is difficult to frequently change the installation of a single radiative cooling structure or single radiative heating structure in a concise period. For example, the diurnal temperature variations typically range from ~ 10^{o}C in humid. The tropical areas, such as Western Intermountain Plateau areas in the United States, show even higher diurnal temperature variations, as high as ~40 ^{o}C. According to the observation of land surface temperature

(LST) over the United States, the diurnal temperature range (DTR) can be as high as 25 ℃ or more in summer and 15 ℃ or more in winter over 50% of the area of the US[173]. The yearly mean DTR of the US is about 13.5 ℃[174]. The rolling changes between cold and hot temperature in a short period require an automatically switchable thermal management strategy to provide a comfortable environment in a building in order to reduce energy consumption and foster global sustainability. The rapid temperature changes between day and night not only cause a massive consumption of energy and devastate the greenhouse gas emission but also has a significant impact on human health. Extreme weather conditions (heat, cold, storms, and floods) have long been associated with increased injury and mortality. During 2006–2010, about 2,000 U.S. residents per year died from weather-related causes of death. About 31% of these deaths were attributed to exposure to excessive natural heat, heatstroke, sunstroke, and about 63% were attributed to exposure to extreme natural cold, hypothermia, or both [175]. In a more recent study, an average of 658 deaths in the U.S. is classified as directly attributable to heat-related causes annually [176]. High values of DTR are one of the inducements of stroke morbidity[177]. The large DTR in a day indicates that the environment can be either too hot or too cold for humans.

Consequently, the environmentally-adaptive sustainable strategy is urgently needed to automatically implement radiative cooling functionality in hot weather and radiative heating at cold ambient, as well as a quick switch between radiative cooling and radiative heating functions to fit different situations. By now, many artificial structures have achieved monofunctional radiative cooling, including layered structure-based

membrane[64, 67, 72, 178], microparticle filling-based membrane[48, 74], and patterned structure-based membrane[55, 77, 79, 80]. However, these technologies cannot respond to environmental changes and lack an effective mechanism to regulate heating and cooling dual-functionally. The progress for the dual-functional structure is very limited. Zhang et al.[84] designed a dynamic gating of IR radiation through the opening and closing bundle of yam, but it shows the same IR transmittance on both sides of the membrane, resulting in low efficiency of heating and cooling even though it is switchable. Hsu et al.[179] demonstrated a dual-mode device with electrostatically controlled thermal contact conductance with high cooling and heating power. However, this design is only limited to the roof of buildings since it requires a roller system to change the heating and cooling film.

In order to achieve environmentally-adaptive radiative cooling and heating toward global sustainability, the surface of materials should be “smart”. It should change its function (either radiative cooling or radiative heating) in response to the ambient temperature. It is well-known that poly(N-isopropylacrylamide) (PNIPAM) is an exceptional thermal responsive polymer and seems a perfect candidate for this application[180].

In this study, a novel responsive structure for environmentally-adaptive cooling and warming is designed and fabricated named as an environmentally-adaptive membrane (EAM), which could substantially reduce the energy consumption in the HVAC toward energy and environmental sustainability. Specifically, numerical simulations were performed to understand the influence of the geometry parameters on the cooling and

heating power. The two-photon laser lithography technology was used to fabricate the as-designed structure at the resolution of 1 μm. The radiative cooling and heating capability and adaption of as-fabricated systems were characterized.

5.2 Experiments

5.2.1 Materials

N-isopropylacrylamide (Sigma-Aldrich, >97%), N,N′-methylenebis (acrylamide) (Sigma-Aldrich, >99%), 2-hydroxy-4′-(2-hydroxyethoxy)-2-methylpropiophenone (Irgacure 2959) (Sigma-Aldrich, >98%), Rhodamine B Tetraethylrhodamine (Sigma-Aldrich, >95%), Methylene Blue 3,7-bis(Dimethylamino)phenazathionium chloride (sigma Aldrich, >82%), 3-(trimethoxysilyl)propyl methacrylate (Sigma-Aldrich, >97%), ethylene glycol (Macron Fine Chemicals, >99%), acetone (Macron Fine Chemicals, > 99.5%), isopropanol (Macron Fine Chemicals, >99.5%), IP-L 780 Resin (Nanoscribe GmbH), IP-S Resion (Nanoscribe GmbH). All chemicals and solvents were used as received without further purification.

5.2.2 NIPAM resist synthesis

10 mg Irgacure 2959 was dissolved in 500 μL ethylene glycol and 500 μL acetone mixture. Then 400 mg N-isopropylacrylamide (NIPAM) and 40 mg N, N′-methylenebis(acrylamide) (Mbis) were added to the solutions and incubated overnight.

5.2.3 Pretreatment of substrates

Since the microstructure can only be printed on the 170-μm-thick coverslips, the coverslips were successively immersed into acetone, ethanol, and DI water by sonication, each for 15 min. Then the coverslips were treated with UV-ozone for 30 min to make the surface hydrophilic. To increase the adhesion of the microstructures to the coverslips, the coverslips were treated by 3- (trimethoxysilyl)propyl methacrylate (1 mM in toluene) for one hour. After being washed with acetone and DI water, the coverslips were dried under nitrogen.

5.2.4 Fabrication of 3D microstructures

A commercial Direct Laser Writing setup (Nanoscribe Photonics GT2 high-resolution 3D printer, Nanoscribe GmbH) with 25 ×, NA = 0.8 and 63 ×, NA = 1.4 oil immersion objective was used for fabrication. To fabricate the thermal responsive structure formed by PNIPAM, as prepared NIPAM resist was drop cast onto the pretreated coverslips. Then add a drop of IPL-780 on the top of the NIPAM resist. The thermal responsive structure was achieved with a laser power at the inner focal plane of 35mW

and the outer focal plane with 40 mW, respectively. The scan speed was set constantly at 10mm/s. After writing, the structures were rinsed with acetone and subsequently transferred into tDI water for further development and storage. No post-curing treatment was applied.

5.2.5 Characterization

The optical microscope (Nikon Eclipse LV150N) was used to observe the morphology of the printed structure. To analyze the thermal response of the samples to changes in temperature, the thermoelectric Peltier plate was power by Keithley 2400, and the temperature was measured by TC-2000 with thermal couples. The 3D-structure of the samples was measured by Keyence VHX-7000. Absorbance/Emissivity characterization was carried out by the ATR-FTIR spectrometer (Bruker Alpha-Platinum), and UV-Vis-NIR spectrometer (Hitachi U-4100) for the wavelength range at 2 μm - 20 μm and 0.2 μm – 2 μm, respectively. The IR images and videos were recorded by the FLIR IR camera (48001-1001, -20°C to 350°C) with a 2X lens (T197214, IFOV 50 μm, WD = 33 mm).

5.2.6 Radiative cooling power calculation

The cooling power calculation is followed the method published by Min Gu[55] et al. Briefly, the net cooling power of the emitter can be defined as:

$$P_{net} = P_r - P_a \tag{5.1}$$

Here, P_r is the power radiated by the emitter, and P_a is the incident atmospheric radiation absorbed by the emitter.

First,

$$P_r = \int_0^{\frac{\pi}{2}} \pi \, sin2\theta d\theta \int_0^{\infty} U_B(T_s, \lambda) e_s(\lambda, \theta) \, d\lambda \tag{5.2}$$

where

$$U_B(T, \lambda) = \frac{2hc^2}{\lambda^5} \frac{1}{e^{hc/\lambda k_B T} - 1} \tag{5.3}$$

is the spectral radiance of a blackbody defined by Planck's law at temperature T where h is the Planck constant, kB is the Boltzmann constant, c is the speed of light, λ is the wavelength, and T_s is the temperature of the emitter.

The factor $e_s(\lambda, \theta)$ in Eq. (5.2) is the emissivity of the EAM, which is measured by the UV-Vis-NIR spectrometer and ATR-FTIR spectrometer according to Kirchhoff's Law.

Similarly, the absorbed incident radiation P_a can be calculated by:

$$P_a = \int_0^{\frac{\pi}{2}} \pi \, sin2\theta d\theta \int_0^{\infty} U_B(T_a, \lambda) e_s(\lambda, \theta) \, e_a(\lambda, \theta) d\lambda \tag{5.4}$$

The angle-dependent emissivity factor $e_a(\lambda, \theta)$ is given by:

$$e_a(\lambda, \theta) = 1 - t(\lambda)^{1/cos\theta} \tag{5.5}$$

where $t(\lambda)$ is the atmospheric transmittance in the zenith direction. The data of $e_a(\lambda, \theta)$ can be found from Gemini Observatory[181]. T_a is the ambient temperature, which is considered to be 300 K. The calculation can be finished by Python (Pandas).

5.2.7 Numerical simulation

The numerical simulations were carried out using the finite element (FE) method, and the finite-difference time domain (FDTD) approaches based on Maxwell's Equations and Heat Transfer Model. Since the closed-flower structure shows the extraordinary emissivity in the atmospheric window range, several dimensional factors needed to be studied. For a range of 3D designs within the membrane, the overall emissivity of the membranes will be calculated with different dimensional factors, including the height, the layer thickness, and the gap distance of linear structures. The equations were solved by Lumerical FDTD Solutions.

5.3 Results and Discussion

5.3.1 Structure design and numerical simulation

In order to achieve environmentally-adaptive radiative cooling and heating, the material structure that responses to the environmental temperature change is critical. A pyramid structure, which looks like a closed flower, has a promising selectivity of mid-infrared absorption to realize high-performance radiative cooling[55, 80]. To achieve environmentally radiative cooling and warming in a single emitter material, the emitter should be switchable between high absorptivity and low absorptivity. The closed-flower structure could effectively reflect the IR radiation and reduce the transmittance, resulting

in radiative cooling capability. In contrast, the open-flower structure cannot realize this function. The double-layered system can be designed based on this knowledge, as shown in Fig. 5.3.1 (a). When the ambient temperature is low, the membrane exhibits the heating function. The shape of the outside layer is the open-flower condition, which allows the atmospheric radiation to come through for heating the zone covered by the membrane. The inside closed-flower structure can effectively prevent the inside heat loss. When the ambient temperature is high, the membrane can realize the cooling function. The outside structures are automatically transformed to the closed-flower condition to prevent the atmospheric radiation from passing through. The inside structures change to the open-flower state, respectively, allowing the inside heat to get out in the way of IR radiation. The detailed mechanism is illustrated in Fig. 5.3.1 (b).

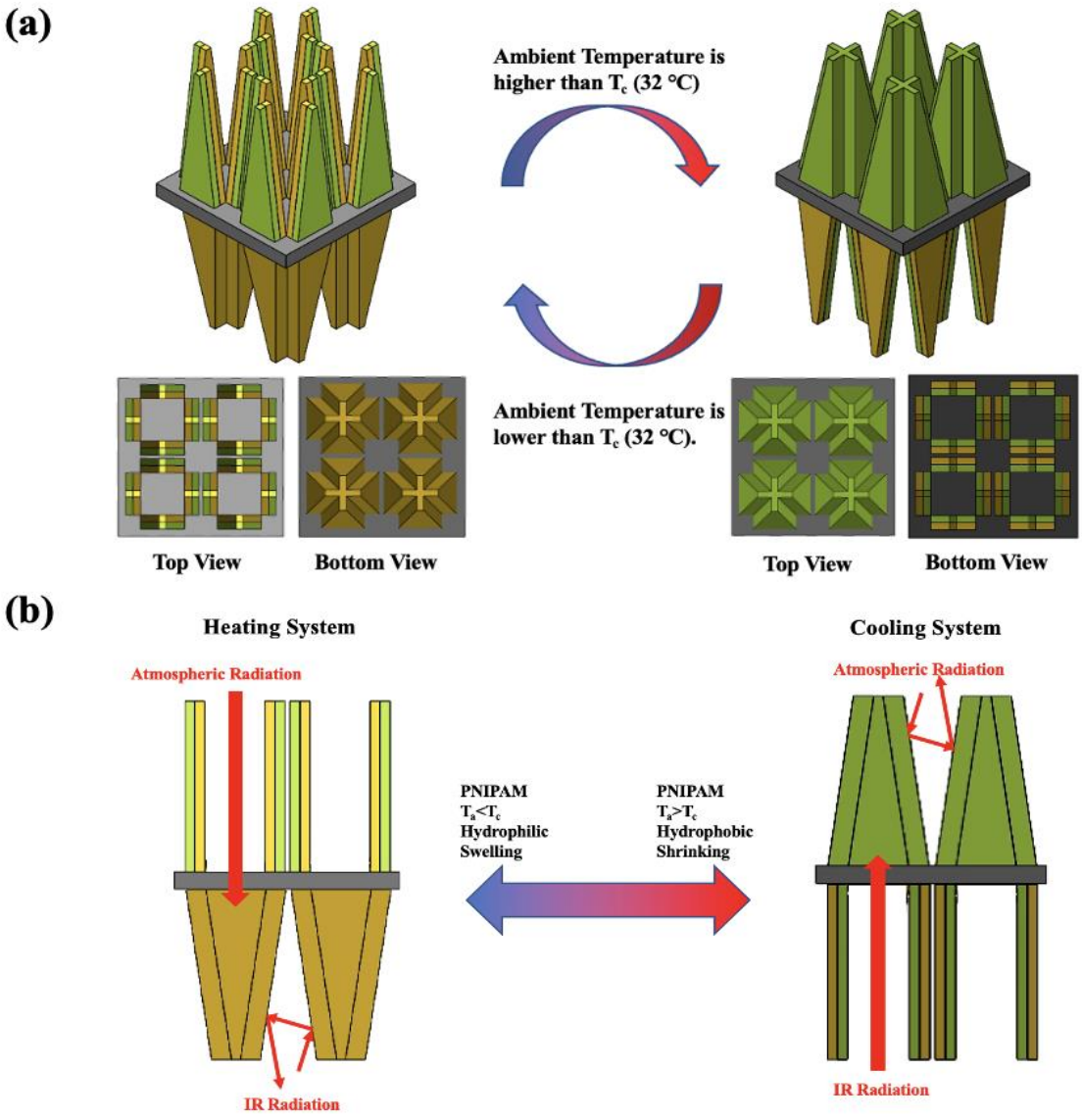

Figure 5.3. 1 Schematic of responsive structure for environmentally-adaptive cooling and warming. (a) Environmental temperature-induced structure evolution for radiative cooling and heating. (b) The mechanism of environmentally-adaptive self-cooling and heating membrane through IR radiation transmission and reflection.

As shown in Fig. 5.3.1, the closed-flower structure will allow trapping the IR radiation while the open-flower structure will let IR radiation pass through. The transformation between the closed-flower and open-flower formats will automatically

allow self-cooling and heating in response to the environment. The relationship between the structure and the corresponding emissivity on the atmospheric window and solar spectrum was investigated to guide the structure design and material selection. The critical issue for radiative cooling is reducing the absorbance from the ambient and increasing the emissivity from inside to outside. Similarly, for radiative heating, the essential factor is reducing the emissivity from the inside object. Simulation of the emissivity of different structures and resulting cooling or heating function could provide insight into the design of the responsive material structure. The numerical simulations were carried out using the finite element (FE) method and the finite-difference time-domain (FDTD) approaches based on Maxwell's Equations and Planck's Law. Since the closed-flower structure looks like a pyramid with a platform on the top, we could design a pyramid structure representing the closed-flower structure and four triangular prisms to define the open-flower structure. Since the pyramid structure shows the extraordinary emissivity in the range of the atmospheric window[80], several dimensional factors need to be studied. First of all, the vertex angle of a pyramid structure is the most significant factor, determining the reflection of electromagnetic waves amongst the pyramids. Generally, the reflection rate increases as the vertex angle decreases, and the IR radiation, as a kind of electromagnetic wave, will be reflected more and absorbed less[182]. On the other hand, as the vertex angle decreases, more pyramid structures and higher height are needed to cover a given area. Herein, we position the vertex angle of the pyramid at 15 degrees to balance the conflict between size and reflectivity[182]. Ideally, the tip of the pyramid structure is a point, but it is extremely difficult to fabricate. Usually, a platform at the top

of the pyramid is created in the fabrication process. Accordingly, the pyramid structure with a small platform, including the geometrical parameters, is designed for numerical simulation, as shown in Fig. 5.3.2 (a, b). The bottom length, top length, gap distance of the structure, and height are denoted as *a*, *b*, *c*, and *h*, respectively. All the parameters are designed for the closed-flower system. The open-flower structures are calculated according to the closed-flower structure. In the numerical simulation, the refractive index of the designed structure was assumed to 1.50 for PNIPAM based on the literature[183]. As shown in Fig. 5.3.2 (c), when the gap distance (denoted as c) is constant, the valley of the absorptivity shifts towards the atmospheric window range as the geometric parameters (*a*, *b* and *h*) increase. Specifically, when the bottom length of the pyramid structure is greater than 30 μm, the valley of the absorptivity will be located in the atmospheric window. Therefore, the optimal bottom size of the pyramid structure would be 30 μm. On the other hand, as shown in Fig. 5.3.2 (d), when the gap distance is a constant, the absorptivity decreases as the geometric parameters (*a*, *b* and *h*) increase. To optimize the absorptivity, it is better to reduce the gap distance as small as possible. However, considering the feasibility of the printing process, the gap distance should match the resolution of the 3D printer.

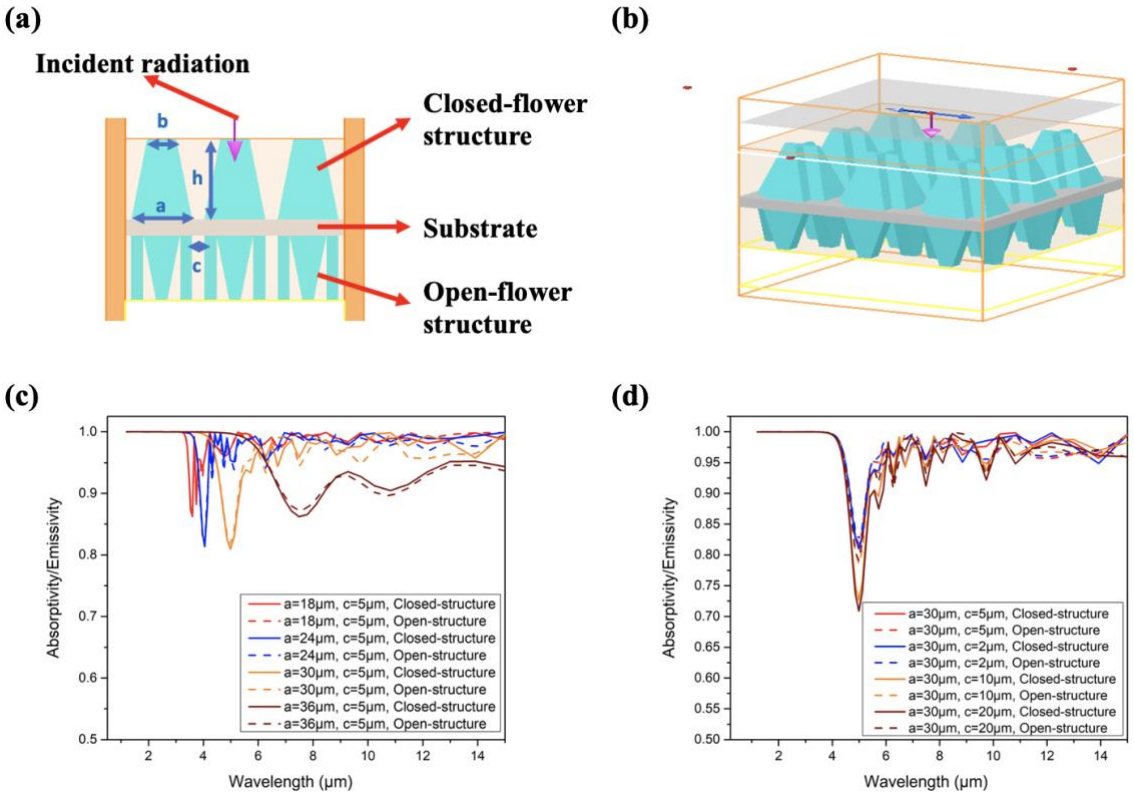

Figure 5.3. 2 Simulation of emissivity of different sizes of EAM structures. (a) Side-view of the designed system. (b) The developed model in Lumerical FDTD simulation. (c) Calculated emissivity spectra for different bottom lengths of the closed-flower structure.

5.3.2 Two-photon laser lithography of PNIPAM microstructures

The fabrication of the EAM structures has been demonstrated using the two-photon laser lithography method. To maintain the stability of the 3D design, the ratio between the monomer (here N-isopropylacrylamide (NIPAM)) and the crosslinker (here N, N′-methylenebis(acrylamide) (Mbis)) is critical. A high concentration of crosslinkers helps to construct the hydrogel but reduces the response capability to the environmental stimulus. On the contrary, it is hard to construct hydrogel using a low crosslinker

concentration while the response to the stimulus is obvious. Therefore, the balance between functionality and feasibility is an initial challenge. According to the literature[184, 185], the molar ratio of NIPAM and Mbis at 10:1 was a good trade-off. Besides the monomer and crosslinker, the photoresist also contains the photoinitiator (PI). Since the laser wavelength of the two-photon laser lithography is 780 nm, the absorption peak for the PI should be around 390 nm. Therefore, 2-Hydroxy-4′-(2-hydroxyethoxy)-2-methylpropiophenone (Irgacure 2959) was selected as the PI in the photoresist. The PI was dissolved in the ethylene glycol (EG) and acetone first to provide a sound dispersion for polymerization.

Another challenge for fabricating the PNIPAM microstructures is to adjust the printing parameters to increase the printability. Möller et al.[185] indicated that the pure NIPAM and Mbis photoresist is hard to be printed by two-photon polymerization due to the low energy delivery. Even if the scan speed was as low as 2000 μm/s and the laser power was as high as 80 mW, the printing process was still very tough, and the resolution was low. Here, one promising strategy to solve this problem is to cover the NIPAM resin with a commercialized IP-L 780 resin layer to increase power delivery[186]. These two kinds of resin are interpenetrated on a scale smaller than the wavelength of the light. By introducing this method, the NIPAM resin can be polymerized under 10,000 μm/s scan speed and 30-40 mW power, respectively. The resolution can be at 100 nm level. In the design, when the ambient temperature is higher than the critical temperature (T_c) of PNIPAM, the polymer shrinks and stiffens because of the hydrophobic property. The magnitude of this effect highly depends on the density of crosslinking during the

polymerization process. With the higher crosslinking density of the polymer chains, the structure is more confined to its designed geometry and is harder to transform. In this case, the thermal response for the highly crosslinked area is weak. To achieve shape transformation between the open-flower and closed-flower structures, each triangular prism can be divided into two layers, as shown in Fig. 5.3.1 (a). The inner layer of the triangular prism indicated in yellow (lower crosslinking density) demonstrated a stronger shrinking than the outer layer shown in green (higher crosslinking density), which led to a pronounced bending toward the closed-flower structure when the temperature is higher than the critical temperature of PNIPAM.

The crosslinking density can be controlled by the exposure dose delivered to the curing region. A larger exposure dose results in a higher crosslinking density, while the lower exposure dose indicates a lower crosslinking density. To vary the local exposure dose during the fabrication process, the gradient of laser power can realize the exposure dose slope when the scan speed is constant. This method is called gray-tone lithography, which gradually changes the material properties by continuously varying the exposure dose during the fabrication process[187]. In this method, a highly localized control of the crosslinking density can be achieved, and, consequently, the thermal responsive structure was fabricated. The detailed printing parameter is stated in the Experiment Section. Specifically, the green layers in Fig. 5.3.1 (a) were printed at 40 mW, and the yellow layers were printed at 30 mW, respectively. After that, the printed PNIPAM microstructures were transferred to acetone to remove the IP-L 780 resin, followed by DI water immersion.

After development, the samples were kept in DI water to avoid drying of the formed hydrogel.

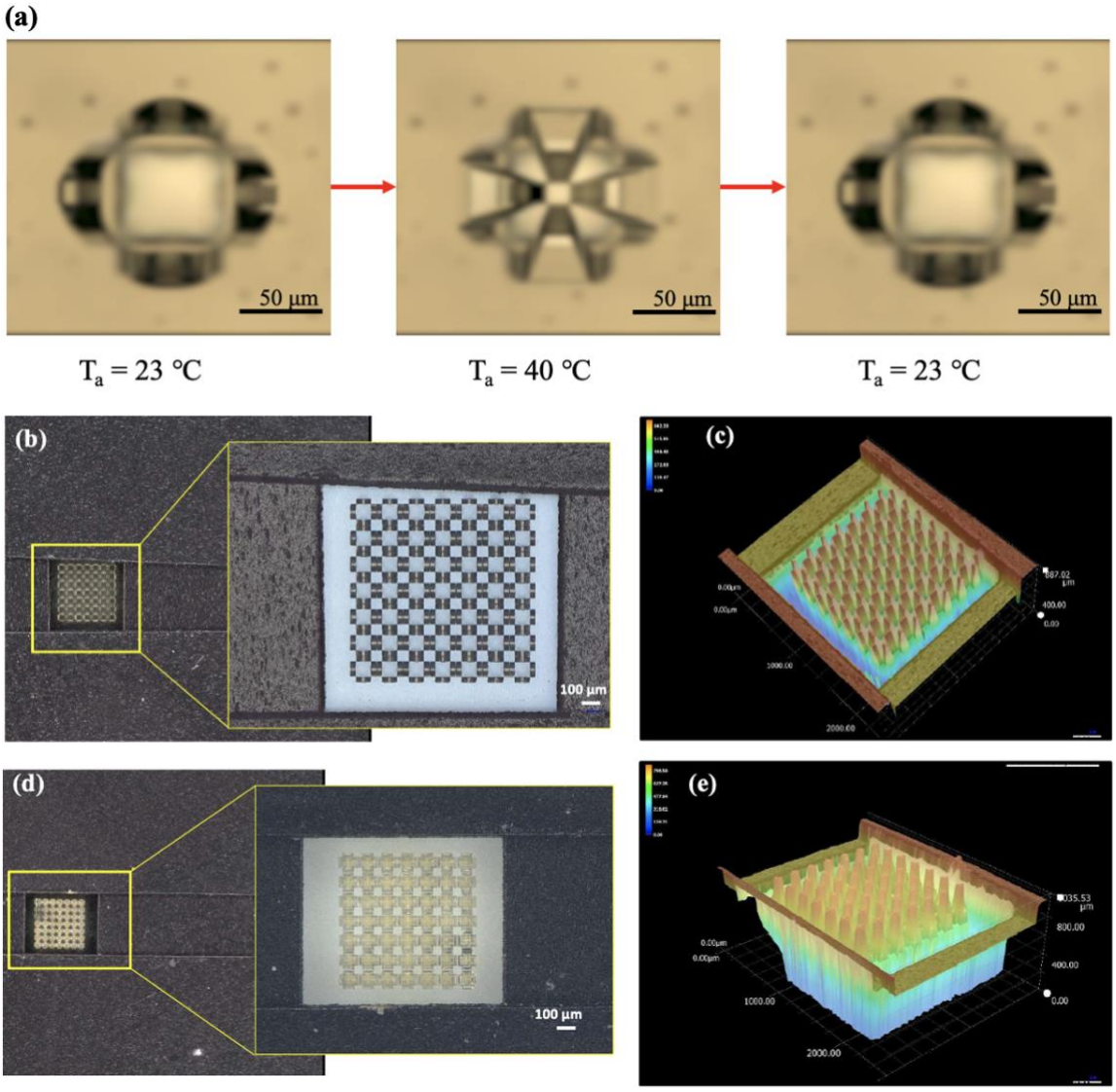

Figure 5.3. 3 Environmentally-adaptive micro-structure fabrication. (a) Temperature-induced transformation between open-flower structure and closed-flower structure. (b-c) Top view and 3D image of printed open-flower structure. (d-e) Top view and 3D image of printed closed-flower structure.

To investigate the thermal response of as-designed structure, as-printed samples were heated or cooled to the desired temperature controlled by a thermoelectric Peltier plate powered by Keithley 2400. According to the ambient temperature, the shape transformation was evaluated by the optical microscope (Fig. 5.3.3 (a)). When the ambient temperature is lower than T_c of PNIPAM (32 ℃), the as-printed structure exhibited the original printed shape, i.e., open-flower form. As the ambient temperature went higher than T_c, PNIPAM transited from hydrophilic to hydrophobic, which resulted in the shrinkage in volume. Since the crosslink density of the outer layer (green layer) is higher than that of the inner layer for each prism, the transition of outer layers is not as sharp as that of the inner layers. Therefore, the open-flower structure was bent to the closed flower structure when the ambient temperature was 40 ℃. After the ambient temperature was decreased to room temperature, PNIPAM exhibited hydrophilic property again and tended to swell in water. The closed-flower structure was re-open to the open-flower shape. This ability to change shape with temperature stimulus provides an excellent opportunity for the realization of EAM.

To experimentally verify the radiative cooling and heating performance of the designed responsive structure, we fabricated patterned structures on substrates for further measurements. Since it is very time-consuming to print deformable structures with a 63x lens (30 min for an open-flower form), we use a 25x lens to print non-deformable systems on a 1.5 mm * 1.5 mm scale to measure the emissivity of EAM. According to the numerical simulation results, the emissivity highly depends on the geometric parameter of the structure. In this case, four groups of samples for both closed-flower structure and

open-flower structure were prepared for testing. The parameters of the system are listed in Table 5.1. In this design, the bottom lengths of the structure were ranged from 30 μm to 120 μm, the thickness of each triangular prism *d* is 1/3 of the bottom size *a*, the gap distance is a constant at 5 μm, and the height of the structure was calculated based on the vertex angle of the pyramid structure. Fig. 5.3.3 (b-e) shows the printed open-flower structure and closed-flower structure when a = 90 μm. Other printed samples for both open-flower and closed-flower shapes were collected in the Fig. 5.3.4 (a-h).

Table 5. 1 Geometric parameters of the printed structure

Sample #	a (μm)	d (μm)	c (μm)	h (μm)	a/c
1	120	40	5	425	24
2	90	30	5	311	18
3	60	20	5	197	12
4	30	10	5	83	6

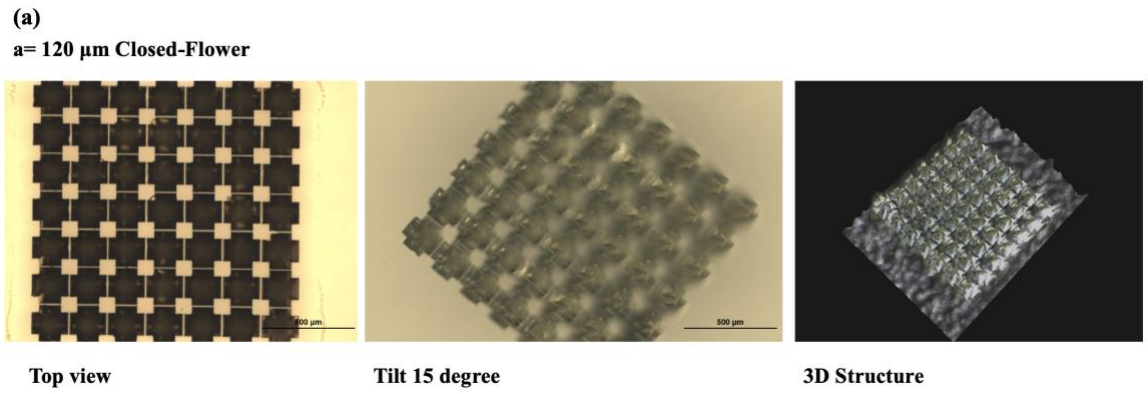

(b)

a= 120 µm Open-Flower

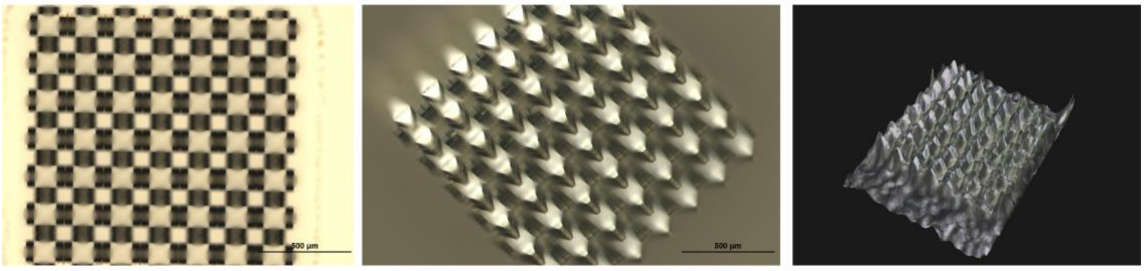

Top view **Tilt 15 degree** **3D Structure**

(c)

a= 90 µm Closed-Flower

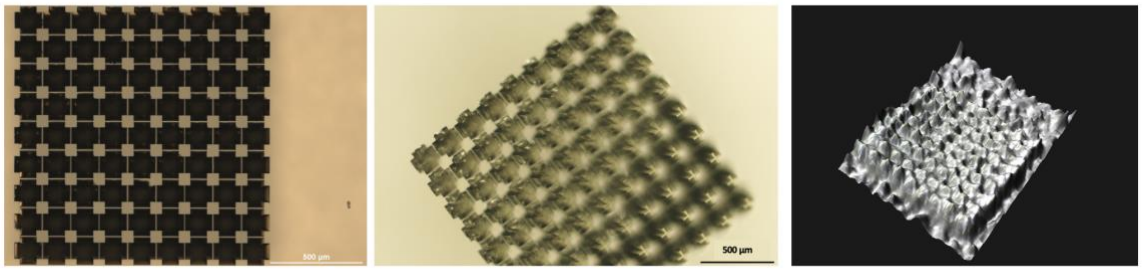

Top view **Tilt 15 degree** **3D Structure**

(d)

a= 90 µm Open-Flower

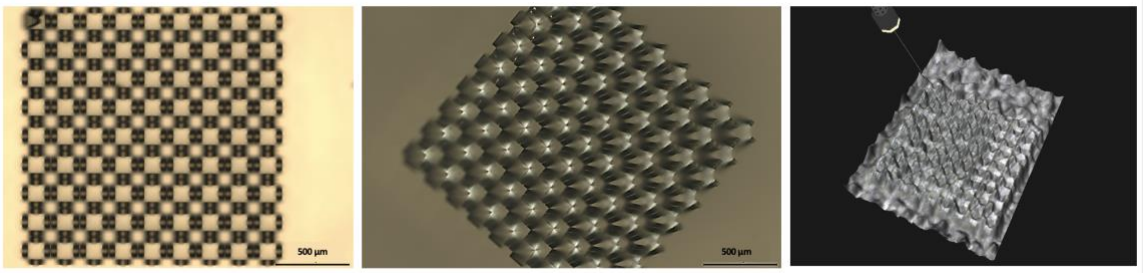

Top view **Tilt 15 degree** **3D Structure**

(e)

a= 60 µm Closed-Flower

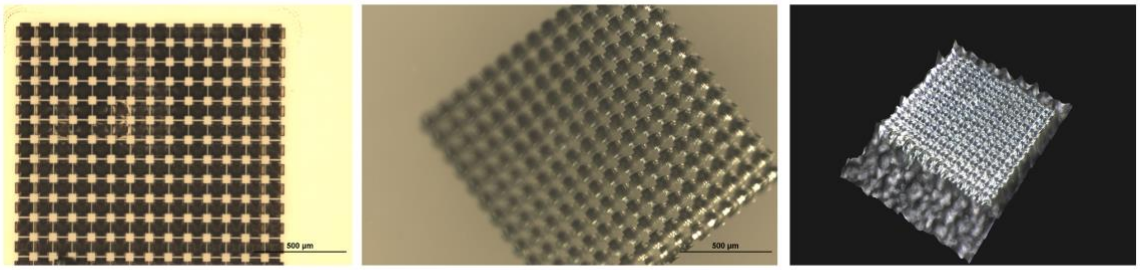

Top view **Tilt 15 degree** **3D Structure**

(f)

a= 60 µm Open-Flower

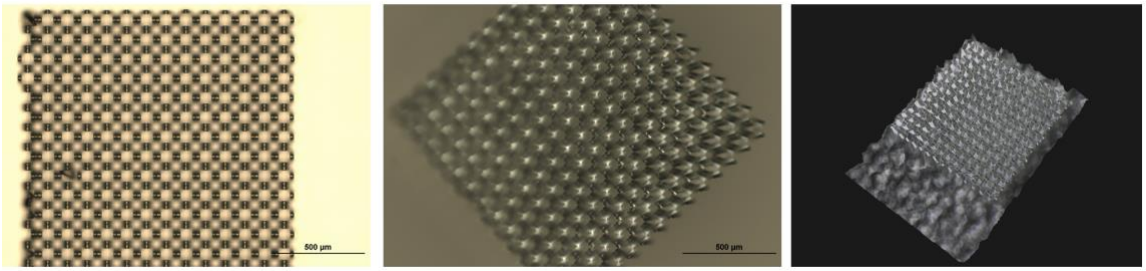

Top view **Tilt 15 degree** **3D Structure**

(g)

a= 30 µm Closed-Flower

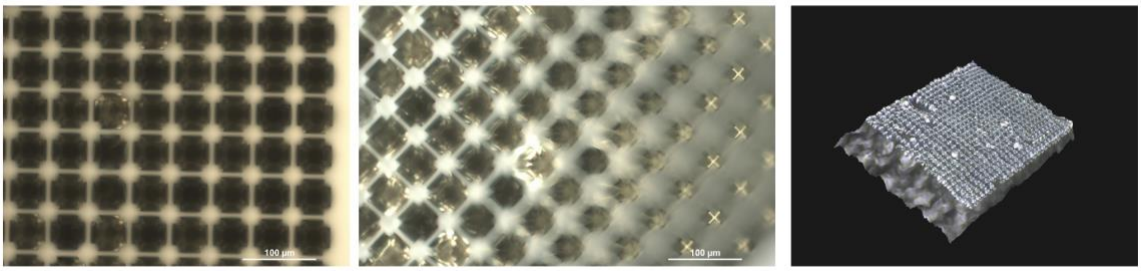

Top view **Tilt 15 degree** **3D Structure**

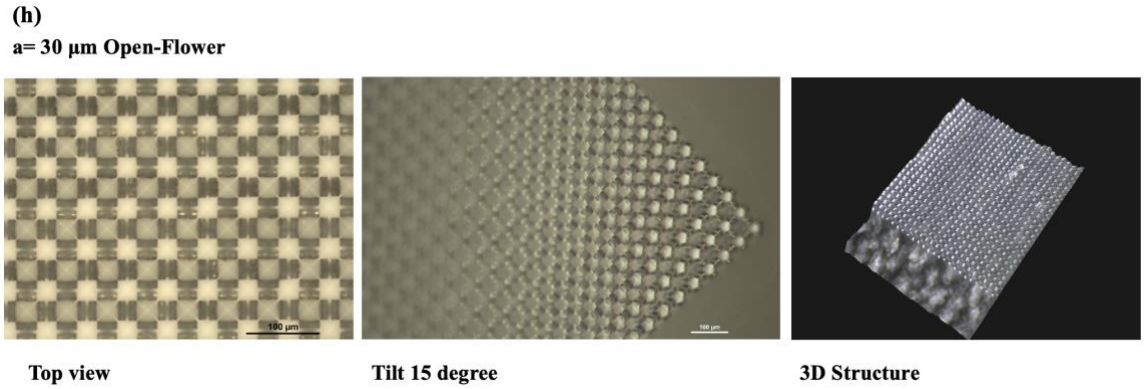

Figure 5.3. 4 Printed sample for closed-flower structure and open-flower structure with the different bottom lengths of the pyramid structure (a = 30 μm, 60 μm, 90 μm, and 120 μm, respectively).

The next step is to investigate the radiative cooling and heating function of the designed EAM. The experimentally measured emissivity (absorptivity) spectra of the EAM were performed by UV-Vis-NIR spectroscopy in the range of 0.4 μm – 3 μm and Fourier-transform infrared (FTIR) spectroscopy in the field of 4 μm – 16 μm. The results are shown in Fig. 5.3.5 (a). The common radiative cooling emitter requires wide-band emissivity from wavelengths 8 to 13 μm with a high emission rate. For a single layer of the closed-flower structure (a = 30 μm, 60 μm, 90 μm, and 120 μm), the peak emission rate is around 95% in the range of atmospheric window. As the bottom length *a* increasing, the peak emission rate goes higher. But the difference is tiny. On the other hand, for a single layer of the open-flower structure (a = 30 μm, 60 μm, 90 μm, and 120 μm), the emission rate decreased in the range of atmospheric window as the bottom length *a* increasing. The lowest emission rate occurs on the 30-μm open-flower structure. The absorptivity dependence on geometrical parameters can be attributed to the bottom width ratio and the gap distance. If the ratio is smaller, which indicates the gap is more

significant, it is easier for IR radiation to pass through the EAM, and the absorption rate is lower. To achieve both radiative cooling and heating by a double-layer structure, the difference of the emissivity between the open-flower and closed-flower structures is the most critical issue. The larger the difference will result in the better the radiative cooling and heating effect.

To evaluate the potential radiative cooling and heating effect of the EAM, the cooling power should be calculated. (Heating power is the opposite of cooling power. Therefore, we can calculate cooling power only.) Generally, the cooling power is subjected to the emitted radiative energy by the emitter and the absorbed atmospheric radiation by the structure. The detailed calculation steps are stated in the experiment section. Fig. 5.3.5 (b) shows the cooling power for a single layer of the emitter, including the closed-flower structure and the open-flower structure. A positive value of cooling power can cool a chamber below the ambient temperature. When the cooling power is 0, the value of the $(T_s - T_a)$ indicates the temperature difference can be achieved between the ambient environment and the covered chamber as the EAM was applied. On the other hand, when the $(T_s - T_a) = 0$, the net cooling power for the 30-μm closed-flower structure is as high as 185 W/m^2.

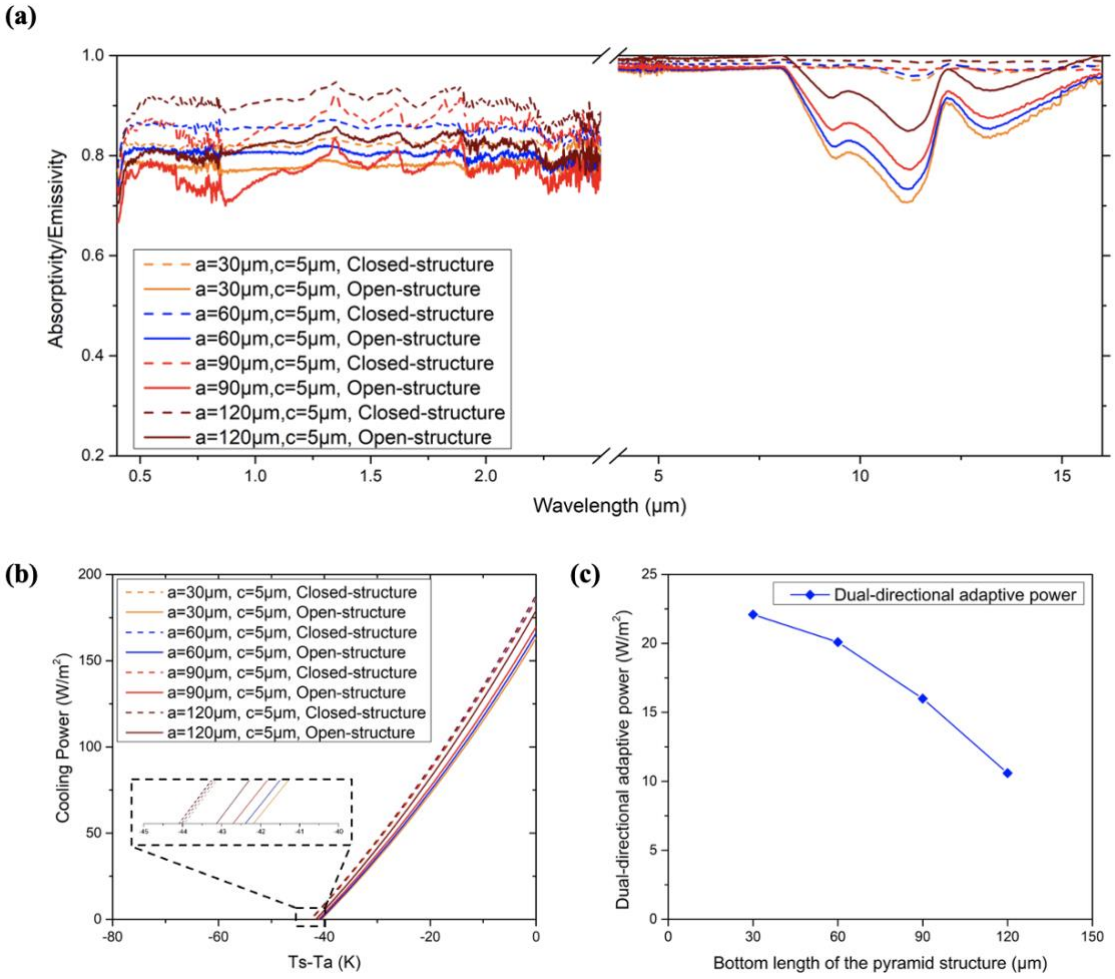

Figure 5.3. 5 Optical properties of the EAM. (a) Measured emissivity (absorptivity) of the EAM for different bottom lengths of the pyramid structure. The wavelength ranged from 0.4 μm to 3 μm was measured by UV-Vis-NIR and the wavelength ranged from 4 μm to 16 μm was measured by FTIR. (b) Calculated cooling power without the presence of nonradiative heat exchange for different bottom lengths of the pyramid structure. (c) Net cooling (heating) power of the designed EAM for different bottom lengths of the pyramid structure.

A dual-function membrane should be considered for both the cooling and heating power. For a double-layer structure, the closed-flower form towards the outside, and the open-flower form towards the inside to achieve radiative cooling when the ambient temperature is high. When the ambient temperature is low, the inside emitter changes to

the closed-flower structure and the outside emitter changes to the open-flower structure. At this moment, the dual-directional adaptive power can be calculated by the difference of the absorptivity for the closed-flower and open-flower structure based on the results in Fig. 5.3.5 (a). The dual-directional adaptive powers are shown in Fig. 5.3.5 (c). The EAM can exhibit "smart" radiative cooling and heating power at 22 W/m^2 when the 30-μm structures were applied.

The traditional evaluation criteria work for radiative cooling power only, which is not sufficient for dual-functional membranes. In this case, a novel strategy to evaluate the performance of dual-functional membranes should be generated. The dual-functional membranes exhibit both radiative cooling and heating functions. For a double-layer structure, the closed-flower form towards the outside, and the open-flower form towards the inside to achieve radiative cooling when the ambient temperature is high. The cooling power should be calculated by the reflected ambient IR radiation minus the conserved heat from the inside. When the ambient temperature is low, the inside emitter changes to the closed-flower structure, and the outside emitter changes to the open-flower structure. The heating power should be considered the difference between the absorbed ambient IR radiation and the inside heat emission. Therefore, the absorptivity difference for the inside and outside structure should be applied to the Eq. (5.1-5.5), i.e.

$$P_{dual-directional\ adaptive\ power} = |P_{outside} - P_{inside}| = |f\big(e_s(outside) - e_s(inside)\big)| \tag{5.6}$$

where the $e_s(outside)$ and $e_s(inside)$ refer to the emissivity of the outside layer and the inside layer, respectively. At this moment, the dual-directional adaptive power can be calculated by the difference of the absorptivity for the closed-flower and open-flower structures based on the results in Fig. 5.3.5 (a). The dual-directional adaptive powers are shown in Fig. 5.3.5 (c). The EAM can exhibit "smart" radiative cooling and heating power at 22 W/m^2 when the 30-μm structures were applied.

To measure the radiative cooling and heating effect of the EAM, a homemade thermographic camera system was set up. The testing system consists of an IR camera, one sample holder for the double-layer EAM, and the ambient temperature control system (Fig. 5.3.6 (a)). A 1-inch length hole was punched on an isothermal chamber to anchor the EAM sample. The EAM sample was fabricated by the 25x lens to print non-deformable structures on a 1.5 mm * 1.5 mm square. Due to the resolution of the IR camera is 50 μm, the structure size for the testing was using the 60-um closed-flower and open-flower structures. For the experiment group, the outside layer of the EAM sample is covered by the closed-flower structure, and the inside layer is covered by the open-flower structure. As the control group, a clean glass substrate was set on the sample position. The hot environment was achieved by a 250 W IR heater, and the cold climate was performed by a box of ice water mixture. Fig. 5.3.6 (b-c) shows the temperature distribution captured by the IR camera for the same heating duration (10 min) and the same cooling duration (30min) for the experiment group and control group, respectively. The average temperature of all the pixels in the black square in Fig. 5.3.6 (b-c) was calculated over time and plotted in Fig. 5.3.6 (d-e). The movies captured by the IR camera were collected

in the Supplementary Materials. As shown in Fig. 5.3.6 (d-e), the heating process and the cooling process of the experimental group are gentler than the control group, which indicates a feasible cooling and heating performance. The calculated dual-directional adaptive of the printed sample was 45 μW on the 1.5 mm * 1.5 mm square.

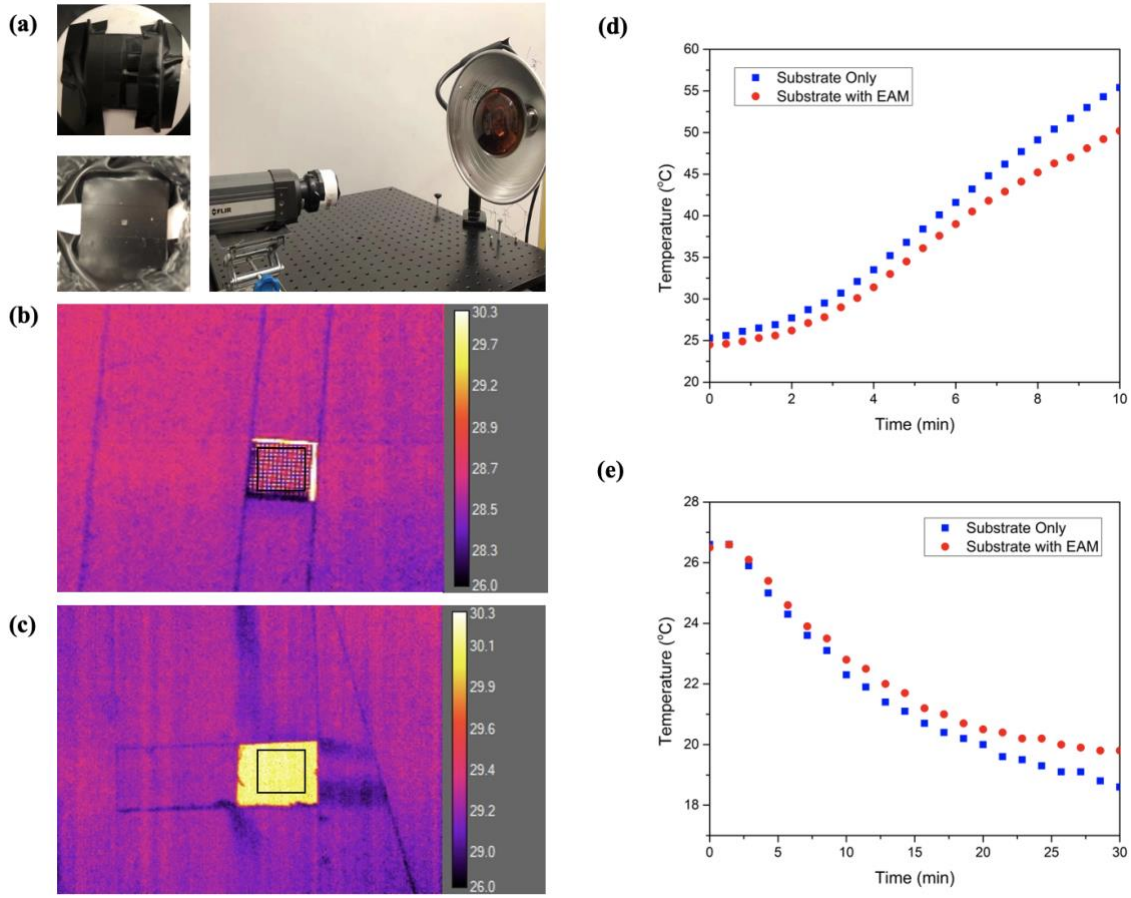

Figure 5.3. 6 Thermal measurement of the EAM. (a) The cooling and warming test system. (b, c) The temperature distribution of the experimental group and the control group respectively. (d) Cooling effect of the experiment group (EAM on the substrate) and the control group (substrate only), respectively. (e) Heating effect of the experiment group (EAM on the substrate) and the control group (substrate only), respectively.

5.4 Conclusion

In summary, the radiative cooling and heating performance of the environmentally-adaptive membrane has been experimentally and computationally demonstrated. A single-layer closed-flower structure can achieve passive radiative cooling power as high as 185 W/m^2. The radiative cooling and heating function is performed by a double-layered system according to the ambient temperature. Such environmentally-adaptive membrane will attract more and more attention for energy sustainability. This technology has a great potential to reduce the energy consumption of the HVAC systems for both buildings and EVs. With the advancement of printing technology, this EAM can be produced on flexible film. Then the EAM would be able to use on the textile to achieve personal thermal management.

CHAPTER VI

CONCLUSIONS AND FUTURE WORK

6.1 Conclusions

This dissertation describes the fundamental study of micro/nano-structured membranes in response to energy consumption which hinders water and energy sustainability. Sustainability has various meanings in the context of water acquisition and passive radiative energy saving.

Since pure GO can be significantly influenced by water flow and be damaged due to swelling and folding, which results in low stability for applications, C60 was selected as the skeleton to support GO layers for tuning the interlayer spacing. The C60 frame can also increase the stability of membranes through the covalent bonds between C60 and GO laminates which indicates over 10 hours stability. By adjusting the ratio of C60, the interlayer spacing can be fixed at 1.25 nm to achieve a high water flux up to 10.85 L h^{-1} m^{-2} bar^{-1} and a high ion rejection rate of 89.66%. The cross-section membrane filtration technique can reduce the steric effect during the water molecule transportation in the GO laminates and minimize energy consumption up to 0.94 kWh/m^3. By increasing the water permeance of GO-based membrane via several strategies, the energy consumption for water desalination is reduced to meet water sustainability requirements.

Although water desalination can be achieved by GO-based membranes, energy efficiency and scalability are still the bottlenecks for further commercialization. In this

dissertation, gradient membranes were designed and assembled with graphene oxide and celluloses laminates and then used for RO desalination. The water flowing path was tuned by graphene oxide sizes while salt/water separation was tailored by the graphene oxide interlayer crosslinking. By optimizing the GO laminates' thickness and the GO nanosheet's lateral dimension, the length of the water pathway can be significantly reduced, and thereby the energy consumption is reduced, while maintaining the water desalination performance. The gradient nanocomposite membranes exhibit water permeance as high as 21.34 L h^{-1} m^{-2} bar^{-1} and ion rejection rate > 96.08%, indicating a 35.8% energy saving on membrane filtration for brackish water.

Passive radiative cooling and heating is another critical energy problem for global sustainability. The cooling and heating systems consume a large amount of electricity. To overcome this problem, many promising technologies have been developed. However, most of these approaches are monofunctional, which can only solve the problem of radiative cooling or heating and cannot adapt the function according to the ambient temperature. PNIPAM is a well-established polymer exhibiting a substantial response to temperature changes. In this dissertation, an EAM for both radiative cooling and heating can be achieved by PNIPAM-based hydrogel. The controlled shape transformation between closed-flower structure and open-flower structure can be achieved by varying the local exposure dose in two-photon laser lithography. This transformation can be completed in 1 min. The cooling power for a single-layer system can achieve up to 185 W/m^2. The radiative cooling and heating function is performed by a double-layered system according to the ambient temperature. The dual-directional cooling and heating power for

the EAM can achieve 22 W/m^2. Such environmentally-adaptive membranes will attract more and more attention for energy sustainability. This technology has a great potential to reduce the energy consumption of the HVAC systems for both buildings and EVs. With the advancement of printing technology, this EAM can be produced on flexible film. Then the EAM would be able to use on the textile to achieve personal thermal management.

6.2 Future Work

1) The biofouling issue is one of the most severe problems associated with membrane applications for water desalination. The performance and lifetime of a membrane are highly dependent on the antifouling properties. The antifouling properties of GO-based membrane must be further investigated. A combination of energy-efficient desalination performance and antifouling performance would significantly contribute to the application of GO-based RO membranes.
2) 3D printing technology is a promising method for nano-/micro-structure fabrication. However, it is challenging to scale-up. For passive radiative cooling and heating membranes, scalability is a critical issue. More efforts ought to develop scalable fabrication methods or substitute materials to achieve large-scale membranes for environmentally-adaptive self-cooling and heating functions.
3) Solar energy is a key part of the heat source. Radiative warming has been widely used for thousands of years. On the other hand, due to the higher requirements of

comfortable temperature, it is essential to introduce other technologies to address solar power for not only radiative heating but also passive radiative cooling.

REFERENCES

1. *AQUASTAT - FAO's Global Information System on Water and Agriculture*. 10/01/2019]; Available from: http://www.fao.org/nr/water/aquastat/water_use/index.stm.

2. Sapkota, A.R., *Water reuse, food production and public health: Adopting transdisciplinary, systems-based approaches to achieve water and food security in a changing climate*. 2019, Elsevier.

3. Teow, Y.H. and A.W. Mohammad, *New generation nanomaterials for water desalination: A review.* Desalination, 2019. **451**: p. 2-17.

4. *How Much Water is There on Earth?* 10/01/2019]; Available from: https://water.usgs.gov/edu/earthhowmuch.html.

5. Rodell, M., et al., *Emerging trends in global freshwater availability.* Nature, 2018. **557**(7707): p. 651.

6. Shenvi, S.S., A.M. Isloor, and A. Ismail, *A review on RO membrane technology: developments and challenges.* Desalination, 2015. **368**: p. 10-26.

7. Elimelech, M. and W.A. Phillip, *The future of seawater desalination: energy, technology, and the environment.* science, 2011. **333**(6043): p. 712-717.

8. García-Pacheco, R., et al., *Validation of recycled membranes for treating brackish water at pilot scale.* Desalination, 2018. **433**: p. 199-208.

9. Liu, Q. and G.-R. Xu, *Graphene oxide (GO) as functional material in tailoring polyamide thin film composite (PA-TFC) reverse osmosis (RO) membranes.* Desalination, 2016. **394**: p. 162-175.

10. Zarzo, D. and D. Prats, *Desalination and energy consumption. What can we expect in the near future?* Desalination, 2018. **427**: p. 1-9.

11. Center, B.P., *Annual Energy Outlook 2020.* 2020.

12. Ürge-Vorsatz, D., et al., *Measuring the co-benefits of climate change mitigation.* Annual Review of Environment and Resources, 2014. **39**: p. 549-582.

13. Fang, H., et al., *Performance evaluation of a metamaterial-based new cool roof using improved Roof Thermal Transfer Value model.* Applied Energy, 2019. **248**: p. 589-599.

14. Zhao, B., et al., *Radiative cooling: A review of fundamentals, materials, applications, and prospects.* Applied energy, 2019. **236**: p. 489-513.

15. Shi, Q., et al., *Water desalination and biofuel dehydration through a thin membrane of polymer of intrinsic microporosity: Atomistic simulation study.* Journal of Membrane Science, 2018. **545**: p. 49-56.

16. Akhavan, M., J. Schofield, and S. Jalili, *Water transport and desalination through double-layer graphyne membranes.* Physical Chemistry Chemical Physics, 2018. **20**(19): p. 13607-13615.

17. Wei, G.L., et al., *Superpermeable Atomic -Thin Graphene Membranes with High Selectivity.* Acs Nano, 2017. **11**(2): p. 1920-1926.

18. Russo, C.J. and J.A. Golovchenko, *Atom-by-atom nucleation and growth of graphene nanopores.* Proceedings of the National Academy of Sciences of the United States of America, 2012. **109**(16): p. 5953-5957.

19. Surwade, S.P., et al., *Water desalination using nanoporous single-layer graphene.* Nature nanotechnology, 2015. **10**(5): p. 459-464.

20. Abraham, J., et al., *Tunable sieving of ions using graphene oxide membranes.* Nature Nanotechnology, 2017. **12**(6): p. 546-+.

21. Joshi, R.K., et al., *Precise and Ultrafast Molecular Sieving Through Graphene Oxide Membranes.* Science, 2014. **343**(6172): p. 752-754.

22. Yang, Q., et al., *Ultrathin graphene-based membrane with precise molecular sieving and ultrafast solvent permeation.* Nature Materials, 2017. **16**(12): p. 1198-+.

23. Surwade, S.P., et al., *Water desalination using nanoporous single-layer graphene.* Nature nanotechnology, 2015. **10**(5): p. 459.

24. Boretti, A., et al., *Outlook for graphene-based desalination membranes.* npj Clean Water, 2018. **1**(1): p. 1-11.

25. Hummers Jr, W.S. and R.E. Offeman, *Preparation of graphitic oxide.* Journal of the american chemical society, 1958. **80**(6): p. 1339-1339.

26. Marcano, D.C., et al., *Improved synthesis of graphene oxide.* ACS nano, 2010. **4**(8): p. 4806-4814.

27. Stankovich, S., et al., *Synthesis of graphene-based nanosheets via chemical reduction of exfoliated graphite oxide.* carbon, 2007. **45**(7): p. 1558-1565.

28. Bourlinos, A.B., et al., *Graphite oxide: chemical reduction to graphite and surface modification with primary aliphatic amines and amino acids.* Langmuir, 2003. **19**(15): p. 6050-6055.

29. Joshi, R., et al., *Precise and ultrafast molecular sieving through graphene oxide membranes.* science, 2014. **343**(6172): p. 752-754.

30. Su, Y., et al., *Impermeable barrier films and protective coatings based on reduced graphene oxide.* Nature communications, 2014. **5**: p. 4843.

31. Nair, R., et al., *Unimpeded permeation of water through helium-leak–tight graphene-based membranes.* Science, 2012. **335**(6067): p. 442-444.

32. Wang, W., et al., *Graphene oxide membranes with tunable permeability due to embedded carbon dots.* Chemical Communications, 2014. **50**(86): p. 13089-13092.

33. El-Deen, A.G., N.A. Barakat, and H.Y. Kim, *Graphene wrapped MnO2-nanostructures as effective and stable electrode materials for capacitive deionization desalination technology.* Desalination, 2014. **344**: p. 289-298.

34. Gao, S.J., et al., *SWCNT-intercalated GO ultrathin films for ultrafast separation of molecules.* Journal of Materials Chemistry A, 2015. **3**(12): p. 6649-6654.

35. Huang, H., et al., *Ultrafast viscous water flow through nanostrand-channelled graphene oxide membranes.* Nature communications, 2013. **4**: p. 2979.

36. Chen, L., et al., *Ion sieving in graphene oxide membranes via cationic control of interlayer spacing.* Nature, 2017. **550**(7676): p. 380.

37. Abraham, J., et al., *Tunable sieving of ions using graphene oxide membranes.* Nature Nanotechnology, 2017.

38. Mi, B., *Graphene oxide membranes for ionic and molecular sieving.* Science, 2014. **343**(6172): p. 740-742.

39. Hung, W.-S., et al., *Cross-linking with diamine monomers to prepare composite graphene oxide-framework membranes with varying d-spacing.* Chemistry of Materials, 2014. **26**(9): p. 2983-2990.

40. Zhang, Y., S. Zhang, and T.-S. Chung, *Nanometric graphene oxide framework membranes with enhanced heavy metal removal via nanofiltration.* Environmental science & technology, 2015. **49**(16): p. 10235-10242.

41. Feng, B., K. Xu, and A. Huang, *Covalent synthesis of three-dimensional graphene oxide framework (GOF) membrane for seawater desalination.* Desalination, 2016. **394**: p. 123-130.

42. Yin, X., et al., *Terrestrial radiative cooling: Using the cold universe as a renewable and sustainable energy source.* Science, 2020. **370**(6518): p. 786-791.

43. Hossain, M.M. and M. Gu, *Radiative cooling: principles, progress, and potentials.* Advanced Science, 2016. **3**(7): p. 1500360.

44. Zhao, D., et al., *Radiative sky cooling: Fundamental principles, materials, and applications.* Applied Physics Reviews, 2019. **6**(2): p. 021306.

45. Vinnikov, K.Y. and N.C. Grody, *Global warming trend of mean tropospheric temperature observed by satellites.* Science, 2003. **302**(5643): p. 269-272.

46. Raman, A.P., et al., *Passive radiative cooling below ambient air temperature under direct sunlight.* Nature, 2014. **515**(7528): p. 540-544.

47. Gentle, A.R. and G.B. Smith, *A subambient open roof surface under the Mid‐Summer sun.* Advanced Science, 2015. **2**(9): p. 1500119.

48. Zhai, Y., et al., *Scalable-manufactured randomized glass-polymer hybrid metamaterial for daytime radiative cooling.* Science, 2017. **355**(6329): p. 1062-1066.

49. Zhao, D., et al., *Roof-integrated radiative air-cooling system to achieve cooler attic for building energy saving.* Energy and Buildings, 2019. **203**: p. 109453.

50. Zhang, H., et al., *Biologically inspired flexible photonic films for efficient passive radiative cooling.* Proceedings of the National Academy of Sciences, 2020. **117**(26): p. 14657-14666.

51. Okada, M., M. Okada, and H. Kusaka, *Dependence of Atmospheric Cooling by Vegetation on Canopy Surface Area During Radiative Cooling at Night: Physical Model Evaluation Using a Polyethylene Chamber.* Journal of Agricultural Meteorology, 2016. **72**(1): p. 20-28.

52. Choi, S.H., et al., *Anderson light localization in biological nanostructures of native silk.* Nature communications, 2018. **9**(1): p. 1-14.

53. Shi, N.N., et al., *Keeping cool: Enhanced optical reflection and radiative heat dissipation in Saharan silver ants.* Science, 2015. **349**(6245): p. 298-301.

54. Rephaeli, E., A. Raman, and S. Fan, *Ultrabroadband photonic structures to achieve high-performance daytime radiative cooling.* Nano letters, 2013. **13**(4): p. 1457-1461.

55. Hossain, M.M., B. Jia, and M. Gu, *A metamaterial emitter for highly efficient radiative cooling.* Advanced Optical Materials, 2015. **3**(8): p. 1047-1051.

56. Li, T., et al., *A radiative cooling structural material.* Science, 2019. **364**(6442): p. 760-763.

57. Chae, D., et al., *Spectrally selective inorganic-based multilayer emitter for daytime radiative cooling.* ACS applied materials & interfaces, 2020. **12**(7): p. 8073-8081.

58. Zhang, X., *Metamaterials for perpetual cooling at large scales.* Science, 2017. **355**(6329): p. 1023-1024.

59. Mandal, J., et al., *Hierarchically porous polymer coatings for highly efficient passive daytime radiative cooling.* Science, 2018. **362**(6412): p. 315-319.

60. Aili, A., et al., *Selection of polymers with functional groups for daytime radiative cooling.* Materials Today Physics, 2019. **10**: p. 100127.

61. Yang, P., C. Chen, and Z.M. Zhang, *A dual-layer structure with record-high solar reflectance for daytime radiative cooling.* Solar Energy, 2018. **169**: p. 316-324.

62. Chen, Y., et al., *Colored and paintable bilayer coatings with high solar-infrared reflectance for efficient cooling.* Science Advances, 2020. **6**(17): p. eaaz5413.

63. Czapla, B., et al. *Potential for Passive Radiative Cooling by PDMS Selective Emitters*. in *ASME 2017 Heat Transfer Summer Conference*. 2017. American Society of Mechanical Engineers.

64. Hu, M., et al., *Field test and preliminary analysis of a combined diurnal solar heating and nocturnal radiative cooling system.* Applied Energy, 2016. **179**: p. 899-908.

65. Palik, E.D., *Handbook of optical constants of solids*. Vol. 3. 1998: Academic press.

66. Berdahl, P., *Radiative cooling with MgO and/or LiF layers.* Applied optics, 1984. **23**(3): p. 370-372.

67. Raman, A.P., et al., *Passive radiative cooling below ambient air temperature under direct sunlight.* Nature, 2014. **515**(7528): p. 540-544.

68. Kecebas, M.A., et al., *Passive radiative cooling design with broadband optical thin-film filters.* Journal of Quantitative Spectroscopy and Radiative Transfer, 2017. **198**: p. 179-186.

69. Huang, Y., et al., *Broadband metamaterial as an "invisible" radiative cooling coat.* Optics Communications, 2018. **407**: p. 204-207.

70. Mandal, J., et al., *Paints as a scalable and effective radiative cooling technology for buildings.* Joule, 2020. **4**(7): p. 1350-1356.

71. Leroy, A., et al., *High-performance subambient radiative cooling enabled by optically selective and thermally insulating polyethylene aerogel.* Science advances, 2019. **5**(10): p. eaat9480.

72. Hsu, P.-C., et al., *Radiative human body cooling by nanoporous polyethylene textile.* Science, 2016. **353**(6303): p. 1019-1023.

73. Mandal, J., et al., *Li4Ti5O12: A visible‐to‐infrared broadband electrochromic material for optical and thermal management.* Advanced Functional Materials, 2018. **28**(36): p. 1802180.

74. Bao, H., et al., *Double-layer nanoparticle-based coatings for efficient terrestrial radiative cooling.* Solar Energy Materials and Solar Cells, 2017. **168**: p. 78-84.

75. Wei, G., et al., *Fabrication of multifunctional coating with high luminous transmittance, self-cleaning and radiative cooling performances for energy-efficient windows.* Solar Energy Materials and Solar Cells, 2019. **202**: p. 110125.

76. Zhu, L., et al., *Radiative cooling of solar cells.* Optica, 2014. **1**(1): p. 32-38.

77. Zhu, L., A.P. Raman, and S. Fan, *Radiative cooling of solar absorbers using a visibly transparent photonic crystal thermal blackbody.* Proceedings of the national academy of sciences, 2015. **112**(40): p. 12282-12287.

78. Zhu, L., A. Raman, and S. Fan, *Color-preserving daytime radiative cooling.* Applied Physics Letters, 2013. **103**(22): p. 223902.

79. Lu, Y., et al., *A universal route to realize radiative cooling and light management in photovoltaic modules.* Solar Rrl, 2017. **1**(10): p. 1700084.

80. Wu, D., et al., *The design of ultra-broadband selective near-perfect absorber based on photonic structures to achieve near-ideal daytime radiative cooling.* Materials & Design, 2018. **139**: p. 104-111.

81. Ono, M., et al., *Self-adaptive radiative cooling based on phase change materials.* Optics express, 2018. **26**(18): p. A777-A787.

82. Li, W., et al., *Photonic thermal management of coloured objects.* Nature communications, 2018. **9**(1): p. 1-8.

83. Hsu, P.-C., et al., *A dual-mode textile for human body radiative heating and cooling.* Science advances, 2017. **3**(11): p. e1700895.

84. Zhang, X.A., et al., *Dynamic gating of infrared radiation in a textile.* Science, 2019. **363**(6427): p. 619-623.

85. Afgan, N.H., M. Darwish, and M.G. Carvalho, *Sustainability assessment of desalination plants for water production.* Desalination, 1999. **124**(1-3): p. 19-31.

86. Shannon, M.A., et al., *Science and technology for water purification in the coming decades.* Nature, 2008. **452**(7185): p. 301-310.

87. Werber, J.R., C.O. Osuji, and M. Elimelech, *Materials for next-generation desalination and water purification membranes.* Nature Reviews Materials, 2016. **1**: p. 16018.

88. Mahmoud, K.A., et al., *Functional graphene nanosheets: the next generation membranes for water desalination.* Desalination, 2015. **356**: p. 208-225.

89. Humplik, T., et al., *Nanostructured materials for water desalination.* Nanotechnology, 2011. **22**(29): p. 292001.

90. Zhao, F.-Y., et al., *High-flux positively charged nanocomposite nanofiltration membranes filled with poly (dopamine) modified multiwall carbon nanotubes.* ACS applied materials & interfaces, 2016. **8**(10): p. 6693-6700.

91. Zhang, C., et al., *Graphene oxide quantum dots incorporated into a thin film nanocomposite membrane with high flux and antifouling properties for low-pressure nanofiltration.* ACS applied materials & interfaces, 2017. **9**(12): p. 11082-11094.

92. Song, X., et al., *Charge-Gated Ion Transport through Polyelectrolyte Intercalated Amine Reduced Graphene Oxide Membranes.* ACS applied materials & interfaces, 2017. **9**(47): p. 41482-41495.

93. Chen, B., et al., *Molecular Insight into Water Desalination across Multilayer Graphene Oxide Membranes.* ACS applied materials & interfaces, 2017. **9**(27): p. 22826-22836.

94. Rollings, R.C., A.T. Kuan, and J.A. Golovchenko, *Ion selectivity of graphene nanopores.* Nature communications, 2016. **7**.

95. Yuan, Y., et al., *Enhanced desalination performance of carboxyl functionalized graphene oxide nanofiltration membranes.* Desalination, 2017. **405**: p. 29-39.

96. Xu, X.-L., et al., *Graphene oxide nanofiltration membranes stabilized by cationic porphyrin for high salt rejection.* ACS applied materials & interfaces, 2016. **8**(20): p. 12588-12593.

97. Kim, H.W., et al., *Selective gas transport through few-layered graphene and graphene oxide membranes.* Science, 2013. **342**(6154): p. 91-95.

98. Koenig, S.P., et al., *Selective molecular sieving through porous graphene.* Nature nanotechnology, 2012. **7**(11): p. 728-732.

99. Li, H., et al., *Ultrathin, molecular-sieving graphene oxide membranes for selective hydrogen separation.* Science, 2013. **342**(6154): p. 95-98.

100. Wang, H., et al., *Graphene-wrapped sulfur particles as a rechargeable lithium–sulfur battery cathode material with high capacity and cycling stability.* Nano letters, 2011. **11**(7): p. 2644-2647.

101. Yao, F., et al., *Diffusion mechanism of lithium ion through basal plane of layered graphene.* Journal of the American Chemical Society, 2012. **134**(20): p. 8646-8654.

102. Cohen-Tanugi, D. and J.C. Grossman, *Water desalination across nanoporous graphene.* Nano letters, 2012. **12**(7): p. 3602-3608.

103. Goh, K., et al., *All‐Carbon Nanoarchitectures as High‐Performance Separation Membranes with Superior Stability.* Advanced Functional Materials, 2015. **25**(47): p. 7348-7359.

104. Nasibulin, A.G., et al., *A novel hybrid carbon material.* Nature Nanotechnology, 2007. **2**(3): p. 156.

105. Su, S., et al., *Efficient photothermal therapy of brain cancer through porphyrin functionalized graphene oxide.* New Journal of Chemistry, 2015. **39**(7): p. 5743-5749.

106. Yu, D., et al., *Fullerene-grafted graphene for efficient bulk heterojunction polymer photovoltaic devices.* The journal of physical chemistry letters, 2011. **2**(10): p. 1113-1118.

107. Jin, W., A. Toutianoush, and B. Tieke, *Use of polyelectrolyte layer-by-layer assemblies as nanofiltration and reverse osmosis membranes.* Langmuir, 2003. **19**(7): p. 2550-2553.

108. Konatham, D., et al., *Simulation insights for graphene-based water desalination membranes.* Langmuir, 2013. **29**(38): p. 11884-11897.

109. Chowdhuri, S. and A. Chandra, *Molecular dynamics simulations of aqueous NaCl and KCl solutions: Effects of ion concentration on the single-particle, pair, and collective dynamical properties of ions and water molecules.* The Journal of Chemical Physics, 2001. **115**(8): p. 3732-3741.

110. Szymczyk, A., et al., *Contribution of convection, diffusion and migration to electrolyte transport through nanofiltration membranes.* Advances in Colloid and Interface Science, 2003. **103**(1): p. 77-94.

111. Szymczyk, A. and P. Fievet, *Investigating transport properties of nanofiltration membranes by means of a steric, electric and dielectric exclusion model.* Journal of membrane science, 2005. **252**(1-2): p. 77-88.

112. Tsoukleri, G., et al., *Subjecting a graphene monolayer to tension and compression.* small, 2009. **5**(21): p. 2397-2402.

113. Choi, J., et al., *Three-dimensional integration of graphene via swelling, shrinking, and adaptation.* Nano letters, 2015. **15**(7): p. 4525-4531.

114. Wei, Y., et al., *Bending rigidity and Gaussian bending stiffness of single-layered graphene.* Nano letters, 2012. **13**(1): p. 26-30.

115. Heiranian, M., A.B. Farimani, and N.R. Aluru, *Water desalination with a single-layer MoS2 nanopore.* Nature communications, 2015. **6**.

116. nan Shen, J., et al., *Preparation and characterization of thin-film nanocomposite membranes embedded with poly (methyl methacrylate) hydrophobic modified multiwalled carbon nanotubes by interfacial polymerization.* Journal of membrane science, 2013. **442**: p. 18-26.

117. Baek, Y., et al., *Evaluation of carbon nanotube-polyamide thin-film nanocomposite reverse osmosis membrane: Surface properties, performance characteristics and fouling behavior.* Journal of industrial and engineering chemistry, 2017. **56**: p. 327-334.

118. Chen, L., et al., *Ion sieving in graphene oxide membranes via cationic control of interlayer spacing.* Nature, 2017. **550**(7676): p. 380-383.

119. Yin, J., G. Zhu, and B. Deng, *Graphene oxide (GO) enhanced polyamide (PA) thin-film nanocomposite (TFN) membrane for water purification.* Desalination, 2016. **379**: p. 93-101.

120. Goh, K., et al., *Graphene oxide as effective selective barriers on a hollow fiber membrane for water treatment process.* Journal of Membrane Science, 2015. **474**: p. 244-253.

121. Perreault, F., M.E. Tousley, and M. Elimelech, *Thin-film composite polyamide membranes functionalized with biocidal graphene oxide nanosheets.* Environmental Science & Technology Letters, 2014. **1**(1): p. 71-76.

122. Ali, M.E., et al., *Thin film composite membranes embedded with graphene oxide for water desalination.* Desalination, 2016. **386**: p. 67-76.

123. Safarpour, M., A. Khataee, and V. Vatanpour, *Thin film nanocomposite reverse osmosis membrane modified by reduced graphene oxide/TiO2 with improved desalination performance.* Journal of Membrane Science, 2015. **489**: p. 43-54.

124. Wang, T., et al., *Effects of acyl chloride monomer functionality on the properties of polyamide reverse osmosis (RO) membrane.* Journal of membrane science, 2013. **440**: p. 48-57.

125. Said, M., A. Gad, and S. Kandil, *Toward energy efficient reverse osmosis polyamide thin-film composite membrane based on diaminotoluene.* Desalination and Water Treatment, 2017. **71**: p. 261-270.

126. Hong, S., et al., *Interfacially synthesized chlorine-resistant polyimide thin film composite (TFC) reverse osmosis (RO) membranes*. Desalination, 2013. **309**: p. 18-26.

127. Jewrajka, S.K., et al., *Use of 2, 4, 6-pyridinetricarboxylic acid chloride as a novel co-monomer for the preparation of thin film composite polyamide membrane with improved bacterial resistance.* Journal of membrane science, 2013. **439**: p. 87-95.

128. Peyki, A., A. Rahimpour, and M. Jahanshahi, *Preparation and characterization of thin film composite reverse osmosis membranes incorporated with hydrophilic SiO2 nanoparticles.* Desalination, 2015. **368**: p. 152-158.

129. Zargar, M., et al., *Polyethylenimine modified silica nanoparticles enhance interfacial interactions and desalination performance of thin film nanocomposite membranes.* Journal of Membrane Science, 2017. **541**: p. 19-28.

130. Zhao, H., et al., *Improving the performance of polyamide reverse osmosis membrane by incorporation of modified multi-walled carbon nanotubes.* Journal of Membrane Science, 2014. **450**: p. 249-256.

131. Khan, A.U.H., Z. Khan, and I.H. Aljundi, *Improved hydrophilicity and anti-fouling properties of polyamide TFN membrane comprising carbide derived carbon.* Desalination, 2017. **420**: p. 125-135.

132. Fathizadeh, M., et al., *Polyamide/nitrogen-doped graphene oxide quantum dots (N-GOQD) thin film nanocomposite reverse osmosis membranes for high flux desalination.* Desalination, 2019. **451**: p. 125-132.

133. Al Mayyahi, A., *TiO2 polyamide thin film nanocomposite reverses osmosis membrane for water desalination.* Membranes, 2018. **8**(3): p. 66.

134. Zhao, Y., et al., *Synthesis of robust and high-performance aquaporin-based biomimetic membranes by interfacial polymerization-membrane preparation and RO performance characterization.* Journal of Membrane Science, 2012. **423**: p. 422-428.

135. Xie, W., et al., *An aquaporin-based vesicle-embedded polymeric membrane for low energy water filtration.* Journal of Materials Chemistry A, 2013. **1**(26): p. 7592-7600.

136. Chan, W.-F., E. Marand, and S.M. Martin, *Novel zwitterion functionalized carbon nanotube nanocomposite membranes for improved RO performance and surface anti-biofouling resistance.* Journal of membrane science, 2016. **509**: p. 125-137.

137. Vatanpour, V., et al., *A thin film nanocomposite reverse osmosis membrane containing amine-functionalized carbon nanotubes.* Separation and Purification Technology, 2017. **184**: p. 135-143.

138. Farahbakhsh, J., M. Delnavaz, and V. Vatanpour, *Investigation of raw and oxidized multiwalled carbon nanotubes in fabrication of reverse osmosis polyamide membranes for improvement in desalination and antifouling properties.* Desalination, 2017. **410**: p. 1-9.

139. Abraham, J., et al., *Tunable sieving of ions using graphene oxide membranes.* Nature nanotechnology, 2017. **12**(6): p. 546.

140. Zheng, J., et al., *A non-MPD-type reverse osmosis membrane with enhanced permselectivity for brackish water desalination.* Journal of Membrane Science, 2018. **565**: p. 104-111.

141. Park, S.-J., et al., *Aromatic solvent-assisted interfacial polymerization to prepare high performance thin film composite reverse osmosis membranes based on hydrophilic supports.* Polymer, 2018. **144**: p. 159-167.

142. Azelee, I.W., et al., *Enhanced desalination of polyamide thin film nanocomposite incorporated with acid treated multiwalled carbon nanotube-titania nanotube hybrid.* Desalination, 2017. **409**: p. 163-170.

143. Kim, S.G., et al., *Nanocomposite poly (arylene ether sulfone) reverse osmosis membrane containing functional zeolite nanoparticles for seawater desalination.* Journal of membrane science, 2013. **443**: p. 10-18.

144. Voutchkov, N., *Energy use for membrane seawater desalination–current status and trends.* Desalination, 2018. **431**: p. 2-14.

145. Stanton, J.S. and K.F. Dennehy, *Brackish Groundwater and its Potential to Augment Freshwater Supplies*. 2017, US Geological Survey.

146. Karabelas, A., et al., *Analysis of specific energy consumption in reverse osmosis desalination processes.* Desalination, 2018. **431**: p. 15-21.

147. Thomas, J.A. and A.J. McGaughey, *Reassessing fast water transport through carbon nanotubes.* Nano letters, 2008. **8**(9): p. 2788-2793.

148. Su, J. and H. Guo, *Effect of nanochannel dimension on the transport of water molecules.* The Journal of Physical Chemistry B, 2012. **116**(20): p. 5925-5932.

149. Werber, J.R., C.O. Osuji, and M. Elimelech, *Materials for next-generation desalination and water purification membranes.* Nature Reviews Materials, 2016. **1**(5): p. 16018.

150. Tang, C., et al., *Biomimetic aquaporin membranes coming of age.* Desalination, 2015. **368**: p. 89-105.

151. Liu, Y., Z. Zhang, and S. Wang, *Carbon Nanopore-Tailored Reverse Osmotic Water Desalination.* ACS ES&T Water, 2020.

152. Liu, Y., et al., *Fullerene-tailored graphene oxide interlayer spacing for energy-efficient water desalination.* ACS Applied Nano Materials, 2018. **1**(11): p. 6168-6175.

153. Cohen-Tanugi, D., et al., *Quantifying the potential of ultra-permeable membranes for water desalination.* Energy & Environmental Science, 2014. **7**(3): p. 1134-1141.

154. Park, S., et al., *Graphene oxide papers modified by divalent ions—enhancing mechanical properties via chemical cross-linking.* ACS nano, 2008. **2**(3): p. 572-578.

155. ; Available from: http://www.emdmillipore.com/US/en/product/MF-Millipore-Membrane-Filters,MM_NF-C152#specifications.

156. Berkooz, G., P. Holmes, and J.L. Lumley, *The proper orthogonal decomposition in the analysis of turbulent flows.* Annual review of fluid mechanics, 1993. **25**(1): p. 539-575.

157. Cohen-Tanugi, D. and J.C. Grossman, *Mechanical strength of nanoporous graphene as a desalination membrane.* Nano letters, 2014. **14**(11): p. 6171-6178.

158. Sun, P., K. Wang, and H. Zhu, *Recent developments in graphene‐based membranes: structure, mass‐transport mechanism and potential applications.* Advanced Materials, 2016. **28**(12): p. 2287-2310.

159. Kafy, A., et al., *Cellulose/graphene nanocomposite as multifunctional electronic and solvent sensor material.* Materials Letters, 2015. **159**: p. 20-23.

160. Zhang, M. and L. Song, *Pressure-dependent permeate flux in ultra-and microfiltration.* Journal of environmental engineering, 2000. **126**(7): p. 667-674.

161. Werber, J.R., A. Deshmukh, and M. Elimelech, *The critical need for increased selectivity, not increased water permeability, for desalination membranes.* Environmental Science & Technology Letters, 2016. **3**(4): p. 112-120.

162. Said, M., et al., *Toward energy efficient reverse osmosis polyamide thin-film composite membrane based on diaminotoluene.* DESALINATION AND WATER TREATMENT, 2017. **71**: p. 261-270.

163. *Connecting Texas Water Data Workshops*. 2018, Texas Water Development Board.

164. Dong, H., et al., *High-flux reverse osmosis membranes incorporated with NaY zeolite nanoparticles for brackish water desalination*. Journal of Membrane Science, 2015. **476**: p. 373-383.

165. Chae, H.-R., et al., *Graphene oxide-embedded thin-film composite reverse osmosis membrane with high flux, anti-biofouling, and chlorine resistance.* Journal of Membrane Science, 2015. **483**: p. 128-135.

166. *The Future of Desalination in Texas*. 2018, Texas Water Development Board.

167. Li, X., et al., *Nature gives the best solution for desalination: Aquaporin-based hollow fiber composite membrane with superior performance.* Journal of membrane science, 2015. **494**: p. 68-77.

168. Ding, W., et al., *Fabrication of an aquaporin-based forward osmosis membrane through covalent bonding of a lipid bilayer to a microporous support.* Journal of Materials Chemistry A, 2015. **3**(40): p. 20118-20126.

169. Cohen-Tanugi, D. and J.C. Grossman, *Nanoporous graphene as a reverse osmosis membrane: recent insights from theory and simulation.* Desalination, 2015. **366**: p. 59-70.

170. Yang, Z., X.-H. Ma, and C.Y. Tang, *Recent development of novel membranes for desalination.* Desalination, 2018. **434**: p. 37-59.

171. *EV Auxiliary Systems Impacts*. Available from: http://avt.inl.gov/sites/default/files/pdf/fsev/auxiliary.pdf.

172. Granqvist, C., *Radiative heating and cooling with spectrally selective surfaces.* Applied Optics, 1981. **20**(15): p. 2606-2615.

173. Sun, D., R.T. Pinker, and M. Kafatos, *Diurnal temperature range over the United States: A satellite view*. Geophysical research letters, 2006. **33**(5).

174. Qu, M., J. Wan, and X. Hao, *Analysis of diurnal air temperature range change in the continental United States.* Weather and Climate Extremes, 2014. **4**: p. 86-95.

175. Berko, J., et al., *Deaths attributed to heat, cold, and other weather events in the United States, 2006–2010.* 2014.

176. CDC. *Heat-related deaths after an extreme heat event—four states, 2012, and United States, 1999–2009*. 2013; Available from: http://www.cdc.gov/mmwr/pdf/wk/mm6222.pdf.

177. Lichtman, J.H., et al., *Average temperature, diurnal temperature variation, and stroke hospitalizations.* Journal of Stroke and Cerebrovascular Diseases, 2016. **25**(6): p. 1489-1494.

178. Czapla, B., et al. *Potential for passive radiative cooling by PDMS selective emitters*. in *ASME 2017 Heat Transfer Summer Conference*. 2017. American Society of Mechanical Engineers Digital Collection.

179. Li, X., et al., *Integration of daytime radiative cooling and solar heating for year-round energy saving in buildings.* Nature communications, 2020. **11**(1): p. 1-9.

180. Ko, H. and A. Javey, *Smart actuators and adhesives for reconfigurable matter.* Accounts of chemical research, 2017. **50**(4): p. 691-702.

181. *IR Transmission Spectra*. December 2020]; Available from: https://www.gemini.edu/observing/telescopes-and-sites/sites.

182. Lv, S.-P., S.-H. Liu, and Y.-B. Zhao, *Design and analysis of a pyramid absorber vertex angle.* Materials Technology, 2005. **20**(4): p. 211-213.

183. Li, M., et al., *Submicrometric Films of Surface-Attached Polymer Network with Temperature-Responsive Properties.* Langmuir, 2015. **31**(42): p. 11516-11524.

184. Hippler, M., et al., *Controlling the shape of 3D microstructures by temperature and light.* Nature communications, 2019. **10**(1): p. 1-8.

185. Nishiguchi, A., et al., *4D Printing of a Light-Driven Soft Actuator with Programmed Printing Density.* ACS applied materials & interfaces, 2020. **12**(10): p. 12176-12185.

186. Nishiguchi, A., et al., *In‐Gel Direct Laser Writing for 3D‐Designed Hydrogel Composites That Undergo Complex Self‐Shaping.* Advanced Science, 2018. **5**(1): p. 1700038.

187. Qu, J., et al., *Micro-structured two-component 3D metamaterials with negative thermal-expansion coefficient from positive constituents.* Scientific reports, 2017. **7**: p. 40643.